DISS. ETH NO. 25852

Characterizing Axially Blown Arcs for Passive Oscillation DC Switches

A thesis submitted to attain the degree of

DOCTOR OF SCIENCES of ETH ZURICH

(Dr. sc. ETH Zurich)

presented by

Lorenz Stefan Johannes Bort

Master of Science ETH in Physics

born on 15 April 1987
citizen of Nürnberg / Germany

accepted on the recommendations of:

Prof. Dr. Christian M. Franck,
Prof. Dr. Kaveh Niayesh

2019

Abstract

Switchgear for high voltage direct current transmission systems is needed, especially for schemes with more than one terminal. In the 1980s, concepts for circuit breakers were developed [BMR+85, VCP+85,LSY+85], which used the passive oscillation principle. These were designed for line commutated converters (LCC), which inherently limit the current in case of a fault and can tolerate fault neutralization times between 30 ms and 60 ms.

In the last decade, significant advances were made in the field of voltage source converters. These allow greater flexibility, namely power flow reversal without the need of reversing polarity, and an independent control of active and reactive power on the AC side. In case of a fault, VSC converters do not limit the current. In contrast, they feature filter capacitors on the DC side, which quickly discharge into a fault leading to a high $\mathrm{d}i/\mathrm{d}t$ [Buc14]. Additionally, they usually use IGBTs, which are much less tolerant to overcurrents than the thyristors in LCC converters. This combination, as well as the fact that there are real multi terminal projects (for example 3 terminals in Nan'ao, 5 terminals in Zhoushan, 4 and 7 terminals in Zhangbei 1 & 2 respectively, according to [ATW17]) sparked another wave of DC breaker research. Technical Brochure 683 of CIGRE nicely summarizes the state-of-the-art in the year 2014 [CTB683]. Circuit breakers which can neutralize a quickly rising fault current ($>3\,\mathrm{kA\,ms^{-1}}$) in less than 10 ms or even 5 ms were developed, for example [CBHJ12] or [TWZ+16, WWR+14, ZYC+18, WYC+18, WLL+18]. Those are rather complex devices, compared with the passive oscillation topology. However, the CIGRE-working group also identified several cases, where ultra high speed and complexity is not necessary, and therefore *Transfer Switches* with passive oscillation topology are still a viable option, if they can be improved.

This thesis investigates the voltage-current characteristic $u(i)$ of gas blast interrupters, which is the main component of passive oscillation

switches. A negative differential resistance $\mathrm{d}u/\mathrm{d}i$ is needed for amplification of the oscillation, which is generally the case in axially blown arcs, for *low current*. This is called Mayr regime, but transitions into the Cassie regime at *higher currents*, where the voltage is independent of current, i.e. $\mathrm{d}u/\mathrm{d}i = 0$. Methods to quantify this transition current as well as the arcs inherent random fluctuations and its dynamic behaviour were developed. The static and dynamic behaviour is obtained by using a special current waveform, which combines a slow current ramp with fast current transients. Furthermore, the axial voltage distribution was determined by variation of electrode positions in the nozzle. Nozzle wall ablation rates were obtained by measuring the change of weight, as well as scanning its contour to determine ablation rate as function of axial position. Using the newly developed methods, the influence of the arcing zone on the static $\mathrm{d}u/\mathrm{d}i$ and the dynamic arc time constant τ was studied. Several experiment series were performed to analyze the impact of blowing gas, the inlet pressure, the nozzle geometry and nozzle material. It was found that the gas flow is the dominant factor that determines the arc voltage. Specifically the acceleration towards Mach 1 in the converging segment of the nozzle contributes most favourably to the static characteristics. The measurements were accompanied by a 1D arc model, similar to the one of [LL75, TL75]. The combination of model results and experiments lead to the hypothesis that the shear layer between hot arc core and cold surrounding gas is actually responsible for the desired negative differential resistance $\mathrm{d}u/\mathrm{d}i$, and the transition from Mayr to Cassie regime is linked to a critical arc radius.

Kurzfassung

Der Bedarf für Schaltgeräte in Hochspannungsgleichstromübertragungssystemen (HGÜ) ist gewachsen, insbesondere für Anlagen mit mehr als einer Konverterstation. In den 1980er Jahren wurden bereits Konzepte für Gleichstromleistungsschalter entwickelt [BMR+85, VCP+85, LSY+85], basierend auf dem passiven Oszillationsprinzip. Diese Schalter wurden für netzgeführte Stromrichter (LCC/CSC) entwickelt, welche im Fehlerfall auftretende Überströme von selbst limitieren, und Ausschaltzeiten zwischen 30 und 60 ms tolerieren. Im letzten Jahrzehnt wurden im Bereich der spannungsgeführten Stromrichter (VSC) grosse Fortschritte gemacht. Diese sind flexibler als die netzgeführten Stromrichter, insbesondere erlauben sie Lastflussumkehr ohne Polaritätswechsel der Pole, sowie aktive Kontrolle der konsumierten Blindleistung, unabhängig von der übertragenen Wirkleistung. Allerdings können VSC Umrichter den Kurzschlusstrom im Falle eines Fehlers nicht begrenzen. Im Gegenteil, die Filterkondensatoren auf der Gleichspannungsseite entladen sich schnell in den Fehler, was zu einem steilen Anstieg des Fehlerstroms führt [Buc14]. Erschwerend kommt hinzu, das die in VSCs verwendeten Leistungshalbleiter (meist IGBTs) im Vergleich mit den Thyristoren in LCCs nur deutlich niedrigere Überstrome tolerieren. Diese neuen Anforderungen, und die Tatsache, dass erstmals HGÜ-Anlagen mit mehr als einem Umrichter im grossen Stil geplant und gebaut werden (beispielweise 3 Terminals in Nan'ao, 5 Terminals in Zhoushan, 4 und 7 Terminals in Zhangbei 1 und 2, wie in [ATW17] beschrieben) hat zu einer neuen Welle an HGÜ Schalterforschung geführt. Die "Technical Brochure 638"der CIGRE fasst den Stand der Technik des Jahres 2014 gut zusammen [CTB683]. Es wurden Leistungsschalter entwickelt, die einen schnell ansteigenden ($>3\,\mathrm{kA\,ms^{-1}}$) Fehlerstrom in weniger als 10 ms oder sogar 5 ms unterbrechen können, beispielsweise [CBHJ12] oder [TWZ+16, WWR+14, ZYC+18, WYC+18, WLL+18]. Diese sind allerdings verglichen mit den passiven Oszillationsschaltern sehr

komplexe Geräte. Die CIGRE Arbeitsgruppe hat einige Schaltfälle identifiziert, in denen derart hohe Schaltgeschwindigkeiten und damit einhergehende Komplexität nicht zwingend notwendig ist. Für diese Schaltfälle sind *Transferschalter* mit passivem Oszillationsprinzip nach wie vor denkbar, falls deren Schaltleistung erhöht werden kann. In der vorliegenen Arbeit wird die Strom-Spannungscharakteristik $u(i)$ von mechanischen Gasschaltern untersucht, welche das Kernelement von passiven Oszillationsschaltern darstellen. Für die Verstärkung der Oszillation ist ein negativer differentieller Widerstand $\mathrm{d}u/\mathrm{d}i$ nötig, was für axial beblasene Lichtbögen während *niedrige Ströme* generell der Fall ist. Dieser Bereich ist allgemein unter Mayr Regime bekannt, für *höhere Ströme* geht dieser ins Cassie Regime über, wo die Lichtbogenspannung stromunabhängig ist, also $\mathrm{d}u/\mathrm{d}i = 0$. Es wurden Methoden entwickelt um diesen Übergang, die zufälligen Fluktuationen der Lichtbogenspannung und das dynamische Verhalten von Lichtbögen zu charakterisieren. Das statische und dynamische Verhalten wird durch eine spezielle Stromform bestimmt, welche langsame Stromrampen mit schnellen Stromimpulsen kombiniert. Des weiteren wurde die axiale Spannungsverteilung bestimmt, in dem die Kontaktpositionen innerhalb der Düse variiert wurden. Der Abbrand von Düsenwandmaterial wurde durch wiegen ermittelt, sowie die ortsaufgelöste Abbrandrate durch Ausmessen der Düsenkontur in axialer Richtung. Mit den entwickelten Methoden wurde die Rolle der Düse auf die statische Lichtbogenkennlinie $u(i)$ und die dynamische Zeitkonstante τ untersucht. Mehrere Experimentserien wurden durchgeführt, um den Einfluss des Beblasungsgases, Einlassdrucks, der Düsenform und des Düsenmaterials zu untersuchen. Die Kühlung durch die Gasströmung wurde als entscheidender Faktor indentifiziert, welcher die Brennspannung des Lichtbogens dominiert. Insbesondere die Beschleunigung auf Mach 1 in der konvergenten Zone der Düse trängt in gewünschter Weise zur Kennline bei. Die Messungen wurden durch ein eindimensionales Lichtbogenmodell ergänzt, ähnlich dem in [LL75, TL75] beschriebenen. Die Kombination des Modells mit den experimentellen Resultaten führt zur Hypothese, dass die Scherzone zwischen heissem Lichtbogenkern und dem ihn umgebenden kalten Gas verantwortlich ist für den negativen differentiellen Widerstand $\mathrm{d}u/\mathrm{d}i$, und dass der Übergang vom Mayr ins Cassie Regime einem kritischen Lichtbogenradius zuordenbar ist.

Acknowledgement

To all the people who made this thesis possible, thank you!
First of all to the ABB corporate research center in Dättwil, who provided funding for the position. Second, to Christian, my supervisor. Far and foremost for keeping all the funding trouble away from us PhDs, and supplying us with a well-equipped lab, where we can focus on our own research.
I would also like to thank the technical and administrative staff, who kept the business running. Henry Kienast was really helpful during the rebuild of the model interrupter in the first two years, where workshop-experience was needed. Lab responsible Hans-Jürg Weber was also helpful, especially dealing with the Hausdienst during the various problems due to the construction site. Thanks to Jonas Trüssel, changing the entire safety-circuit fence and doors was completed fast, despite the customization needed for our special case without a *super-cube*.
Karin Sonderegger-Zaky also deserves a big thank you, for dealing with all the paperwork, bills without proper addresses, hotel bookings in China, printing of student theses and so on. Claudia Stucki, Marina Eisenstat and the rest of the ID-service were also crucial and solved countless support tickets, the last one just a few days before I handed in this thesis.
As stated below, this thesis would not have been possible without the contributions of the many semester and master students who worked with me. Specifically, I would like to thank Vincent Freiermuth for implementing the ablation measurement as independently as he did in his master thesis. The discussions with Julian Humml during his bachelor thesis made me understand the peculiarities of supersonic flow. Lastly, Miriam Vonesch was performing the experiment series with varying gases, materials and pressures equally independent, which allowed me to focus on paper-writing and simulation work during that time.

Thanks also to the inhabitants of *H34*. It was a great time to share the office with you. Especially in the beginning, Andi was great at helping to translate my physics knowledge to "engineer", and showing me where its time to stop (over)thinking and just trying things out. Thank you Tim for countless hours of discussion, be it engineering or politics. Whenever I was going too far with some ideas, you always found the right moment to *earth* me again when necessary, and asked the right questions at the right time. What I missed most when Pascal Bü. defended was his almost unlimited supply of good mood. Also, having a mechanical engineer in the office was very helpful, for discussing ITEM-profile designs, as well as the best rocket-staging sequence to reach Duna. Thanks to all other colleagues, I really think we were a group with a good spirit. We helped and supported each other whenever possible during work and had a great time afterwards as well. I definitively miss spontaneous afterwork-beer with BBQ on the ETL terrace.
Lastly, I'd like to thank my family. First my parents, who sent me to Switzerland "for 12 months, to see how it goes", and supported me although it eventually became more than 12 years at ETH. And Nicole: Thank you for everything. You were there to motivate me when no-one else would, and tolerated it when I was not there, because I was motivated to finish stuff in the lab late. Whatever comes after this, we will also manage it.
♢

List of Own Publications

The following publications and student theses were written during the course of the PhD project.

Journal Publications

[BF18]
L. S. J. Bort and C. M. Franck. Determination of Axial Electric Field Distribution in Blown Arcs With Differential Method. *IEEE Transactions on Plasma Science*, PP:1–7, 2018. doi: 10.1109/TPS.2018.2880950

[BVF19]
L. S. J. Bort, M. Vonesch, and C. M. Franck. Controlling the differential resistance of axial blown arcs. *Journal of Physics D: Applied Physics*, in press, jul 2019. doi: 10.1088/1361-6463/ab34e0

[SHBF19]
T. Schultz, B. Hammerich, L. Bort, and C. Franck. Improving interruption performance of mechanical circuit breakers by controlling pre-current-zero wave shape. *High Voltage*, pages 1–9, apr 2019. doi: 10.1049/hve.2018.5103

For [BF18], LB developed the method, performed most of the experiments (some were performed by the master student Vincent Freiermuth) and evaluated the results. All authors discussed the results. The manuscript was written by LB.

For [BVF19], LB developed the method, implemented the 1D model and analyzed its results. MV performed most of the experiments, and evaluated the experimental results. All authors discussed the results. The manuscript was written by LB.

For [SHBF19], LB contributed the method and code for fitting τ.

The experiments with the FPDCS were performed by LB, TS and BH, and evaluated by BH and TS. All authors discussed the results. The manuscript was written by TS.

All manuscripts were proof read by, and discussed with CF.

Conference Publications

[BF16]
L. S. J. Bort and C. M. Franck. Effects of nozzle and contact geometry on arc voltage in gas circuit-breakers. In *2016 IEEE International Conference on High Voltage Engineering and Application (ICHVE)*, pages 1–4. IEEE, sep 2016. doi: 10.1109/ICHVE.2016.7800700

[RBF16]
A. Ritter, L. Bort, and C. Franck. Five years of pulsed current testing for HVDC switchgear. In *2016 IEEE International Conference on High Voltage Engineering and Application (ICHVE)*, pages 1–4. IEEE, sep 2016. doi: 10.1109/ICHVE.2016.7800658

[BFF17]
L. S. J. Bort, V. Freiermuth, and C. M. Franck. Influence of Ablation on Differential Arc Resistance. *Plasma Physics and Technology*, 4(3):1–4, 2017. doi: 10.14311/ppt.2017.2.145

[BSF19]
L. Bort, T. Schultz, and C. Franck. Determining the Time Constant of Arcs at Arbitrary Current Levels. *Plasma Physics and Technology*, 2019, in press

For [BF16], LB developed the method, performed the experiments and evaluated the results. All authors discussed the results. The manuscript was written by LB.

For [RBF16], the authors' experience of using the current source built by Michael Walter [Wal13] is presented. LB contributed the part on power semiconductors, including the thermal simulations. AR contributed the part on high frequencies and filtering, as well as the simulations of the source. The part about measurement equipment and safety summarizes the work of LB, AR as well as the students Stefan Franz, Daniel Rothmund, Aditya Shekhar, Jaka Strumbelj

and Jonas Trüssel who all gradually improved the setup. All authors discussed the results. The manuscript was written by AR.

For [BFF17], VF developed the scanning method, performed the experiments and evaluated the results, under the supervision of LB. All authors discussed the results. The manuscript was written by LB.

For [BSF19], LB contributed the theoretical basis, the fitting algorithm and all experimental aspects involving the current source. TS was responsible for the DUT during experiments and did most data evaluation work. All authors discussed the results. The manuscript was written by LB and TS.

All manuscripts were proof read by, and discussed with CF.

Student Theses

The work presented in this manuscript would not have been possible without the contributions of many students, who joined the project for their semester or master projects. Their theses are listed below, in chronological order. Julien Thomas started his master thesis roughly at the same time I joined the high voltage lab myself. Although I was not officially supervisor, we spent several weeks in the laboratory together, while I was getting to know the current source, measurement equipment etc. His project was very helpful for me to quickly understand the passive oscillation scheme. Benjamin Simonet's master thesis was the first collaboration with the Institute of Fluid Dynamics, which helped kickstarting the modelling of supersonic flow. Vincent Freiermuth wrote a semester thesis during which he investigated the accuracy of the voltage measurement. I also worked closely with Jaka Strumbelj, supervised by Andreas Ritter while rebuilding the source and debugging of the current sensors, which was team work of all three of us. Mingkun Lui performed many measurements with varying contact positions during her semester project. These were the first systematic series with the upgraded measurement system. At the same time, two more mechanical engineering students joined me: Lara Egli for a semester project and Julian Humml for his bachelor thesis. Julian was a huge help in understanding the the-

oretical particularities of supersonic flow, and made a great effort to simulate the interaction of the arc and the cold gas flow. Lara conducted cold flow measurements, to validate the simulations, and also helped during the process of finding a suitable optical setup for the new highspeed camera. Vincent Freiermuth returned for his master project, which laid the foundation for [BFF17]. Thankfully, he stayed at the institute a couple of weeks after handing in his thesis, to complete the measurement series. Johannes Goedejohann rewrote the highspeed footage evaluation code during his semester thesis. Finally, Miriam Vonesch performed the large number of experiments needed for [BVF19] during her master project.

[Tho14]
J. Thomas. *Small scale testing of hvdc circuit breakers.* Master thesis, ETH Zürich, 2014

[Sim15]
B. Simonet. *Design and Testing of Supersonic Nozzles for High Current DC Circuit Breakers.* Master thesis, ETH Zürich, 2015

[Fre15]
V. Freiermuth. *High Bandwidth Voltage-Divider for HVDC-CB Experiment.* Semester thesis, ETH Zürich, 2015

[Str15]
J. Strumbelj. *Simulation and Upgrade of HVDC Bus-Transfer Setup.* Master thesis, ETH Zürich, 2015

[Liu16]
M. Liu. *Parameter Study of HVDC Circuit Breaker Arcs.* Semester thesis, ETH Zürich, 2016

[Egl16]
L. Egli. *Testing of Supersonic Nozzles for High Current DC Circuit Breakers.* Semester thesis, ETH Zürich, 2016

[Hum16]
J. Humml. *Simulation of Heated Supersonic Gas Flow in a Circuit Breaker Nozzle.* Bachelor thesis, ETH Zürich, 2016

[Fre17]
V. Freiermuth. *Finding the Limits of Theoretical Arc Models.* Master

thesis, ETH Zürich, 2017

[Goe17]
J. Goedejohann. *Development of Highspeed Imaging Evaluation Methods for Arcs.* Semester thesis, ETH Zürich, 2017

[Von18]
M. Vonesch. *Gas Circuit Breaker Arc Voltage Under Different Flow Conditions.* Master thesis, ETH Zürich, 2018

Nomenclature

Acronyms

AIS	air insulated switchgear
CAD	computer-aided design
CB	circuit breaker
CFD	computational fluid dynamics
CMM	coordinate measurement machine
CNC	computerized numerical control
CSC	current source converter, synonym for LCC
CZ	current zero crossing
DSO	digital storage oscilloscope
DUT	device under test
FPDCS	flexible pulsed direct current source
GIS	gas insulated switchgear
HVAC	high voltage alternating current
HVDC	high voltage direct current
IGBT	insulated-gate bipolar transistor
LCC	line commutated converter, synonym for CSC
MMC	modular multi level converter
MOSA	metal oxide surge arrester
MRTS	metal return transfer switch, sometimes also called MRTB, metal return transfer breaker
MTDC	multi-terminal HVDC
PMMA	poly methyl methacrylate, also known as acrylic glas
TIV	transient interruption voltage

TRV	transient recovery voltage
VSC	voltage source converter

Symbols

$\boldsymbol{\tau}$	characteristic arc time constant, thermal inertia
$\boldsymbol{i_{\mathrm{arc}}}$	Current through interrupter, sum of $\boldsymbol{i_{\mathrm{f}}}$ and $\boldsymbol{i_{\mathrm{L}}}$
$\boldsymbol{i_{\mathrm{f}}}$	External current which should be interrupted
$\boldsymbol{i_{\mathrm{L}}}$	Current in LC path, positive if in same direction through interrupter as $\boldsymbol{i_{\mathrm{f}}}$
$\boldsymbol{P_{\mathrm{conv}}}$	Convective cooling power. Losses of arc column energy due to gas flow.
$\boldsymbol{P_{\mathrm{cool}}}$	Cooling power. Sum of all terms that remove energy from the arc column, like radiation or convection.
$\boldsymbol{P_{\mathrm{ohmic}}}$	Ohmic heating power inside the arc column. At all times, $P_{\mathrm{ohmic}}(t) = u(t) \cdot i(t)$.
$\boldsymbol{P_{\mathrm{rad}}}$	Radiative cooling power. Losses of arc column energy due to radiation.
$\boldsymbol{t_{\mathrm{CZ}}}$	Point in time where current through the DC breaker has decreased to the residual current level (leakage through MOSA). See section 10.2 Timing Definitions in [CTB683] for details.
$\boldsymbol{t_{\mathrm{neutralized}}}$	Point in time where DC breaker countervoltage surpasses system voltage, which implies peak current is reached at that point. From there on, the system recovers and current decreases until current zero at $\boldsymbol{t_{\mathrm{CZ}}}$.
$\boldsymbol{u_{\mathrm{arc}}}$	Voltage drop across the interrupter
$\boldsymbol{u_{\mathrm{TIV}}}$	Transient interruption voltage, i.e. voltage drop across the switch during switching in DC. See [CTB683] for detailed definition.
$\boldsymbol{u_{\mathrm{TRV}}}$	Transient recovery voltage, i.e. voltage drop across the switch right after CZ in AC
$\boldsymbol{W_{\mathrm{CB}}}$	Energy a DC breaker must absorb to create current zero.

All non-capitalized variables implicitly assume time dependence, i.e. $\boldsymbol{i_{\mathrm{L}} \equiv i_{\mathrm{L}}(t)}$. This is also true for the power terms, which use capitalized P to avoid confusion with the pressure, p. RMS values are indicated by capitalized letters $\boldsymbol{I_{\mathrm{L}}}$, and amplitudes by the hat symbol $\boldsymbol{\hat{I}_{\mathrm{L}}}$.

Contents

1. Introduction

Since the very early days of electricity use, there was a need to interrupt loaded or highly overloaded lines. Around 120 years ago, the first breakers were designed, consisting of metal contacts immersed in oil tanks that were mechanically separated. One example is shown in figure 1.1. In those early days, the transformer's ability to easily step up the voltage, reduce losses and longer transmission distances decided the competition of AC and DC systems, with AC being the clear winner. The early electrical island systems were more and more interconnected, leading to a grid with higher and higher transmission voltage levels ever since. To enable this, much work was done to improve AC breakers, towards higher interruptible currents as well as higher voltage withstand. Reliability went up and maintenance requirements reduced. First, the open tanks were closed, then developed further to *minimum oil breakers* in the first half of the 20th century. A further step was the introduction of the *air blast breakers*, which used a gaseous insulation medium instead of the liquid oil, which greatly reduced the fire risk in case of failures. In the 1970s those were again superseded by the SF_6 *gas blast breakers*, which are still the technology used today, at least for system voltages over 100 kV. In parallel to the *gas blast breaker*, vacuum switchgear became the technology of choice for the medium voltage segment of a few tens of kV, a historical overview is given by [HSKY06]. The push to replace the very potent greenhouse gas SF_6 in the wake of the Kyoto Protocol and other international efforts to reduce global warming lead to the development of vacuum circuit breakers for transmission voltage levels. Single break vacuum circuit interrupters for 72 kV were already available in the 1980s and 1990s [SHK+98], in the last decade this was pushed to 145 kV [HHT+18], and interrupters for 245 kV are likely to follow soon. To reach higher ratings, series connection of these interrupters similar to the early air blast and SF_6 designs is possible, as shown by [FCM16] for example. The following

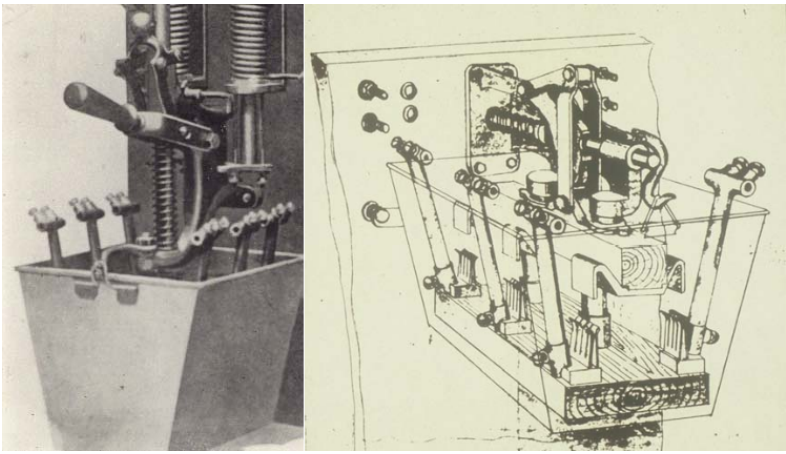

Figure 1.1: Oil breaker designed by L.L. Elden in 1898. Installed at the Boston Electric Light Company L Street Plant (later Boston Edison), featuring an open tank with upward motion operation, mounted on a panel. Taken from [Nel08]

sections summarize the aspects of switching in gas blast interrupters that are important for the present work. A more thorough discussion of the switching process, the devices used and the technological and physical challenges can be found in [Nak91, Kap11, NR17].

1.1. Switching in HVAC Systems

After a fault occurs in a high voltage AC system (i.e. a conductive path exists between phases or phase and ground, indicated by R_{fault} in figure 1.2a), the resistance of the circuit is close to zero. The current amplitude delivered into the fault is therefore only limited by the line inductance, and reaches values of 20 kA to 70 kA. This is a steady state, the grid is loaded with a huge reactive load, as shown in figure 1.2b. The switching duties for breakers in high voltage AC systems can be described in three parts. After t_{fault} the breaker must first withstand the overcurrent situation while opening. All other equipment, like transformers, generators also must tolerate these overcurrents. Secondly at one of the following zero crossings of the current (CZ), the breaker must stop conducting. Third, it

must withstand the rapid increase of voltage which builts up. This is illustrated in figure 1.3. Although the system voltages are in the 100 kV range, and the current amplitudes are also measured in kA, the power dissipated in the breaker is rather low (still in the MW range) compared to the apparent power that is interrupted, because the voltage is low while current is high before CZ, and vice versa after CZ.

All types of breakers fulfill these tasks in a similar fashion. Metal contacts are mechanically separated in phase one, drawing an arc between them, i.e. conducting plasma. At CZ, this plasma is rapidly cooled down, decreasing its conductance and therefore interrupting. This cooling is done by the oil in the earlier designs, and by supersonic gas flow in the air and gas blast concepts. Figure 1.4 shows the geometry of a SF_6 puffer breaker, which creates the gas flow by compressing a puffer volume during the motion of the contact. This axial gas flow cools the plasma column that burns in the center of the cylindrical nozzle, allowing a fast increase resistance in the few µs before and after current zero, to prevent so-called *thermal reignition*. Additionally, after current zero the volume that was occupied by the arc needs to be filled as fast as possible with as much high density gas as possible to prevent *dielectric reignition*. The probability that the breaker is capable of clearing at CZ is mainly determined by the $\mathrm{d}i/\mathrm{d}t$ before CZ, and the $\mathrm{d}u/\mathrm{d}t$ after. Significant research has been performed to understand the details of the processes around CZ and a large body of literature exists, e.g. [Rag78], which is essentially a collection of relevant papers, or [SK00]. However, for this manuscript it is not necessary to understand the exact details of interruption, assuming that gas blast breakers just clear at current zero crossings is sufficient, provided $\mathrm{d}i/\mathrm{d}t$ and $\mathrm{d}u/\mathrm{d}t$ are not excessively high. The necessary details and physical processes relevant for this thesis are explained in section 1.4.

To summarize the AC situation, there exist solutions to interrupt every fault that may occur in any part of the power transmission system. Breakers exist for the highest voltages up to 1100 kV, using series connection of gas blast interrupters, where each can withstand several hundred kV. Solutions also exist for lower voltages, but extremely high currents. like they are expected between large (> 1 GVA) generators and their machine transformers. Nominal

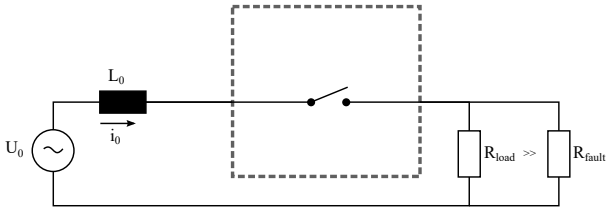

(a) Equivalent circuit of an AC fault. The resistive load is bypassed by a low impedance fault. Therefore, the current is determined largely by the line inductance L_0, and the breaker needs to be able to interrupt at current zero, which is close to peak voltage of the grid U_0.

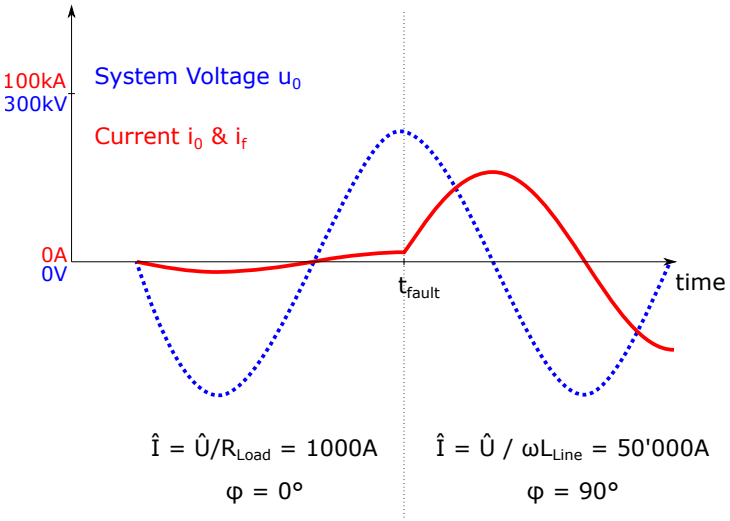

(b) Prospective fault current for AC systems. The numbers indicate roughly the order of magnitude. Load currents are roughly 1 kA and in phase with the voltage, fault currents typically around 20 kA to 70 kA, and phaseshift is highly inductive (almost 90 degrees).

Figure 1.2: Faults in AC systems.

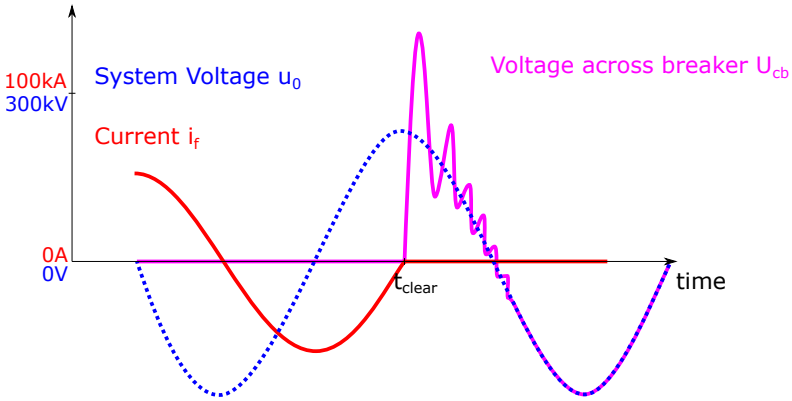

Figure 1.3: Transient recovery voltage in case an AC breaker clears. The current naturally goes to zero, and the breaker clears. The voltage quickly recovers to the system voltage, which is near its peak due to the inductive phase shift. Transient over- and undershoots up to double the system voltage can occur in the most severe switching cases.

current exceeding (25 kA) and even higher fault currents (250 kA) can be carried and interrupted. Yanabu nicely summarized this using Japan as example [YZH06]. AC interrupter development is ongoing, but is focussed on gradual improvements of existing devices rather than driven by the need to solve switching cases for which no solution exists so far. The most notable topic at the moment is the replacement of SF_6 gas by an alternative with less global warming potential. Switching load currents is not much different from switching faults, the principles are the same, only the stresses for the interrupter in terms of $\mathrm{d}i/\mathrm{d}t$ before, and $\mathrm{d}u/\mathrm{d}t$ after CZ are much lower.

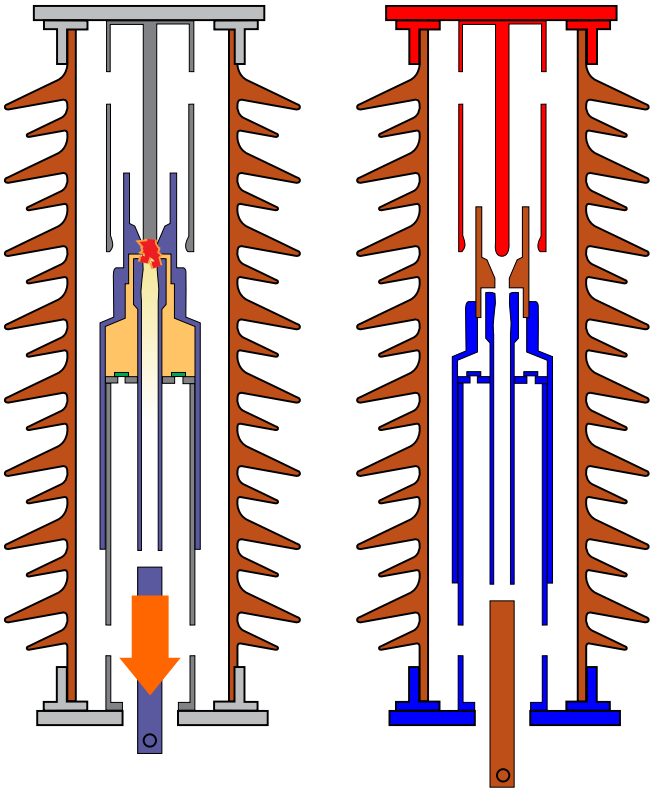

Figure 1.4: Schematic of an SF_6 puffer type gas blast interrupter. Usually (in AC context), only the central part with contact system and nozzle are called *interrupter*, and the entire assembly including the drive is referred to as *breaker*. However, in HVDC context the word *breaker* usually refers to a more complex topology, where the shown device is only a part of many. For consistency, throughout this thesis the word *interrupter* is therefore used to refer to the gas blast interrupter, including enclosure, drive etc.
When opening (left), the nozzle and hollow contact are pulled down (all purple parts move), which separates the arcing contacts. Simultaneously, the stationary piston (all grey parts do not move) compresses the gas in the puffer volume (pressure is indicated in orange), which creates a strong axial gas flow to aid arc extinction at current zero. In the open position (right), the materials are shown by the colors: orange are insulators (enclosure and PTFE nozzle), red indicates the metal parts of the upper terminal, blue the lower terminal. Taken and adapted from [ABB13]

1.2. Switching Load and Fault Currents in HVDC Systems

In the case of DC switchgear, the state of the art is different: there are still many problems waiting to be solved. This has two main reasons.

First, the need to interrupt DC currents was limited to small niche applications for many decades. Examples are all systems containing batteries, traction for public transport (trams, trolley busses, subways and some trains) or the semi-famous DC grid for elevators in San Francisco [Fai12]. These system voltages rarely exceed several hundred to a few thousands of volts, and could therefore be handled by devices that interrupt the current by passively creating a counter voltage higher than the system voltage. This can easily be done by fuses, or air blast breakers using splitter plates, which use the voltage drop of (many series connected) arcs to force the current to zero. Only the introduction of HVDC systems in the 1960s created the need for switchgear that can interrupt DC in systems where arc voltage alone is not sufficient.

Second, and more important: switching off DC currents is intrinsically harder than interrupting AC currents. This is due to the fact that 50 Hz AC currents feature natural current zero transitions every 10 ms (or 8.3 ms in case of 60 Hz). As described before, breakers for AC can wait for the current to decrease to zero, and just need to prevent the system voltage from driving current in the opposite direction afterwards. In DC systems, the current follows the exponential curve of an LR circuit, which asymptotically reaches the current $i_\mathrm{f} = u_\mathrm{system}/R_\mathrm{fault}$. This is illustrated in figure 1.5. With a fault resistance in the range of single digit or maybe tens of Ω, the DC voltage first drops over the line inductance. Unlike in AC systems, the inductance does not limit the fault current amplitude, but only determines its rate of rise. In steady state, the current is only limited by the fault resistance, leading to fault currents much higher than in the AC case, as shown in figure 1.5b. These levels cannot be tolerated for two reasons. First, modern DC converters use IGBTs, which unlike AC equipment (transformers) cannot carry fault currents of that level, not even for several (ten) milliseconds. And secondly, all the fault power is active. A fault current of 10 kA in a 400 kV

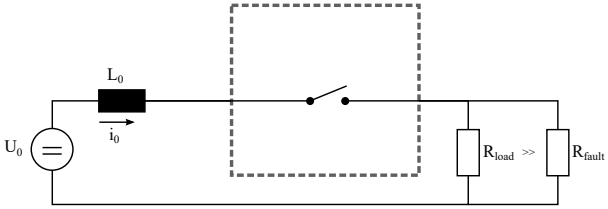

(a) Equivalent circuit of a DC fault. As in figure 1.2a, the resistive load is bypassed by a low impedance fault. In the DC case, the current will exponentially grow to U_0/R_{fault}, and the inductance L_0 only determines the initial rate of rise, $\mathrm{d}i/\mathrm{d}t = U_0/L_0$. The breaker needs to provide a counter voltage U_{CB} higher than U_0, to actively reduce the current, which then falls with $\mathrm{d}i/\mathrm{d}t = -(U_0 - U_{\text{CB}})/L_0$ (see figure 1.6).

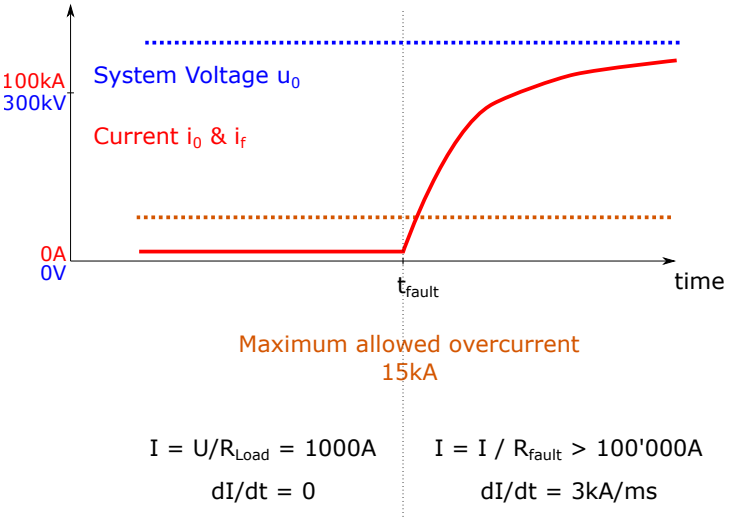

(b) Prospective fault current in a high voltage DC system. As in figure 1.2b, this is a qualitative view, and the numbers indicate orders of magnitude. Load currents are in low kiloampere range, whereas the fault current would rise quickly to values which are intolerable by converters and other attached equipment.

Figure 1.5: Faults in DC systems.

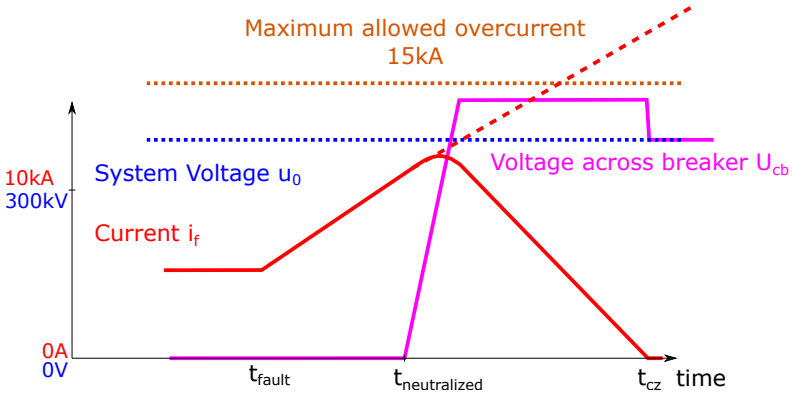

Figure 1.6: Idealized current and voltage waveform of a DC circuit breaker. At time t_{fault} the fault current starts rising. In order to interrupt, the breaker needs to provide a counter voltage u_{cb} higher than the system voltage u_0. The time when this happens is denoted as $t_{\text{neutralized}}$. During the following time until t_{CZ}, the breaker needs to dissipate significant energy: The energy, which has been stored in the line inductance, plus the energy the converter supplies during the time until current zero $0.5\, L_0\, i_{\text{f}}^2(t_{\text{neutralized}}) + \int_{t_{\text{neutralized}}}^{t_{\text{cz}}} u_0(t) \cdot i_f(t)\text{d}t$ (see equation (1.2)

DC system consumes 4 GW active power. Thus DC faults pose a significant risk for system stability, both for the AC/DC converter control, as well as for the connected AC grid. Detailed stability studies have to be performed during the protection system design for each individual DC project, and quite some relevant literature exists, for example [CTB739].
In order to bring the current to zero, switches in DC systems need to create a counter voltage of several hundred kilovolts while still conducting current, as shown in figure 1.6. This means, the breaker (entire topology including energy absorption path, not only the interrupter) needs to dissipate significant power. Driving 10 kA to zero in 4 ms by generating a counter voltage $u_{\mathrm{cb}} = 600\,\mathrm{kV}$ is a hypothetical but realistic scenario. In this case, the breaker must absorb

$$W_{\mathrm{cb}} = \int_{t_{\mathrm{neutralized}}}^{t_{\mathrm{CZ}}} u_{\mathrm{cb}} \cdot i_{\mathrm{f}}\,\mathrm{d}t = 0.5 \cdot 600\,\mathrm{kV} \cdot 10\,\mathrm{kA} \cdot 4\,\mathrm{ms} = 12\,\mathrm{MJ}, \quad (1.1)$$

after $t_{\mathrm{neutralized}}$, with peak power dissipation of 6 GW. This value is usually much larger than the energy dissipated during the time between t_{fault} and $t_{\mathrm{neutralized}}$, which is therefore neglected here. Depending on the breaker topology, power dissipation during this period might nevertheless be an important value for other branches in parallel to the energy absorption branch. The total energy that needs to be dissipated is a function of peak fault current $i(t_{\mathrm{neutralized}})$, line inductance and also the overvoltage the breaker generates with respect to the nominal dc voltage. The example in equation (1.1) assumes a DC voltage $u_0 = 400\,\mathrm{kV}$, a peak fault current $i(t_{\mathrm{neutralized}}) = 10\,\mathrm{kA}$ and a line inductance $L = 80\,\mathrm{mH}$. From the DC-grid perspective, the energy to dissipate until current zero can be expressed as follows

$$W_{\mathrm{cb}} = W_{\mathrm{inductance}} + W_{\mathrm{gridinfeed}} \quad (1.2)$$

$$W_{\mathrm{cb}} = 0.5\, L_0\, i_{\mathrm{f}}^2(t_{\mathrm{neutralized}}) + \int_{t_{\mathrm{neutralized}}}^{t_{\mathrm{cz}}} u_0 \cdot i_f(t)\mathrm{d}t \quad (1.3)$$

The first term of the sum is the stored energy in the line inductance. This is only a function of L and peak fault current i_{f}. The second

term is the amount of energy added to this, by the dc grid during the time until current zero. As a worst case it is assumed that the voltage of the converters is perfectly stiff. In this case, $u_0 = -400\,\mathrm{kV}$ partly counters the voltage of the circuit breaker u_{cb}, which defines the slope of the current:

$$u_0 + u_L + u_{\mathrm{cb}} = 0 \tag{1.4}$$

$$\frac{\mathrm{d}i_{\mathrm{f}}}{\mathrm{d}t} = \frac{u_L}{L} \tag{1.5}$$

$$\frac{\mathrm{d}i_{\mathrm{f}}}{\mathrm{d}t} = \frac{-u_{\mathrm{cb}} - u_0}{L} \tag{1.6}$$

$$\frac{\mathrm{d}i_{\mathrm{f}}}{\mathrm{d}t} = \frac{-600\,\mathrm{kV} + 400\,\mathrm{kV}}{80\,\mathrm{mH}} \tag{1.7}$$

$$\frac{\mathrm{d}i_{\mathrm{f}}}{\mathrm{d}t} = -2.5\,\mathrm{kA\,ms^{-1}} \tag{1.8}$$

The voltage u_0 is negative here, since energy sources have negative signs in passive sign convention. This current slope defines the time to current zero, and therefore has an influence on the energy fed into the fault by the converter or DC grid. Assuming a constant overvoltage leads to a strictly linear current decay, which leads to a simple solution of equation (1.3):

$$W_{\mathrm{cb}} = 0.5 \cdot 80\,\mathrm{mH} \cdot (10\,\mathrm{kA})^2 + 0.5 \cdot 400\,\mathrm{kV} \cdot 10\,\mathrm{kA} \cdot 4\,\mathrm{ms} \tag{1.9}$$

$$W_{\mathrm{cb}} = 4\,\mathrm{MJ} + 8\,\mathrm{MJ}. \tag{1.10}$$

In this example, with 200 kV overvoltage, it takes 4 ms for the current to go to zero. The energy fed into the system by the dc grid until CZ is double the amount stored in the line inductance. If the breaker created a higher countervoltage of 800 kV, i.e. an overvoltage of 400 kV, time to current zero would be only 2 ms and the infeed would half as well, reducing the total dissipated energy from 12 MJ to 8 MJ. This reduces the duty for the energy absorption path, but increases the overvoltage stress of all connected DC equipment. As

a compromise, a counter voltage of 1.5 pu, i.e. a overvoltage of 0.5 times system voltage is generally accepted [CTB683, DJSH14].

Another requirement for breakers is to introduce minimal losses in closed state. Low losses are desired for obvious economic reasons, on the other hand avoid the need for active cooling which adds complexity and needs maintenance.

There are several different topologies which achieve this, a good summary is provided by [SLF16, CTB683]. The vast majority of topologies consist of three paths: a *nominal current path*, optimized for low on-state losses, a *current commutation path*, which takes over the current from the nominal path, and subsequently creates the counter voltage. The nominal current path needs to withstand the counter voltage at that point. As soon as the counter voltage is high enough, the third *energy absorbtion path* consisting of metal oxide surge arresters (MOSA) then takes over, absorbing the energy while the current drops to zero.

The most challenging aspect of interrupting DC is the allowed time between t_{fault} and $t_{\text{neutralized}}$. This is determined by the system inductance, the system voltage and the system topology. Other constraints are the overcurrent capabilities of the converters, as well as converter topologies. Thyristor-based line commutated converters (LCC) actually limit the current themselves, because they control the current. Additionally, those schemes operate with large smoothing inductors of several hundred mH. This means, fault currents do not rise fast, and breakers for these systems were designed already in the 1980s [BMR+85, LSY+85, VCP+85]. Future HVDC systems, especially meshed grids, are more demanding. Due to their higher flexibility and less reactive power use, voltage source converters become increasingly popular. These regulate the voltage and do not use smoothing reactors, but DC filter capacitors at the output. Thus they do not limit the current intrinsically. With only the line inductance limiting the rate of rise of fault currents, values around $3\,\text{kA}\,\text{ms}^{-1}$ are typical. Additionally, the overcurrent capabilities of IGBTs are lower than the surge rating of thyristors of the more traditional LCCs, which mean the time between t_{fault} and $t_{\text{neutralized}}$ needs to be well below 10 ms for circuit breakers in VSC schemes. A detailed analysis of the fault current waveform can be found in [Buc14].

Circuit breakers that can interrupt fast rising fault currents have received much attention recently, but there are many cases where speed is less critical, and simpler devices can be used. The joint working group A3/B4.34 of CIGRE coined the term *transfer switch* in their technical brochure 683 [CTB683]. These switches are used in all cases, where a load current needs to be interrupted or commutated, against a driving voltage between a few kV and the system voltage. Metal return transfer switches (MRTS) are one example, but also cases where one of several parallel lines or a non-faulty but loaded line are disconnected fall in this category.

For those cases, switches which rely on passive oscillation are a good choice, since they do not posses any of the drawbacks of using power semiconductors. Only a mechanical gas blast circuit breaker (CB) is needed, as well as a parallel LC branch and an arrester bank. This concept is not new, but was already described in the last century, for example by [LSY+85]. Its principle is described in the following section.

1.3. Passive Oscillation Switches for HVDC

A schematic for a passive oscillation DC switch is shown in figure 1.7. The general idea is to artificially create a current zero crossing in the nominal current path by commutating the current to a path with a capacitor. As soon as the nominal current path is interrupted, the capacitor is charged up by the dc current flowing through the commutation path, creating the counter voltage needed to reduce the current to zero. To limit the counter voltage, an energy absorption path starts conducting at a predefined overvoltage.

A gas blast interrupter similar to the ones used in conventional AC breakers is placed in the *nominal current path*. The *commutation path* consists of an LC circuit connected in parallel to the nominal path, possibly with an additional making switch to connect it only after the main CB has opened. The *energy absorbtion path* consists of a metal oxide surge arrester (MOSA), which conducts the load or fault current at about 1.5 times the system voltage.

As the interrupter opens (and the making switch closes, if there is one), an oscillating current in the loop consisting of L, C and the

interrupter's switching arc is started. This current is superimposed on the nominal DC current flowing through the interrupter. If the differential resistance of the arc $\mathrm{d}u/\mathrm{d}i$ is negative, the oscillating current is amplified, until it reaches the same amplitude as the DC current. Chapter 3 discusses this amplification in detail. This creates a current zero crossing in the interrupter, allowing it to clear and commutate the current completely into the LC-branch. As soon as the capacitor reaches the threshold voltage of the MOSA, the current commutates into the arrester bank. The only active component is the mechanical drive, which makes this concept very attractive.
The performance of the passive oscillation concept depends on the arc voltage, specifically on the fact that the arc voltage decreases with rising current. The most important variables are the time it takes from the start of the oscillation until CZ is reached (*fault neutralization time*). This obviously depends on the magnitude of the current to break, and whether it is rising, and if so, how fast. Another important variable is the maximum interruptible current. Above a certain current, the differential resistance of arcs is zero, making self amplification of the oscillation impossible. Typical values for the breakers of the 1980s were 2 kA interruptible current, and fault neutralization times in the range from 20 ms to 60 ms, including time needed for the interrupter to open. The amplification of the oscillation was already achieved below 1 ms in one case, where making switches were used [BMR+85, VCP+85].

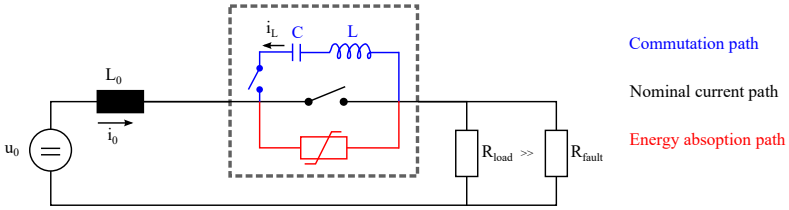

Figure 1.7: Equivalent circuit diagram of a DC breaker using passive oscillation. The nominal current path is a gas blast interrupter, which is only able to clear at current zero crossings. An LC path, either permanently connected or with an additional a making switch, is the commutation path. As soon as the oscillating current amplitude is higher than i_0, the interrupter can clear. Subsequently, i_0 charges up the capacitor, up to the threshold voltage of the MOSA. At that point, the current commutates to the energy absorption path, which limits the voltage drop over the breaker.

1.4. Arcs in Gas Blast Circuit Breakers

As described in section 1.3, passive oscillation DC switches require the differential arc resistance $\mathrm{d}u/\mathrm{d}i$ of the switching arc to be negative. This is generally true for axially blown arcs, at least for low currents, and often called the *Mayr regime*. For higher current, the arc voltage becomes independent of current, which is referred to as *Cassie regime*. Section 5.3.1 sheds some light on the question what *high* and *low current* actually means, and tries to identify the factors contributing to this transition, but here, a qualitative description is sufficient. Most of the research on switching arcs in the past was focused on the conditions around current zero, to improve the breaking performance of AC breakers, or on the peak value of the current, which is important for pressure built-up due to nozzle wall ablation in self blast interrupters. Thus, the transition between Mayr and Cassie region was not a research priority, as long as the conditions at current zero were known. The books of Ragaller [Rag78], Nakanishi [Nak91], Kapetanović [Kap11], and Niayesh and Runde [NR17] cover progress and the state of the art of switching arc research very well.

In contrast to 50 Hz AC, the behaviour in the intermediate current range (axially blown arc, not dominated by nozzle wall ablation) is important for the optimization of passive oscillation DC breakers. A lot of basic research on gas blast interrupters was con-

ducted in the 1970s, and the literature from that time and onwards is very relevant. Hermann, Kogelschatz, Niemeyer, Ragaller, and Schade published detailed experimental studies of axially blown arcs [HS70,HS72,HKRS74,HKN$^+$74,HKN$^+$76,KS72,BKS72,NR73,Nie79]. Additionally, Lowke, Ludwig and Tuma derived a 1D arc model, which they compared to the experiments for validation [TL75, LL75].

The essential phenomena of axially blown arcs can be briefly summarized as follows. During separation of the two metal contacts of an interrupter, an arc is drawn between them. It is started by a molten metal bridge at the last point of contact, which is quickly evaporated by joule heating of the current flow, and transitions into a column of plasma. This happens inside an axisymmetric nozzle assembly, as illustrated in figure 1.4. The purpose of the nozzle is to create a strong axial gas flow around the arc, which cools it. This can be described by the arc's energy balance.

$$P_{\text{heat}} = P_{\text{cool}} + \frac{\mathrm{d}}{\mathrm{d}t} Q_{\text{arc}} \tag{1.11}$$

$$P_{\text{heat}} = i \cdot u_{\text{arc}} \tag{1.12}$$

$$P_{\text{cool}} = P_{\text{conduction}} + P_{\text{radiation}} + P_{\text{convection}} \tag{1.13}$$

In steady state, the internal energy of the arc Q_{arc} is contant, i.e. $P_{\text{heat}} = P_{\text{cool}}$. The higher the cooling terms, the higher the arc voltage for a given current. Cooling the arc with a supersonic flow increases the convection term, and high pressure leads to high density, which in turn increases the radiation losses. Thermal conductance becomes negligible compared to the other two in that case.

A high cooling power is helpful in interrupters, for two reasons. First, it reduces erosion of the nozzle and contact system by the plasma. And second and more importantly, at current zero the arc is not in steady state anymore. Directly at current zero, the heating is zero, but the cooling terms are not. This decreases the plasma temperature, and increases its resistance. Higher cooling before and at current zero therefore leads to faster voltage withstand capability right after CZ. The cooling terms are a function of plasma column geometry, material parameters of the blowing gas, pressure, temperature and so forth. It is known that for a given interrupter the voltage drops with increasing current, until it reaches a steady value. After that,

the voltage is independent of current, until it eventually rises again when it transitions from flow stabilized to wall stabilized conditions. Much research was done to optimize the interrupter in order to reliably clear at current zero. But the understanding which external parameters determine the $u(i)$ curve and especially the derivative $\mathrm{d}u/\mathrm{d}i$ is still poor. In axially blown arcs, the main cooling mechanisms are clearly convection and radiation, while heat conduction is negligible. How exactly those cooling terms scale with current, and which of them is responsible for the needed negative $\mathrm{d}u/\mathrm{d}i$ is still not well understood. Shedding light on this is the main intention of the present thesis. Whereas a previous work [Wal13] has mainly shown empirical results with respect to variations in blow pressure, nozzle diameter and type of gas, the detailed physical understanding of the measureable changes is targeted.

2. Goals and Structure of this Thesis

The goal of this thesis is to increase the fundamental knowledge about switching arcs, for the application in passive oscillation switches. These switches rely on the negative differential arc resistance, a topic which has not received much research attention. In order to optimize gas blast interrupters specifically for the application, several basic research gaps need to be closed.

The two arc properties of most interest are the absolute arc voltage as function of current $u(i)$, which should be as large as possible, as well as its derivative $R_{\mathrm{diff}} = \mathrm{d}u/\mathrm{d}i$, which should be as negative as possible. It is therefore important to find ways to increase the arc voltage, and decreasing $\mathrm{d}u/\mathrm{d}i$. The best solution would be a detailed understanding of the physical mechanisms that lead to $R_{\mathrm{diff}} < 0$, which allows a targeted optimization of the interrupter to enhance those mechanisms. But even without a full physical explanation, the knowledge which external parameter influences the arc voltage by how much is valuable. In addition to arc studies, it is important to know how improving the arc characteristic translates into higher interruption performance of oscillation switches. Namely, the maximum interruptible current depends on the current value above which $\mathrm{d}u/\mathrm{d}i$ is not negative enough to effectively amplify the oscillation. An optimum solution requires an optimized arc, in combination with an LC-circuit that also takes into account the arc response to dynamically changing current. For this analysis, the coupling of the oscillation with the arc needs to be analyzed.

New methods for arc characterization were designed and implemented in the present thesis, namely:

- a thorough theoretical study of the interaction of switching arc with the LC circuit in passive oscillation switches.

- a robust metric to quantify the static arc behaviour.
- an algorithm to determine the arc time constant τ by using a specialized current waveform and fitting routine, as suggested by [Wal13].
- a differential method to obtain the axial voltage distribution of the arc in the nozzle.
- a scanning technique to obtain spatially resolved wall ablation rates
- an analytical 1D arc model, based on the work of [LL75, TL75], which analyzes convective and radiation cooling.

With these methods, the arc of a model interrupter was studied experimentally while varying various external parameters, to determine the dominant mechanisms leading to favourable $u(i)$. The insights gained allow to give recommendations for future designs of passive oscillation switches.
As shown in the table of content, theoretical study can be found in **chapter three**, the other methods are described in **chapter four**. In **chapter five**, the results of various experiment series are presented and discussed. **Chapter six** gives an outlook to the future, with suggestions for followup work.

3. Theoretical Analysis of the Passive Oscillation Topology

As introduced in section 1.3, passive oscillation switches need an oscillating current of sufficient amplitude to create a current zero in the nominal current path, which is created by self-amplification of an oscillation in the LC-arc loop. There are several parameters that influence how strong the amplification is. A strong enough amplification is needed to reach a current zero crossing at all, and the stronger it is the faster CZ is reached. In order to adapt gas blast interrupters specifically for the application of passive oscillation switchgear, it is necessary to thoroughly understand the amplification process. This analysis allows to specify which behaviour of the arc is favourable and to quantify the limits of the topology for a given arc. In this chapter, first the needed mathematical formulations are derived. Those are then used to simulate the self-amplification process up to current zero in the following sections, for different values of L, C and arc characteristics.

3.1. Renormalizing the Capacitor Voltage

To understand self-amplification, it is important to recapitulate the basics of oscillating circuits. The fundamental frequency of an LC circuit is determined by the values of L and C. If no other components are included (see figure 3.1), current and voltage oscillate, moving the same amount of energy from the capacitor to the inductor back

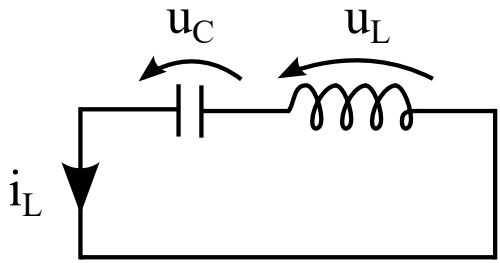

Figure 3.1: Ordinary undamped LC circuit.

and forth indefinitely, as shown by equations (3.1) to (3.4).

$$\omega_0 = \frac{1}{\sqrt{LC}} \tag{3.1}$$

$$i_{\mathrm{L}}(t) = \hat{I_0} \sin(\omega_0 t) \tag{3.2}$$

$$u_{\mathrm{C}}(t) = \hat{U_0} \cos(\omega_0 t) \tag{3.3}$$

$$w(t) = \frac{1}{2}\, C\, u_{\mathrm{C}}^2(t) \;+\; \frac{1}{2}\, L\, i_{\mathrm{L}}^2(t) \quad = \quad \text{const}\ \forall t \tag{3.4}$$

With a resistor in the circuit (see figure 3.2), the oscillation is damped. At this point the author would like to highlight the notation and sign convention used in this chapter, which fixes the direction of voltage arrows. All non-capitalized quantities are variable in time, i.e. $u_C = u_C(t)$ implicitly, whereas capital letters with the hat symbol indicate an amplitude, as used in equation (3.2). For all components, passive sign convention is used, which defines the polarity of the voltage across each component: if the value of the voltage is positive, the voltage arrows in figures 3.1 to 3.4 point from the positive to the negative terminal of each component. This means, if $u_C < 0$ in figure 3.2, the left side is positive, and the right is negatively charged. In this convention, the quantity $p = u \cdot i$ is the power *consumed* by each component. If voltage and current have opposite signs, p is negative and the component *provides* electrical energy. Lastly, according to Kirchhoffs law, sum of all voltages in a loop needs to be zero

$$u_L + u_C + u_R = 0 \qquad \forall t. \tag{3.5}$$

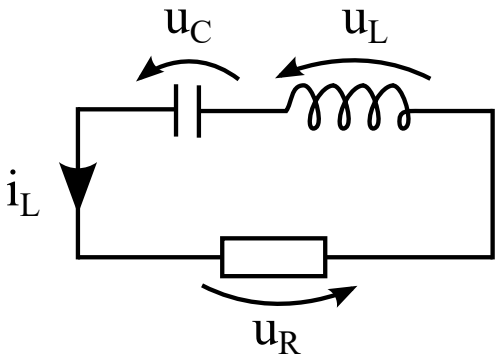

Figure 3.2: Damped LC circuit. Passive sign convention is used, i.e. if current and voltage have the same sign, the component is an electrical load that consumes energy. If they have opposite signs, they are sources. Since $u_\mathrm{R} = i_\mathrm{L} \cdot R$, the resistor is always a load, whereas the capacitor and inductor change roles each quarter-wave, because i_L and u_C change signs with almost (for small values of R) 90° phase shift.

With this convention, the resistive damping is accounted for in equations (3.6) to (3.10).

$$\omega_0 = \frac{1}{\sqrt{LC}} \tag{3.6}$$

$$\delta = \frac{R}{2L} \tag{3.7}$$

$$\omega_d = \sqrt{\omega_0^2 - \delta^2} \tag{3.8}$$

$$i_\mathrm{L}(t) = \hat{I}_0 e^{-\delta t} \sin(\omega_d t) \tag{3.9}$$

$$w(t) = \frac{1}{2}\, C\, u_\mathrm{C}^2(t) \;+\; \frac{1}{2}\, L\, i_\mathrm{L}^2(t) \quad \approx \quad W(0)\, e^{-2\delta t} \tag{3.10}$$

For values of $R < \sqrt{4LC}$, this is an underdamped RLC case with well known behaviour. The amplitude of the oscillation decays exponentially, and after a period between $3/\delta$ and $5/\delta$, the energy in the system can be considered completely dissipated. The parameter $1/\delta$ is effectively the time it takes to reduce the current and voltage amplitude from 1 to $1/e$. To generalize this to the case of an arc

instead of a resistor, we need to take a closer look into equation (3.7) and find a way to replace R by a non-linear term. Maxim Bonkarev did this concisely in his PhD thesis [Bon15], the following derivation of δ is mostly taken from there (with adaptations to keep signs consistent).
If the voltage across L and C is expressed as function of the current through them, equation (3.5) becomes

$$L\,\frac{\mathrm{d}i_\mathrm{L}(t)}{\mathrm{d}t} \;+\; \frac{1}{C}\int_{-\infty}^{t} i_\mathrm{C}(t)\,\mathrm{d}t \;+\; u_\mathrm{R}(t) = 0. \tag{3.11}$$

Differentiation by time gives

$$L\,\frac{\mathrm{d}^2 i_\mathrm{L}(t)}{\mathrm{d}t^2} \;+\; \frac{1}{C}\,i_\mathrm{C}(t) \;+\; \frac{\mathrm{d}u_\mathrm{R}(t)}{\mathrm{d}t} = 0. \tag{3.12}$$

The derivative of the resistive term can now be expanded

$$\frac{\mathrm{d}u_\mathrm{R}(t)}{\mathrm{d}t} = \frac{\mathrm{d}u_\mathrm{R}(i_R(t))}{\mathrm{d}t} = \frac{\mathrm{d}u_\mathrm{R}(i_\mathrm{R}(t))}{\mathrm{d}i_\mathrm{R}} \cdot \frac{\mathrm{d}i_\mathrm{R}(t)}{\mathrm{d}t}. \tag{3.13}$$

Since $i_\mathrm{L} = i_\mathrm{C} = i_\mathrm{R}$, equation (3.13) can be substituted in (3.12), which leads to

$$L\,\frac{\mathrm{d}^2 i_L(t)}{\mathrm{d}t^2} \;+\; \frac{\mathrm{d}u_R(i_L(t))}{\mathrm{d}i_L} \cdot \frac{\mathrm{d}i_L(t)}{\mathrm{d}t} + \;\frac{1}{C}\,i_L(t) \;= 0. \tag{3.14}$$

This is the well-known second order differential equation of an oscillating system, in which the second term of the sum describes the damping

$$\delta = \frac{\mathrm{d}u_R(i_L(t))}{\mathrm{d}i_L} \cdot \frac{2}{L}. \tag{3.15}$$

Equation (3.7) is the simplified version of (3.15), for the case of a resistor with $\mathrm{d}u/\mathrm{d}i = R$. For the more generalized case of a load with non-linear voltage-current relationship, equation (3.15) is correct.
As discussed in section 1.4, arcs do have negative differential resistance $\mathrm{d}u/\mathrm{d}i$, and therefore replacing R by a negative value in (3.7) leads to a state in which the oscillation is negatively damped, i.e. amplified. The current amplitude grows by a factor of e in

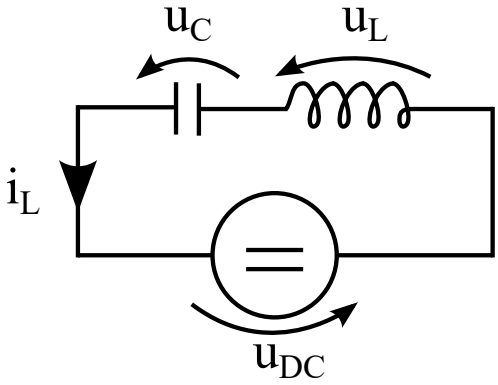

Figure 3.3: LC Circuit plus a DC voltage source (using passive sign convention, i.e positive terminal of the voltage source is left for $u_{\mathrm{DC}} > 0$). The change of current is determined by the voltage drop over the inductor, which is now $\mathrm{d}i/\mathrm{d}t = -\frac{u_{\mathrm{C}}+u_{\mathrm{DC}}}{L}$.

the time $1/\delta$. This might sound like a violation of the principles of thermodynamics at first glance, because the arc as an electrical load (energy sink) seems to be the energy source for the amplification, but this is not the case. If R is replaced by an arc in the circuit shown in figure 3.2, $\mathrm{d}u/\mathrm{d}i$ is only negative for positive current values, but as soon the current i_{L} reverses, the voltage also reverses. The value of the arc resistance u/i is always positive, and $\mathrm{d}u/\mathrm{d}i$ has a singularity at $i = 0$. This means, for $i_{\mathrm{L}} < 0$ equation (3.15) does not hold, and the problem of energy conservation is solved. In case of passive oscillation DC switches however, the superimposed DC current i_{f} shifts the $u_{\mathrm{arc}}(i_{\mathrm{L}})$ curve, leading to a negative differential resistance for all current values $i_{\mathrm{L}} = [-i_{\mathrm{f}}, \infty)$, enabling amplification of an oscillating current up to amplitudes of i_{f}. The power needed for the amplification comes from the external source that drives the DC current, i.e. the DC grid.

To understand this, it is helpful to first look into an LC circuit with an ideal DC voltage source added in series, as shown in figure 3.3.

In this circuit, current will oscillate back and forth exactly like in an ideal LC circuit. However, every time the current flows forward through the DC source ($i_{\mathrm{L}} > 0$ is considered forward), it acts as

energy sink, while it feeds back the same amount of energy to the circuit every time the current flows backwards. Equation (3.4) is not valid anymore due to this periodic exchange of energy with the source. The easiest way to account for this is to renormalize voltage zero. All the equations of the undamped case (3.1) to (3.4) are still valid, if the capacitor voltage is replaced by the sum of capacitor and DC source voltage

$$u_{\mathrm{eff}} = u_{\mathrm{C}} + u_{\mathrm{dc}}. \tag{3.16}$$

The energy which oscillates is therefore

$$W_{\mathrm{eff}}(t) = \frac{1}{2}\, C\, (u_{\mathrm{C}}(t) + u_{\mathrm{DC}}(t))^2) \;+\; \frac{1}{2}\, L\, i_{\mathrm{L}}^2(t) \quad = \quad \text{const}\ \forall t. \tag{3.17}$$

This leads to nonintuitive consequences like the fact that 0 V capacitor voltage does not equal zero energy stored in the renormalized capacitor term (that would be the case if $u_{\mathrm{C}} = -u_{\mathrm{DC}}$). But renormalizing allows the use of the normal differential equations for oscillation, e.g. $\mathrm{d}i_{\mathrm{L}}/\mathrm{d}t = -u_{\mathrm{eff}}/L$. Most importantly, it allows to calculate the effective energy in the system at all times. This energy is a very useful indicator to describe the breaking process, because to eventually clear, all the current i_{f} needs to commutate into the LC branch. This means at least an effective energy of $0.5\ L\ i_{\mathrm{f}}^2$ is needed in the LC circuit to reach CZ. In section 3.3 this is used to compare different LC circuits and boundary conditions, and find optimum values for L and C.

Figure 3.4a shows the real situation in a passive oscillation switch. For simplicity a perfectly flat DC load current of amplitude i_{f} is assumed to be forced through by an external source. As long as the load current i_{f} is not fully commutated into the LC branch, i_{arc} is always positive. An arc in the Cassie regime has a voltage drop independent of current flowing through it, therefore the circuits in figures 3.3 and 3.4a are equivalent. In the forward half-wave of the LC current (i.e. $i_{\mathrm{arc}} > i_{\mathrm{f}}$), the arc is an energy sink, just as expected. In the backwards half-wave there is still forward current through the arc, because even though $i_{\mathrm{L}} < 0$, $i_{\mathrm{f}} + i_{\mathrm{L}} = i_{\mathrm{arc}} > 0$. Looking at the LC-arc loop only, this means the sign of i_{L} reversed, while u_{arc} did

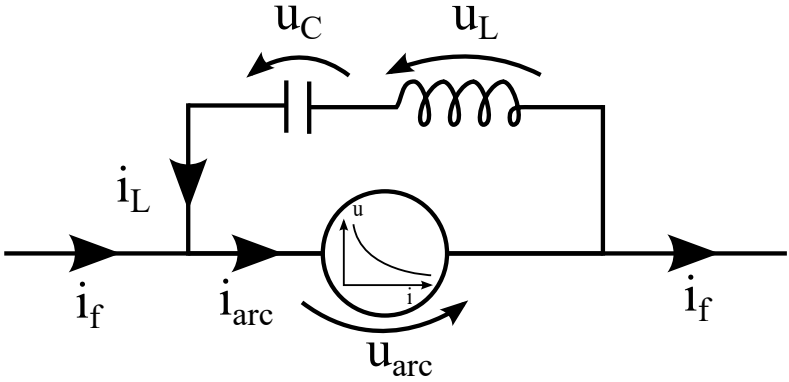

(a) Equivalent circuit of a passive oscillation switch. On top the commutation path with L and C, and on the bottom the nominal current path, with the arc of the gas blast interrupter. As long as $i_\mathrm{f} > i_\mathrm{L}$, the arc voltage never changes its sign. For i_f, as well as the sum $i_\mathrm{f} + i_\mathrm{L}$, the arc is always a load. If only the i_L component of i_arc is considered, the arc is equivalent to the ideal DC voltage source: during the forward half-wave (i.e. $i_\mathrm{L} > 0$) the arc removes energy from the LC circuit, while during the backward half-wave, voltage and current i_L have different signs, which means it acts as an energy source.

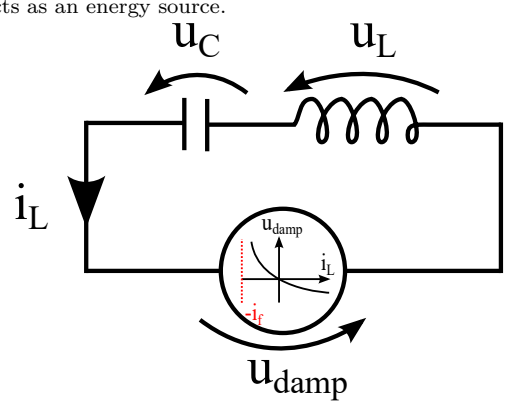

(b) To ease the calculations, it is helpful to eliminate the external current i_f. This can be done by renormalizing the capacitor voltage by adding $u_\mathrm{arc}(i_\mathrm{f})$, and shifting the $u(i)$ curve of the arc by i_f, as indicated in the diagram.

Figure 3.4: Renormalization of the capacitor voltage and voltage-current relationship of the arc, which enables simulation of the amplification.

not. This is only possible as long as $i_\mathrm{L} + i_\mathrm{f} > 0$, i.e. as long as there is no current reversal in the arc path. As soon as the amplitude of i_L is high enough to reach current reversal, amplification stops. However, current reversal means there is a current zero crossing in arc path, which is precisely the goal because it allows the interrupter to clear.
Using this renormalization, it also becomes clear how the arc (an electric load) can be responsible for the amplification. The arc voltage pushes part of i_f into the LC branch, just as the DC voltage source discussed above. As long as the arc voltage is constant, this leads to $\delta = 0$. However, if the arc voltage drops with rising current, the losses in the forward half-wave are smaller than the gains in the backwards half-wave, leading to a net energy gain. This is illustrated in figure 3.4b. If the origin of the coordinate system in the $u(i)$ plot of the arc is shifted to $(i_\mathrm{f}, u_\mathrm{arc}(i_\mathrm{f}))$, it is clear that the arc voltage is in the two *source* quadrants: for positive values i_L the voltage is negative, whereas for i_L negative, the voltage is positive.
The parasitic resistance of the LC-arc loop was neglected in the derivation so far, but it is easy to incorporate: The (positive) parasitic resistance needs to added to the (negative) differential resistance of the arc, and the result still needs to be smaller than zero.

3.2. Modelling Passive Oscillation

In section 3.1 the formalism and renormalization of the arc was derived, that shifts the $u(i)$ curve to the left by i_f, and down by $u(i_\mathrm{f})$. This can be used to simulate the amplification of passive oscillation, for a given $u(i)$ and circuit parameters. In order to analyze which of the parameters influences the amplification by how much, a numeric solver was implemented in matlab, using the forward Euler method. The LC-Arc circuit is simulated, using the following variables:

- L — inductance of LC path (including stray inductance of LC-arc loop)
- C — capacitance of LC path
- R — parasitic resistance of LC-arc path (including ohmic resistance of interrupter)

- τ — dynamic arc constant, as described in section 4.3.3
- $P(g)$ — static arc power as function of conductance, which can be converted to $u(i)$, $g(i)$, $P(i)$ etc.

Additionally, a couple of boundary conditions need to be set. These are:

- $i_\mathrm{f}(t)$ — external current that should be interrupted, $i_\mathrm{f}(0)$ automatically determines the shift $u_\mathrm{DC}(t)$
- $i_\mathrm{L}(0)$ — current in inductor at $t = 0$
- $u_\mathrm{C}(0)$ — voltage of capacitor at $t = 0$, this determines $u_\mathrm{eff}(0)$
- Δt — a timestep for the simulation, small enough to minimize error, while not increasing computation time too much

With this, it is possible to evaluate the time to current zero in the nominal path (i.e. the *fault neutralization time* in the terms of [CTB683]), the number of cycles needed etc. For a given interrupter, which fixes $P(g)$ and τ it is also possible to find the optimal values of L and C. A static $P(i)$ fit for the 12 bar case further described in section 5.2 was used to test the model, and to analyze the influence of L, C and τ, as well as different starting conditions. The static voltage current relationship of this arc is shown in figure 3.5, as well as its derivative, $R_\mathrm{diff} = \mathrm{d}u/\mathrm{d}i$.
Figures 3.6 and 3.7 show simulation results for two examples, where all boundary conditions are equal, except τ, the arc's time constant. The topmost graph shows i_f, which is constant at 1 kA, as well as i_L and i_arc as defined in figure 3.4a. In the second graph, the capacitor voltage is shown, as well as the $-u_\mathrm{arc,if}$, which is the voltage the arc would have, if i_f would flow through it. This is equivalent to u_DC in section 3.1. It also illustrates the fact that even though $u_\mathrm{C}(0) = 0\,\mathrm{V}$, there is energy in the system, since u_C does not oscillate around zero. The third graph shows two different arc voltage curves. The first line, $u_\mathrm{arc,insta}$ shows the hypothetical instantaneous arc voltage obtained from the static $u(i)$ curve and the current in the nominal path. The second line, u_arc represents the real arc voltage, including the delay due to arc time constant τ. This is obtained by using the Mayr-equation similar to the method described in section 4.3.3. The

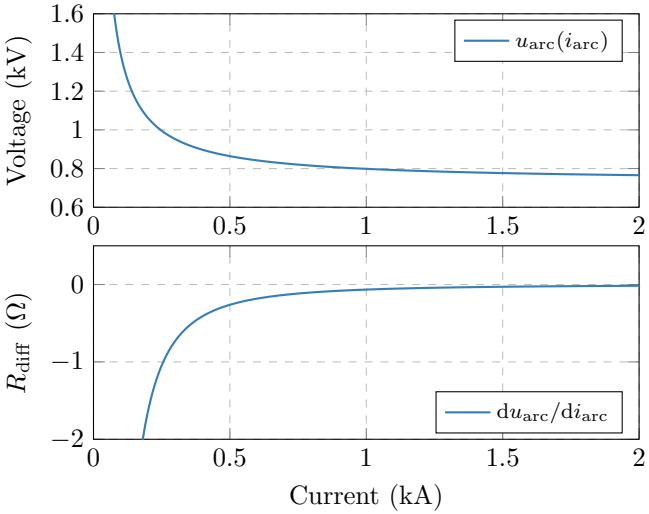

Figure 3.5: Static voltage current characteristic of the arc used in the examples of this section. It is based on a fit of the 12 bar measurement from section 5.2. R_{diff} at $i_{\mathrm{f}} = 1\,\mathrm{kA}$ is $-68\,\mathrm{m\Omega}$, making the sum $R_{\mathrm{total}} = R_{\mathrm{diff}} + R_{\mathrm{parasitic}}$ still slightly negative for the examples in figures 3.6 and 3.7.

last graph in figures 3.6 and 3.7 shows how much energy is stored in L and C, compared to the total energy needed for commutation (see equation 3.17).

Figure 3.6 shows a setup with favourable boundary conditions. The chosen values of $C = 40\,\mu\mathrm{F}$ and $L = 10\,\mu\mathrm{H}$ lead to an oscillation frequency of 8 kHz, which corresponds to a period of 125 µs. This is a lot longer than $\tau = 1\,\mu\mathrm{s}$, therefore the real arc voltage follows the instantaneous value very closely. This is important since in order to amplify the oscillation, u_{arc} needs to be higher than $u_{\mathrm{arc,i_f}}$ as long as $i_{\mathrm{L}} < 0$, and lower than $u_{\mathrm{arc,i_f}}$ for $i_{\mathrm{L}} > 0$. For $u(i)$ curves that are monotonically falling with rising current, this is always fulfilled by the instantaneous curve. The two bottom graphs also show that amplification is much stronger in the backwards half-wave: since $\mathrm{d}u/\mathrm{d}i$ of the simulated arc is more negative for smaller values of i_{arc} (see bottom graph of figure 3.5), the arc voltage deviates much stronger from $u_{\mathrm{arc,i_f}}$ in upwards direction than downwards.

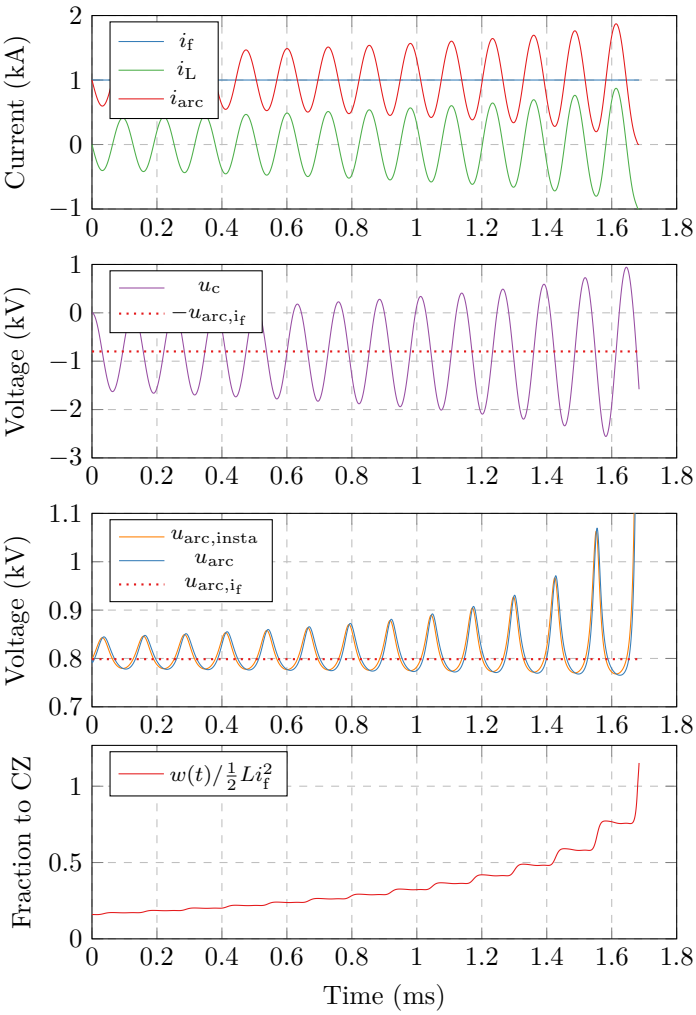

Figure 3.6: Simulation results for a circuit with $L = 10\,\mu\mathrm{H}, C = 40\,\mu\mathrm{F}$, $R = 50\,\mathrm{m}\Omega$ and $\tau = 1\,\mu\mathrm{s}$, the period of the oscillation is $125\,\mu\mathrm{s}$. At $t = 0$, the making switch connects the empty capacitor, which equates to a starting energy in the system of 15% of what is needed to clear. The oscillation grows, until $-i_\mathrm{L} = i_\mathrm{f} = 1000\,\mathrm{A}$ is reached after 1.7 ms.

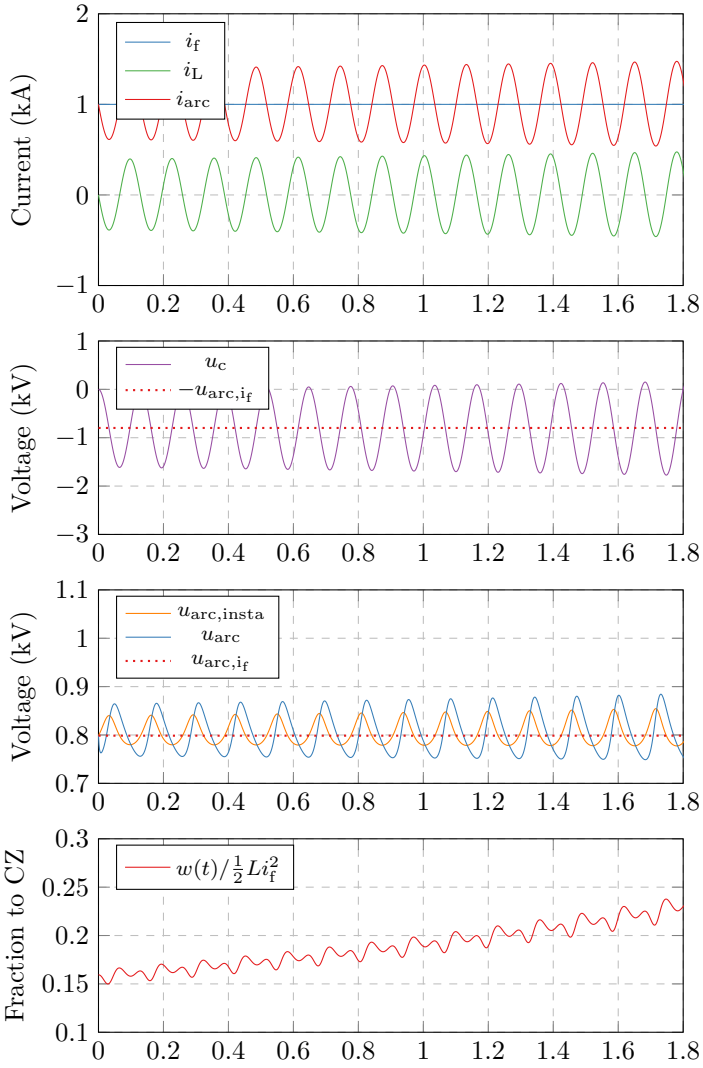

Figure 3.7: Simulation results with identical parameters as shown in figure 3.6, but with $\tau = 5\,\mu\mathrm{s}$ instead of $1\,\mu\mathrm{s}$, i.e an oscillation period of 20τ. The oscilation is only very weakly amplified, as shown in the bottommost graph. Current zero is only reached after 36 cycles and almost 5 ms (not shown). This is due to the fact that the current changes too fast for the arc voltage to adapt in time. The third graph shows the actual arc voltage in blue, and the voltage it would have in equilibrium in orange.

3.3. Parameter Influence on Amplification

The first obvious result of the simulations is, for all currents between zero and i_f the differential arc resistance $\mathrm{d}u/\mathrm{d}i$ must be negative and the more negative, the better. Additionally, in the range from i_f to $2 \cdot i_\mathrm{f}$ $\mathrm{d}u/\mathrm{d}i$ should also be negative but at least be maximally zero and not positive, to prevent any damping in the forward half-wave where i_L adds to i_f in the nominal path. All parasitic resistance in the LC-arc circuit adds positive $\mathrm{d}u/\mathrm{d}i$, and should therefore be minimized.

The second parameter determined by the arc – the thermal inertia described by the time constant τ – should be as small as possible for all current values between 0 A and $2 \cdot i_\mathrm{f}$. The amplification relies on the fact that the arc voltage reacts to changes in current. If those changes happen too fast, the arc cannot follow, and $u(i)$ becomes increasingly resistive. *Too fast* in that case can have two meanings. First, if the natural frequency of the LC-circuit has a period shorter than about $10\ \tau$, the changes of conductance lag too far behind and amplification is not possible at all. Second, the higher the amplitude, the higher the maximum $\mathrm{d}i/\mathrm{d}t$ near the current zero crossing of i_L. This means around CZ the lag due to τ is highest, but transition from forward half-wave to backward half-wave is exactly where the arc voltage should ideally flip from low to high and vice versa. Too much lag can result in a growing oscillation during parts of the oscillation period, but damping in others, as illustrated by the bottom two graphs in figure 3.7. The voltage already lags significantly for $\tau = 5\,\mu\mathrm{s}$ and a period of $125\,\mu\mathrm{s} = 25\,\tau$, and the energy $w(t)$ clearly shows periodic damping.

The values of L and C are coupled because they determine the frequency and should therefore be analyzed together. As stated before, the period of the oscillation must be longer than $10\,\tau$. This poses a certain minimum for the product $L \cdot C$. Since the energy needed to reach full commutation scales linearly with L, this should be minimized. Additionally, the starting energy also scales linearly with C, at least if the oscillation is started by connecting an empty capacitor with a making switch (see below). This means that from a technological point of view it is always favourable to minimize the inductance (i.e. only use the stray inductance of the capacitor

bank), and increase the size of the capacitor. If only the breaking process is considered, there is no upper limit for the capacitor size. Increasing its value decreases the number of cycles needed, as well the time to current zero, until full commutation is reached in the first half-wave already. This would be equivalent to an active injection topology, with a pre-charging voltage of u_{arc}. Additionally, having a larger capacitance also linearly decreases the $\mathrm{d}u/\mathrm{d}t$ after current commutation and helps preventing reignition. On the other hand, low $\mathrm{d}u/\mathrm{d}t$ also increases the time it takes build up the full counter voltage, which is also undesired. A big capacitor also stores significant energy when charged to the system voltage. This energy needs to be absorbed by closing resistors, setting another technological limit. And last but not least, economy introduces another factor, which is likely to dominate: price. The capacitors have to withstand the full transient interruption voltage (typically 1.5 to 2 times the system voltage) are therefore bulky, and minimizing its capacity might have significant influence on the price and geometrical footprint of the entire breaker. Commercial manufacturers might find it advantageous to reduce the capacitor size and increase the inductance (to keep ω_0 low), which increases the commutation time, but is more economical and compact.

The next major factor are the starting conditions. The current in the commutation path at $t = 0$ is zero by definition, but the capacitor voltage is not defined a priori. The simulation does not cover the opening phase of the gas blast interrupter, but only analyzes the growing oscillation for an axially blown arc as found in an interrupter in fully open position. In reality, there are two ways to start the oscillation. The easiest way is to connect the LC path permanently to the nominal path and the oscillation starts due to the rise in arc voltage and random fluctuations during opening (see [BMR+85] for example). Alternatively, the LC-path is connected with a making switch only after the gas blast interrupter has established sufficient contact distance and blowing pressure, as described by [LSY+85]. The first concept is simpler, but making switches could increase breaking performance according to the simulations performed during the present work. This is especially true in combination with high arc voltages. As stated in section 3.1, the energy needed to completely commutate is $0.5\ L\ i_{\mathrm{f}}^2$. In case of a permanently connected LC

branch, the voltage rise of the interrupter during opening is slow enough that the capacitor voltage is able to follow the arc voltage before the oscillation starts. Only after the blowing gas flow reduces τ of the arc to levels low enough to allow oscillation amplification, it grows, starting from almost zero. However, if the LC branch is connected with a making switch only after the arc is fully established, and the capacitor is *empty* (i.e $U_C = 0\,\mathrm{V}$), this means the oscillation starts with u_{eff}. This corresponds to an effective energy of $0.5\ C\ u_{\mathrm{arc}}^2$ in the oscillation circuit, as explained in section 3.1. Depending on the size of L, C, u_{arc} and i_{f}, this can be a significant portion of the needed energy. Since $\mathrm{d}u/\mathrm{d}i$ is usually more negative for lower arc currents (see figure 3.5), the amplification is nonlinear (more amplification if $\hat{I}_{\mathrm{L}}$ is bigger), and starting with even a little more energy reduces the fault neutralization time considerably. Figures 2 and 7 in [LSY+85] indicate this was the case in their design: it starts with an instantaneous current amplitude of around half of the needed value, and fault neutralization occurs after three half-waves. The authors of [LSY+85] actually compare the two options in their Figures 12 and 13, which are in line with the simulations performed during the presented work. Judging from his simulations and literature, the author believes using making switches could significantly boost performance, both in terms of speed and maximum interruptible current.

Series connection of several interrupters — as shown already by most designs from the 1980s — also improves the interruption performance. Especially if all interrupters share only one LC circuit with a making switch, increasing the number of interrupters in series significantly increases the starting energy. Having only one LC branch shared by all interrupters avoids the problem where one of the sub-modules already fully commutated and the others did not (as described by [BMR+85, VCP+85]. Additionally, two series connected arcs posses double the differential $\mathrm{d}u/\mathrm{d}i$ and therefore double the amplification. The commutation time should therefore decrease with the number of series connected arcs (all else being equal). Additionally, random arc voltage fluctuations (see section 4.3.2) should lose importance, assuming they occur independent from each other in the series connected interrupters.

4. Methods

In this chapter, the methods for arc characterization developed during this thesis are presented. In general, the intention is not to characterize a full breaker with nominal, commutation and energy absorbtion path. Only the gas blast interrupter is studied, not the actual oscillation circuit. This is on purpose, since much more fundamental information about arc behaviour can be gathered from a dedicated interrupter characterization setup than from a tests, where little information can be gained except a "pass" or "fail", and maybe time to current zero.

4.1. Current Source

This section is largely based on [RBF16]. The first paragraphs summarize the work of Michael Walter during his dissertation [Wal13], as well as parts of the work of Andreas Ritter presented in [RBF16]. The subsections afterwards cover the authors contribution to [RBF16], with slight modifications.

While voltage sources for DC insulation tests have been commonly available for decades, high current DC sources remained sparse mostly due to a lack of applications. However, the recent increase in research and development activities surrounding HVDC circuit breakers has renewed interest in such current sources. Testing full-scale HVDC CB is generally estimated to require currents of 10 kA or more rising within a few milliseconds in combination with sufficient recovery voltage in order to model fault behavior of an HVDC grid, as explained by Smeets in [SYBS15]. However, in research and development tests of CB components, significantly higher current gradients have to be produced, particularly when evaluating passive oscillation performance and arc characteristics (cf. [BMR$^+$85, NNH$^+$01]). For this reason, an initial plan for building a current source capable of

delivering current pulses at a maximum amplitude of 20 kA at gradients of up to 200 kA ms^{-1} was presented in 2010 by Walter [Wal13]. Within one year, the flexible pulsed DC current source (FPDCS) was developed and commissioned at ETH Zurich's high voltage laboratory. FPDCS' final current rating was set to 3 kA at gradients of up to 50 kA ms^{-1} using power electronics and control systems optimized for cost, delivery time and energy storage. In the time since its commissioning, FPDCS has been in continuous use while receiving intermittent upgrades to improve performance, safety and measurement accuracy. Many of the results gathered from tests using FPDCS on different loads have been published (cf. [Wal13, BF16, BFF17, TCF17, Rit18, RSF18, RF18, BF18, BVF19, SHBF19, BSF19]) while more are certainly to follow.

The main operating principle of FPDCS is that of three identical buck converter modules ($M_1 \dots M_3$) connected in parallel to provide a controllable current i_L to a variable load as shown in the equivalent circuit diagram of Figure 4.1. The peak output currents i_1, i_2 and i_3 are limited to 1 kA each by the ratings of diodes ($D_1 \dots D_3$) and IGBTs ($S_1 \dots S_3$). The entire energy supplied to the load during one test is stored in three parallel connected capacitors ($C_1 \dots C_3$) with a capacitance of 2 mF each and a maximum charging voltage of 3 kV. This enables tests with peak powers over 1 MW, and with total durations up to a few tens to several hundred milliseconds, depending on energy demand of the load. The capacitors are not recharged while supplying a load, which permits the complete electrical isolation of FPDCS from any equipment other than the load during tests. The output inductances ($L_1 \dots L_3$) can be individually varied in 26 steps between 6 µH and 4.5 mH. The control of $S_1 \dots S_3$ is split into a digital part, which determines when current starts flowing from the capacitor according to a set switching frequency. The signal for switching off the IGBTs is given by a high-speed analog part which compares the module currents $i_1 \dots i_3$ to their set values $i_{1set} \dots i_{3set}$ continuously. From the circuit diagram in Figure 4.1, it is clear that the capacitor voltage (and therefore stored energy) decreases whenever the IGBT is conducting. The voltage across each module's inductance changes back and forth between the difference of capacitor voltage and load voltage whenever the IGBT is on and the negative load voltage whenever the IGBT is switched off. Therefore,

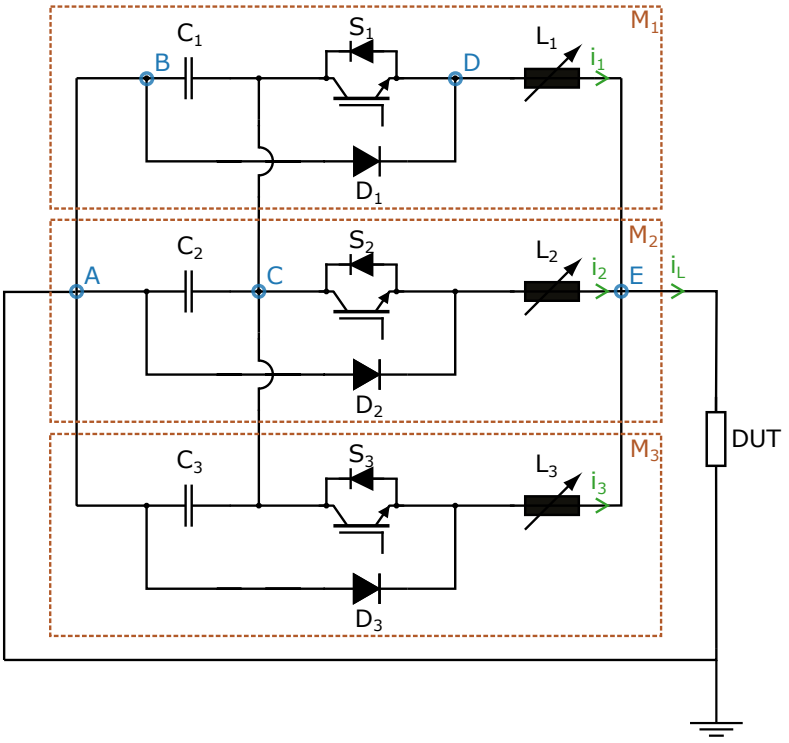

Figure 4.1: Idealized equivalent circuit diagram of power part of FPDCS, showing three buck converter modules with variable inductances in parallel. A denotes the common negative side of the modules and the load. C is the star point of the capacitors, which effectively means all modules share the same energy storage. E is the positive output terminal of the source, where the load is connected. Each module is a buck converter, which either conducts through the diode between points B and D, or inserts the capacitor by turning on the respective IGBT. The DUT is the model interrupter in that case. Only the interrupter itself is characterized, there is no LC or arrester path.

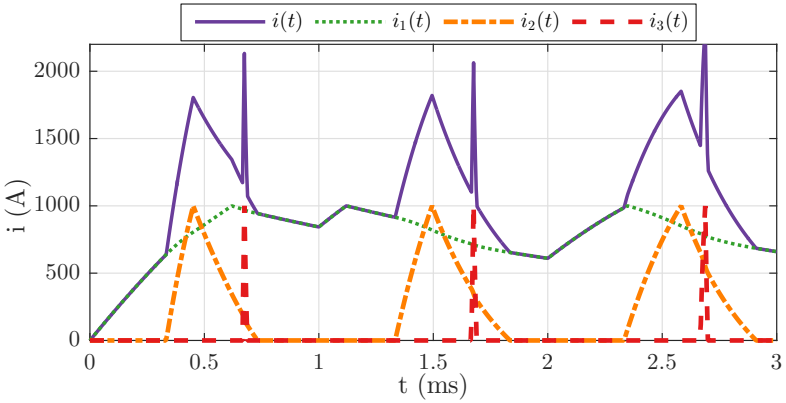

Figure 4.2: Simulation of testing a resistive load using different inductances (L1>L2>L3) but identical set currents and phase shifts between switch-on times of $M_1 \ldots M_3$. Simulation data rather than measurement results are shown to provide idealized explanations of the functioning principles using the simulation tools developed in [Rit18] for HVDC bus transfer tests.

jumps of up to 3000 V within microseconds across $L_1 \ldots L_3$ can occur. The control hardware allows for a configurable phase shift between switching on modules, which permits the creation of complex output currents using moderate switching frequencies, as illustrated by the simulated currents in figure 4.2. In addition, the set current of each module can be defined individually for any point in time prior to starting a test. This combination enables the operator to create intricate current waveforms such as the ones presented in [WF14]. Additionally, it opens up possibilities to rapidly adapt the output currents to different loads. Past and current applications include emulating HVDC grids for testing of a model CB [TCF17], providing different current harmonics for bus-transfer by disconnector [Rit18], and providing currents to characterize arcs, which is used in this thesis.

Over the five years of using FPDCS, many different challenges had to be overcome which are not necessarily present in the idealized representation shown in figures 4.1 and 4.2. Additionally, the area of safe operation was gradually extended through improvements on hardware and software as well as changes in usage practices.

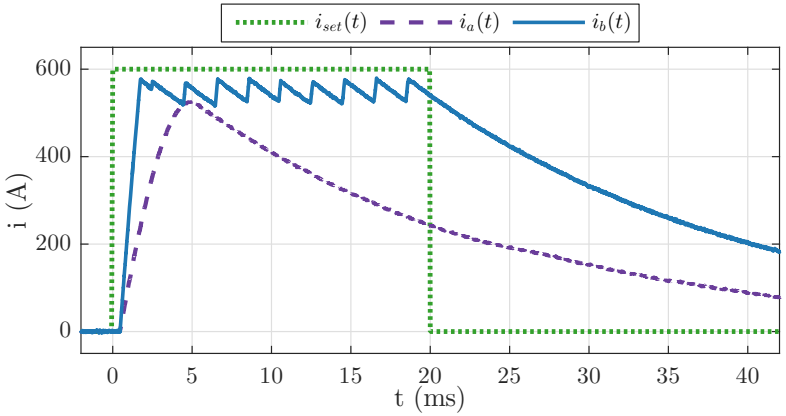

Figure 4.3: Two tests using set current of 600 A for 20 ms. The initial capacitor voltage was raised from 300 V ($i_a(t)$) to 700 V ($i_b(t)$), all other parameters including the load were left unchanged.

4.1.1. Limitations Introduced by Capacitors

When constructing FPDCS, the choice of three 2 mF capacitors represented one of the main tradeoffs between performance, cost, safety and availability. In everyday operations, the capacitors limit three aspects of testing: First, the maximum energy which can be supplied to the load is around 20 kJ (assuming half the voltage, i.e. a quarter of the energy, is left in the capacitors afterwards), setting limits mainly on duration and current magnitude. Secondly, the current gradient during increasing current is directly proportional to the voltage difference between the capacitors and the load, therefore decreasing with dissipated energy. This fact is illustrated by the decreasing steepness of increasing current parts in Figure 4.2. Thirdly, if the load voltage rises above the capacitor voltage at any time during a test, the load current decreases to zero. This is shown by the example in figure 4.3. To provide the load current $i_a(t)$ to a resistive load, the IGBTs stayed on during the entire test duration of 20 ms but after 5 ms the load voltage reached a higher level than the capacitor voltage leading to a slow decay towards zero. By increasing the capacitor charging voltage, the desired current $i_b(t)$ could be

achieved in the resistive load, albeit at a significantly higher initial gradient. For nonlinear loads like arcs in gas interrupters, the load voltage increases with decaying current, which can leads to a very rapid decrease of the load current to zero. Instead of though the interrupter (which clears at CZ and does not reignite afterwards), the current of one module can flow backwards through another module instead, recharging the capacitor. This is potentially a dangerous situation for the source, since it only works if one of the module inductances is set to a small value, allowing fast commutation into it without high overvoltages. If this alternative path is not available, the arc voltage extinction peak could reach values much higher than the 4.5 kV to which the semiconductors are rated, and destroy them. Therefore, if the load is capable of interrupting the current, or creating high counter voltages, one of the modules is set to an inductance value below 100 µH. Additionally the operator must ensure that this module is not carrying forward current in the moment where the load stops conducting, to be able to quickly absorb the current of the other modules. Future systems or upgrades should protect the IGBTs and diodes with snubber circuits or MOSA modules at appropriate locations.

4.1.2. Maximum Temperature of Power Semiconductors

Due to the short durations of each individual test, the switching and conduction losses generated by the power diodes and IGBTs heat almost exclusively their silicon dies. The maximum acceptable temperature rise of 100 K therefore imposes a complex boundary on the number of switching operations as well as the set current levels and their durations. In order to maximize FPDCS' potential, a worst-case thermal loss simulator was implemented which automatically predicts turn on, turn off and conduction losses in all semiconductors prior to any test. Before charging of the capacitor starts, the user is warned if the thermal losses would potentially damage a diode or an IGBT. Not only does this simulator protect the semiconductors from potentially damaging heating, it also allows the user to quickly evaluate the feasibility of certain test currents in advance. No online thermal modelling is performed during the test, and the load behaviour and

therefor duty cycle of IGBT and diode is unknown to the simulator. Thus, a worst case analysis must be performed, which simply assumes the IGBTs and diodes both have to carry the current all the time. This effectively adds a considerable safety margin.

4.1.3. Power Semiconductor Particularities

FPDCS' circuit shown in figure 4.1 was originally chosen over more advanced DC-DC designs mainly due to its cost-effectiveness, the availability of components and the fact that it can be controlled by a fast and reliable control loop. As such, the chosen design relies on switching the IGBTs $S_1 \ldots S_3$ off while current is flowing and on when voltage is applied (i.e. hard switching). Figure 4.4a shows a typical switch-on operation of an IGBT whenever current was previously flowing through the freewheeling diode of the same module. The initial current rise is significant in its magnitude but well within the specifications of the IGBT modules in use in FPDCS because the inductance of the commutation path (labels B and D in figure 4.1) was minimized during construction. Other than the heating of the IGBT substrate — which is accounted for in the thermal simulator — this switching mode has no negative effect on FPDCS. Current waveforms b and c of figure 4.4 show the two different recovery modes of the diodes $D_1 \ldots D_3$. In both cases, a module with very low inductance is switched on for a short time (10.5 µs in figure 4.4b, 7.5 µs in 4.4c) while a current of slow gradient is already provided by another module. When the current of the low inductance module reaches zero, the semiconductor diode needs a recovery charge of 560 µC to 930 µC in order to stop conducting (according to data sheet of diode 5SLD 0650J450300 by ABB). In case b a soft recovery is observed, whereas in case c, snappy recovery leads to a rapid oscillation of the module current around zero, increasing thermal losses in the diode considerably. A detailed study of failure modes stemming from diode reverse recovery is given by Rahimo in [RS01]. While the high current gradients typical for snappy diode recovery does not pose a problem for FPDCS, it constitutes a potential failure mode: The total duration of reverse conduction of the diode in question is increased, which in turn increases the chance of an IGBT switching on in this state. This poses additional transient stresses to

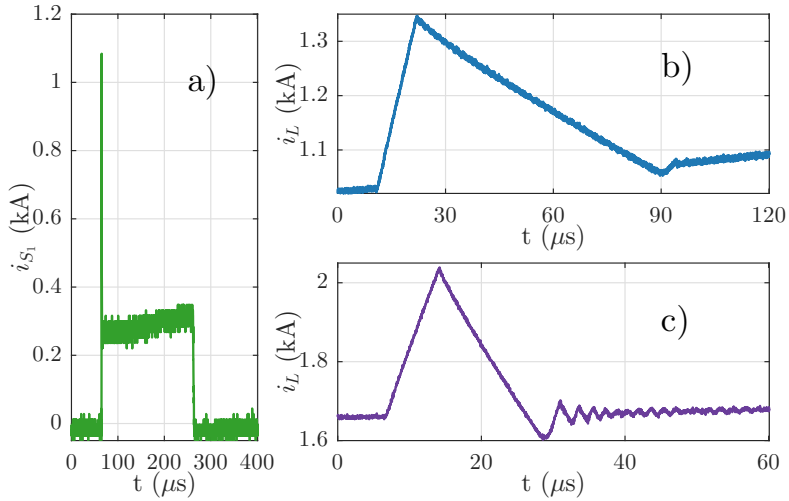

Figure 4.4: Excerpts of currents measured during testing: a) Current through one IGBT of one module when delivering approximately 300 A for 150 µs, showing rapid initial current excursion to 1 kA during diode recovery. b) total current i_L during a current spike of 310 A on top of 1 kA, exhibiting soft recovery at $t = 90\,\mu\mathrm{s}$; c) total current i_L during current spike of 380 A on top of 1.7 kA followed by snappy diode recovery at $t = 26\,\mu\mathrm{s}$.

the diode. A reverse recovery failure of a diode (after the module was used with even smaller inductance and gradients higher than $50\,\mathrm{A\,\mu s^{-1}}$) and the resulting blown fuse and destroyed IGBT has led to the only appreciable downtime FPDCS over its period of use.

4.1.4. Stray Inductances of Connections

The considerable current gradients of up to $50\,\mathrm{kA\,ms^{-1}}$ lead to extensive voltage drops along any inductance in series with the load. In this case, the entirety of the parts between points E and A in figure 4.1 is considered as load, including several meters of cabling necessary to connect the load in question. This additional stray inductance has to be considered if aiming for $\mathrm{d}i/\mathrm{d}t$ higher than $10\,\mathrm{kA\,ms^{-1}}$. Initially, the FPDCS was located in a separate room, some distance away from the devices under test and connected through bus bars of 12 µH.

Since FPDCS was grounded at the capacitors (point A in figure 4.1), a worst case drop of 600 V along these bus bars meant that the low voltage side of the load reached 300 V, making differential voltage measurements and potential free current measurements inevitable. During a major rebuild of FPDCS in 2015, the distance between source modules and loads was shortened by a factor of five, lowering the inductive voltage drops substantially. Additionally, the grounding scheme of the modules was revised in order to remove all ground connections during tests except for one which can be freely placed by the user. This not only enables the use of a shunt resistor for current measurement but also provides the ability to directly measure the absolute load voltage if the low voltage side of the load is chosen as the designated ground point. The current measurement was also improved during this rebuild, as described in section 4.2.2.

4.1.5. Waveform for Arc Characterization

The most important fact about the current waveform is, that it does not try to replicate actual switching cases. The DUT is not a complete DC breaker, but only the gas blast interrupter (cf. section 4.2). This interrupter is stressed with a predetermined waveform that is designed to extract as much information as possible about the arc behaviour, rather than to be a realistic test case that is actually interrupted. To create these test currents, the FPDCS was used with modules 1 and 2 set to the maximum inductance of 4.5 mH, and the third to 50 µH. Modules 1 and 2 allow ramping the current slowly enough to be considered steady state for the arc at all times, while module 3 can superimpose current transients of below 100 µs in length. At all times, the current source is capable of forcing the current through the interrupter, i.e. the interrupter cannot interrupt itself, but the current only goes to zero after the source stops supplying energy.
Each experiment consisted of two phases, and an example is shown in the top graph of figure 4.5. During the pre-current phase (0 ms to 77 ms in figure 4.5), only a small current is flowing while the downstream contact moves from the closed position to the open position. This way, an arc is established, without dissipating too much energy. The pre-current should be as small as possible, to minimize nozzle erosion, and also to keep the energy in the capacitors

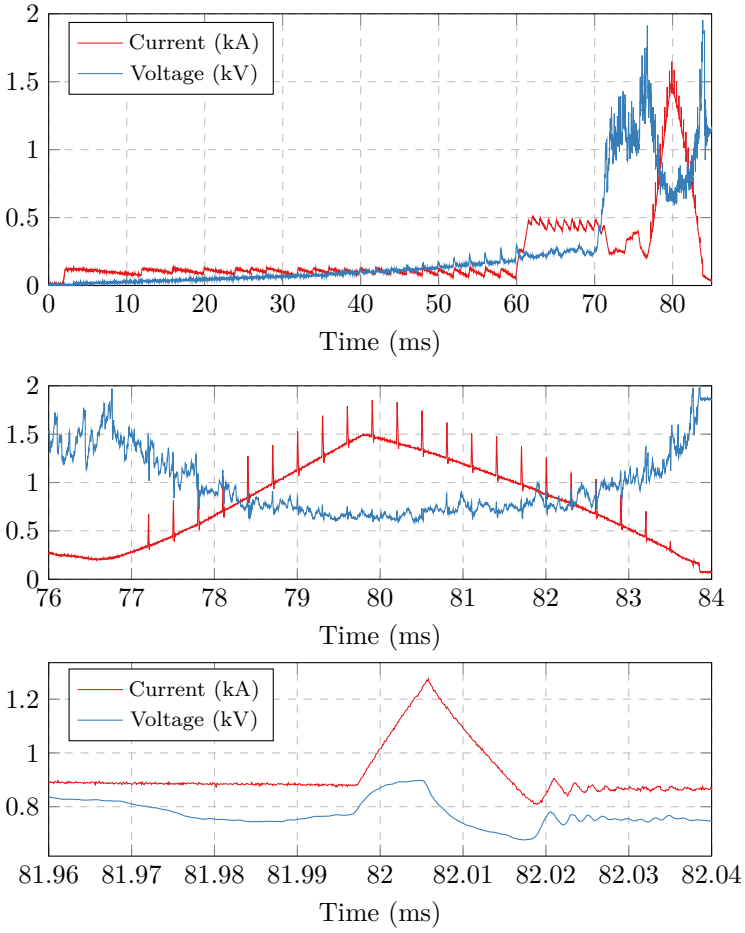

Figure 4.5: Typical waveform used to characterize arc behaviour. Top: total experiment duration. Current starts at 1.5 ms, contacts separate at 3 ms, and reach final position around 75 ms. A low pre-current between 100 A to 200 A is held during unblown contact separation. As soon as the gas flow starts in the nozzle (at 70 ms in this case) a higher pre-current is needed to prevent the current going to zero. Here a test is shown where this is 500 A, but for the actual results the maximum pre-current was reduced to around 300 A by choosing a higher switching frequency (see figure 4.29). Middle: actual high current phase during which the arc is characterized. The slow current ramp in between the current spikes is used for the static characterization. Bottom: one of the fast current transients, during which the dynamic behaviour is obtained.

high until the main-current phase starts. Towards the end of this phase, the valves of the blowing system are opened (60 ms to 77 ms). To prevent accidental interruption, the current is slightly increased. As soon as the gas flow has reached a steady state and the contact has stopped its movement at the final position, the main current phase is started (77 ms to 84 ms). During this time, the current is ramped up to 1.6 kA and down to zero again over a timespan of around 10 ms for most experiments. If the dynamic arc behaviour is to be determined, fast transients are be superimposed, usually with rise times around 10 µs and fall times between 10 µs to 30 µs. A typical example is shown in the bottom graph of figure 4.5. The main features of the arc can already be observed in that figure: The middle graph shows lower voltage with higher current, i.e. negative differential resistance $\mathrm{d}u/\mathrm{d}i$, which is discussed more detailed in section 4.3.1. The bottom graph shows the dynamic response of the arc to fast current transients. The arc cannot change its conductance infinitively fast, which results in a delayed change in voltage to fast changes in current. This dynamic behaviour is discussed in section 4.3.3.
For the ablation characterization measurements shown in section 4.5 and 5.2, the current was instead increased and held at its set value for 10 ms, as shown in figure 4.29. All results that are shown in chapter 5 are calculated only from the values measured during the main current phase.

4.2. Model Gas Blast Interrupter

This section contains content from [BF16, BFF17].
To study arcs, the model interrupter which was initially built by Michael Walter and described in [Wal13] is used. It includes independent contact movement and blowing systems, and uses air as blowing gas in a single flow direction configuration. Contacts are copper tungsten (WCu) electrodes, similar to the material used in commercial interrupters. The downstream contact is moved by a pneumatic cylinder, which takes between 50 ms and 90 ms to move from closed state to the desired final position, which is a travel of 40 mm to 100 mm. The blowing system is realized by 8 bottles of 1.5 L volume each, which are arranged radially around a central

mixing volume. The bottles are filled with the desired pressure prior to each experiment, and discharged into the mixing volume using fast acting valves. Thus the inlet pressure is variable, the exhaust pressure is always fixed at 1 bar abs. Figure 4.6 shows a photograph with the main components, figure 4.7 and 4.8 shows details of the nozzle and contacts. A cross section of the interrupter is shown in figure 4.9, the blue arrows indicate the gas flow from 2 of the eight bottles.

In order to be able to use simple 1D fluid dynamic simulations for experiments without current (cold flow), the model interrupter was adapted since the work of Walter [Wal13] (see colored pieces in figure 4.9). Sharp changes in cross section along the nozzle axis lead to flow separation from the wall and highly turbulent zones right before or after the edges. To obtain more homogeneous flow conditions throughout the nozzle, the inlet section where the gas flow of the eight gas bottles of the blowing system is combined was redesigned (orange and grey parts). The cylindrical nozzle was replaced by a converging-diverging design without any sharp changes in area (green part). At the same time, the upstream contact was replaced by a thinner pin with 5 mm diameter, which is closer to the effective arc diameter. The mounting of both contact pins allows for the axial position (α and β in figure 4.9) to be varied. Therefore, experiments where the arc burns in different sections of the converging-diverging nozzle are possible. Using pins of only 5 mm in diameter is not feasible in real breakers since they would erode too fast. Nevertheless, the thin pin was chosen because the previously used contact with 19 mm also represents a jump in fluid dynamic cross section at its end, which probably induced flow separation and 3D turbulences like Kármán vortices that cannot be accounted for in a 1D model. No qualitative 3D cold flow simulations were performed, but high speed footage strongly indicated the presence of those. Discussions with members of the fluid dynamics group concluded that the pin should be as this as feasible to avoid this. Additionally, the cross sectional area of the contact should be much smaller than the area of the nozzle throat for the measurements described below, as changing the contact positions should influence flow conditions of the blowing gas as little as possible. The exact value of 5 mm was chosen due to easily available material with that diameter, and considered a good compromise, because

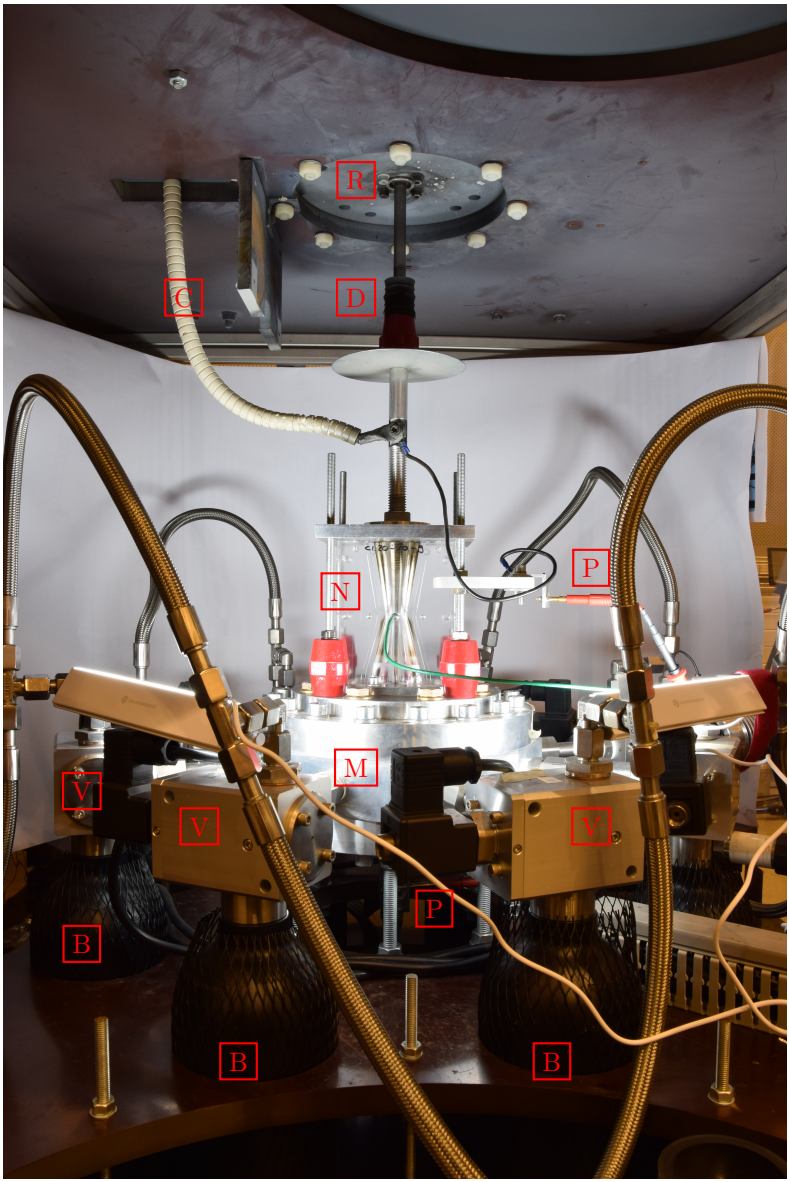

Figure 4.6: Entire model interrupter. Three of the eight bottles are indicated with [B], which are connected to high speed valves [V], which allow flow into mixing volume [M] and nozzle [N] into ambient air. The downstream contact can be moved by a pneumatic cylinder rod [R], and is damped by a rubber damper [D]. Voltage probes are connected to both upstream and downstream electrodes [P]. Current is supplied with positive polarity to moving electrode [C], and returns back to the current source close to ground potential.

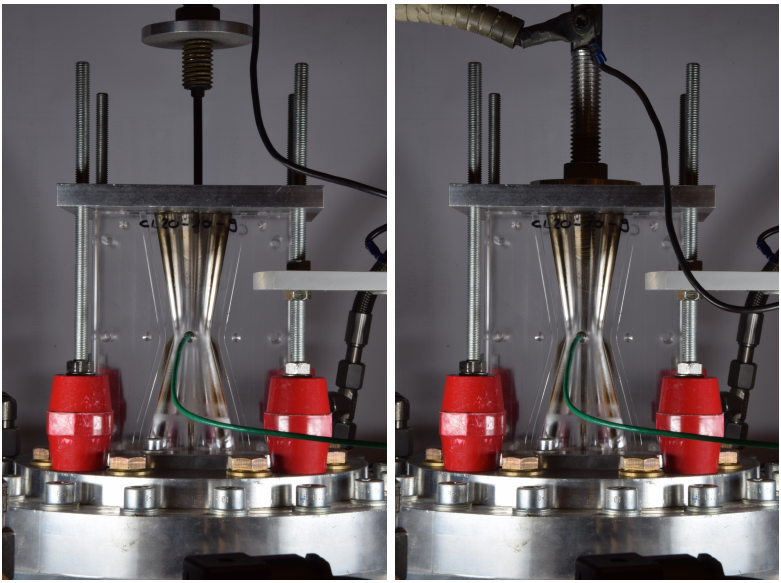

Figure 4.7: Closeup of nozzle and contacts fully assembled (sealing cord missing in groove between nozzle halves, dovel pins and screws joining the nozzle halves are missing), in open (left) and closed (right) position. Flow is from bottom up. The green cable is attached to the pressure sensor at the nozzle throat.

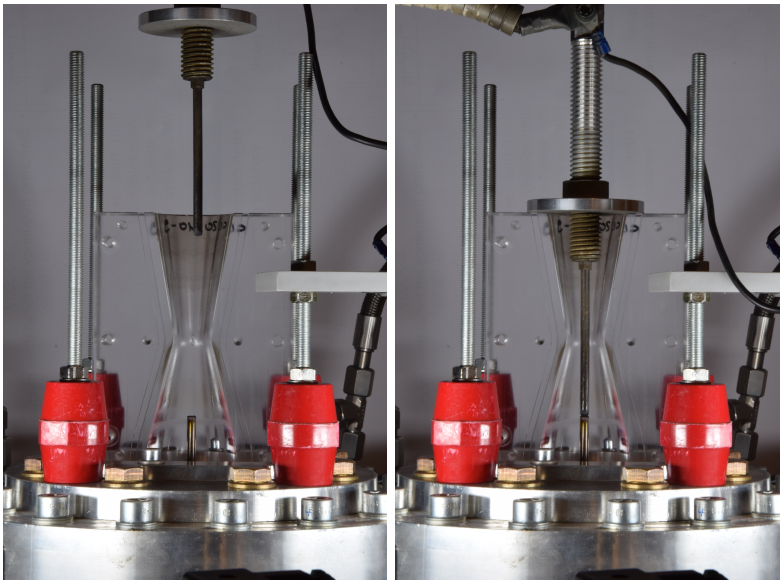

Figure 4.8: Closeup of nozzle and contacts with clamping plate and one nozzle half removed, in open (left) and closed (right) position. Both contacts are WCu pins of 5 mm diameter. Their position can be freely adjusted using a stuffing box mechanism similar to mechanic pencils. The disc at the moving contact is wider than the nozzle exit and can be adjusted to close the nozzle exactly when the butt contacts touch. This was needed to keep air out of the nozzle after flushing the nozzle when other gases were used.

it had still had enough cross section to have negligible resistance. With a minimal nozzle throat diameter of 20 mm and a contact pin of 5 mm, the throat area decreases by only 1/16 if the upstream pin is moved downstream to (or past) the throat position which is considered negligible.
The operating sequence of the model interrupter is as follows. In preparation for one test, 8 gas bottles with 1.5 L capacity each are filled with the blowing gas to the desired pressure. The downstream contact is mounted on a pneumatic piston, which moves it inside the nozzle so that it touches the upstream contact. The experiment is started by supplying a pre-current of small amplitude, usually between 100 A to 200 A, for about 70 ms. During this time, the downstream contact is moved to the desired position by the pneumatic actuator, drawing an arc in the nozzle. Towards the end of the movement, the source current is increased slightly (around 300A) to prevent arc extinction and then the 8 bottles are discharged into the mixing volume upstream of the nozzle, starting the gas flow. The jitter of the 8 high speed valves is below 2 ms, pressure build-up at the nozzle inlet takes about 10 ms. The experiment is synchronized so that this point of steady gas flow is reached when the downstream contact has reached its final position and stopped moving. At this point, the main current waveform is started by the current source, i.e. either the one shown in figure 4.25, or figure 4.29, depending on the measurement performed. The main current period lasts approximately 10 ms. In this time, the blow pressure stays reasonably constant, the discharge in this first period is around 5% in 10 ms, i.e. a pressure decrease from 8.0 bar abs. to 7.6 bar abs. The pressure given in the results sections refers to the pressure at the nozzle inlet, at the time when the main current phase starts.

4.2.1. Nozzle Assembly

This section contains content from [BFF17] and [BVF19]
The nozzle assembly is held down by only four screws, and is therefore easy to disassemble. Since no gas handling is required to access the parts, it is possible to remove and reinstall the nozzle (green and purple parts in figure 4.9) in a matter of minutes. This made it possible to determine the ablation after each test in reasonable time.

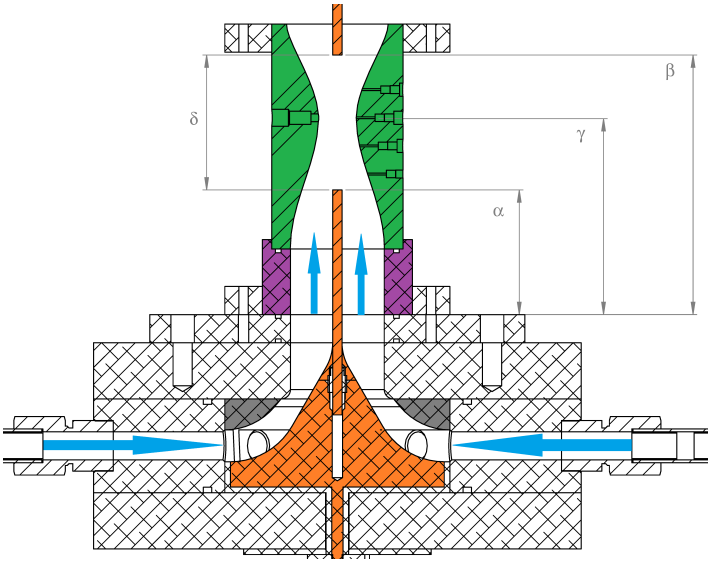

Figure 4.9: Model interrupter setup. Jumps in fluid dynamic cross section were reduced compared to the work of Walter [Wal13] by changing the upstream contact to a 5 mm pin, adding a new mounting piece which transitions smoothly to 5 mm (orange), and adding a toriod-shaped part (grey). The nozzle (green) changes its cross section smoothly without edges. The cylindrical adapter piece (purple) was only used in some of the experiments, for example for holding the inserts or for measurements in which the contacts were placed far upstream relative to the throat. To uniquely describe the contact and nozzle geometry, the distance from a reference point is used, and specified in mm throughout this manuscript. The upstream contact position is denoted by α, the downstream contact position by β. For the standard nozzle used, throat position γ is fixed at 105 mm if the purple adapter is installed, and at 70 mm in case it is removed. $\delta = \beta - \alpha$ denotes the length of the arc.

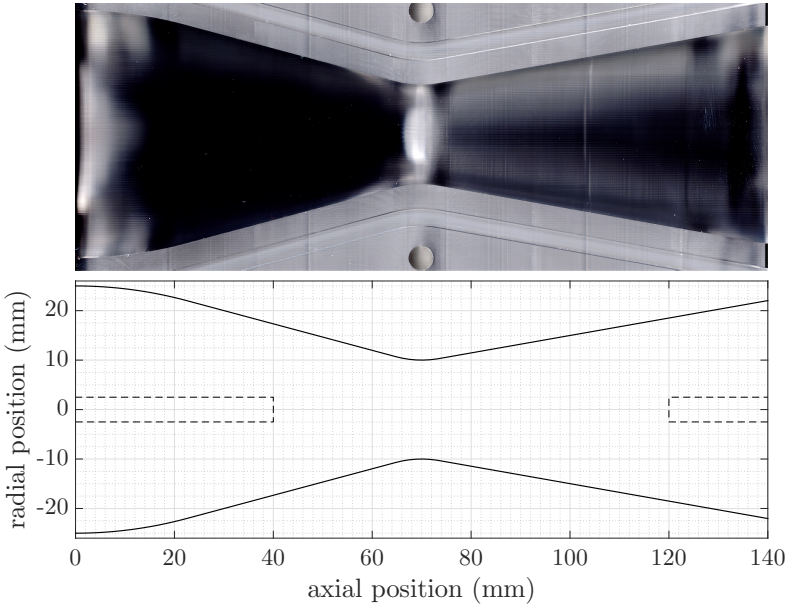

Figure 4.10: Top: Image of one nozzle half as captured by flatbed scanner. The contour can be seen, as well as the grooves for the sealing cord and two of the six holes for dowel pins. Bottom: Extracted nozzle contour (solid), and position of contacts (dashed). Gasflow is from left to right, cathode is left, anode right.

For the nozzle material PMMA was chosen because it is transparent, making it possible to observe the arc. To allow separation along the axis of cylindrical symmetry, each nozzle consisted of two identical parts. This was achieved by milling the contour into two rectangular blocks of PMMA, which were bolted together. To ensure tightness, a rubber seal in a groove was used, and the alignment was guaranteed by dowel pins. Separating the nozzle allowed scanning the contour line in between experiments to track the changes in geometry, as described in section 4.5.

The nozzle geometry and a scan of one nozzle half is shown in figure 4.10. This is the standard nozzle, used for the majority of experiments shown in chapter 5. The inlet directly attaches to the inlet pressure volume and has a diameter of 50 mm. Both the

converging and the diverging part are conical, with half angles of 15° and 10° respectively. The throat is 70 mm after the inlet and is 20 mm in diameter initially. The conical parts were chosen as the simplest single-flow reference geometry, similar to the nozzles used in literature [HKN+74]. The diverging half angle is the maximum possible without flow separation, and the converging part was designed to connect to the mixing volume with a smooth curve without sharp corners or jumps in cross section.

To keep the results comparable, nozzles need to be exchanged often, because widening of the throat diameter by 1 mm already increases the throat area by 10%.

The contacts are copper-tungsten rods with 5 mm diameter, which are at the indicated axial positions of 40 mm and 120 mm. After the publication of [BFF17] there was a strong suspicion that ablation onset could be the reason for $\mathrm{d}u/\mathrm{d}i$ becoming zero. To confirm causality, a material with as little ablation as possible was searched. The company *Brandenburger Isoliertechnik* offers ablation resistant composite material sold under the trade name *S5000*, which was tested. The same dividable nozzle shape as for the PMMA nozzles was machined, to be able to use the scanning technique described in section 4.5. Figure 4.11 shows a picture of these before the tests, and figure 5.11 after the tests.

For the results presented in [BVF19] and section 5.5 small changes were implemented compared to the setup for the previous experiments. Notably, a lid was attached to the downstream pin, that allowed to close the nozzle before experiments, and therefore enable the use of other gases. To prepare the system before the upstream valves are opened, the lid is closed by the pneumatic cylinder moving the contact. While still actively pressed closed, the blowing system is activated, to flush the bottles and nozzle through a small slit between lid and nozzle exit created by the overpressure. This slit closes as soon as the gas flow stops, preventing air from entering the nozzle, and thus ensures the blowing system is filled only with the blowing gas.

Laminar or turbulent gas flow in a tube is mainly dependent on the velocity, the diameter, the gas density and the viscosity. To define whether a flow is laminar or turbulent, the Reynolds number is a

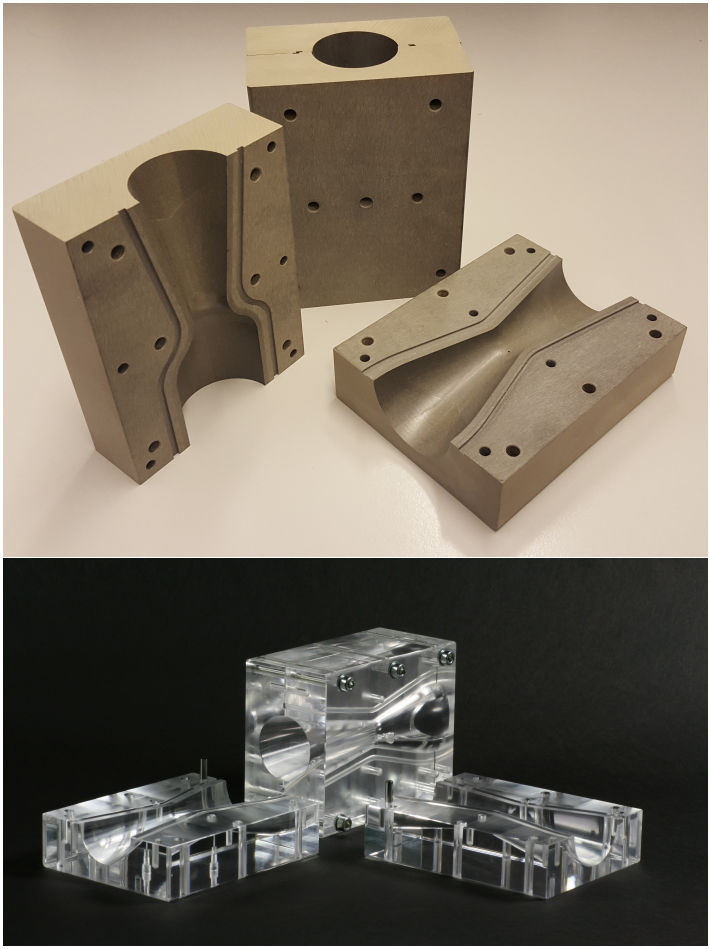

Figure 4.11: Dividable nozzles made from PMMA and S5000 ablation resistant material, before use.

Figure 4.12: Overview (left) and closeup (right) of the 5 mm WCu contact pins. The downstream pin (left in both pictures) was always the anode. The initially cylindrical tip erodes into a convex tip. Additionally, many brighter spots can be seen on the side of the pin, these were created when the arc root was blown downstream along the side of the pin, as shown in figure 4.20. The upstream pin was always cathode, and showed different erosion. The tip became concave, and cracks formed at the surface.

good indicator.

$$\text{Reynolds number} = \frac{v \cdot \rho \cdot d}{\eta} \tag{4.1}$$

with the tube's diameter d, the velocity v, the density ρ, and the dynamic viscosity η of the gas. For a Reynolds number below 2000, the fluid's flow is assumed to be laminar, between 2000 and 4000 there is a transitional flow and above 4000 the gas flow is turbulent. A low Reynolds number and hence, a laminar flow can be accomplished by decreasing the velocity and the tube's diameter. If the critical velocity is not exceeded, a flow through a tube is generally laminar and dependent on the viscosity. On the other hand, laminar flow can be disturbed by sudden changes in flow cross section, described by the Borda-Carnot equation. A flow through an orifice into a pipe with wider cross section is turbulent and dependent on the density. Therefore, it is possible to straighten a flow by inserting a honeycomb or many small straws with small diameter into a large pipe, decreasing the Reynolds number. Likewise, a turbulent flow can be provoked

by inserting a perforated plate which acts as orifice.
In order to change the inlet conditions of the blowing gas to change the level of turbulence, some parts were added into the purple adapter (see figure 4.9) for one measurement series. Three flow straightners, hive-like grids of different length and hole diameter, that should help dissipate turbulent patterns and homogenize the inlet flow. They are shown in figure 4.13. To introduce more turbulent inlet conditions, perforated metal plates were used, which block 61% and 68% of the cross section respectively, and introduce additional turbulence. Those are shown in figure 4.14. It must be noted, that it cannot be expected to achieve laminar flow in the nozzle inlet. The density and velocity of the gas are too high, even with the smallest hole size of 3 mm the Reynolds number is around 50'000. However, inserting something in the inlet was an easy way to test if turbulence can be influenced, and if that has an impact on the arc behaviour.
Lastly, a different nozzle shape with a shorter converging section was studied, this shape is shown with red dashed lines in figure 4.15.

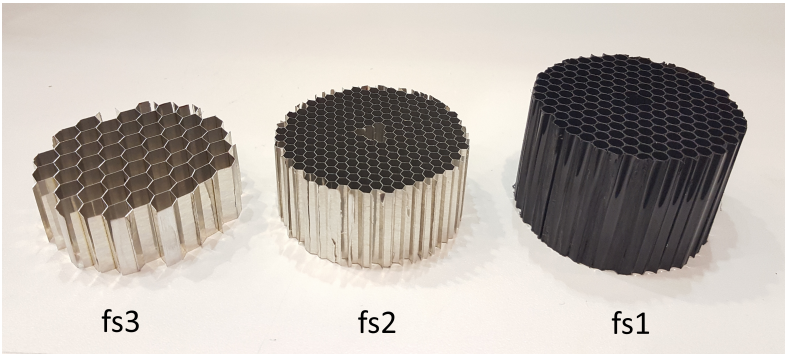

Figure 4.13: Flow straighteners 1 to 3, used in the inlet condition variation, as described in section 5.4 and figure 5.19. Diameter of the holes are (from left to right) 7 mm, 3.1 mm and 4 mm. The length in flow direction is 19 mm, 25 mm and 38 mm respectively.

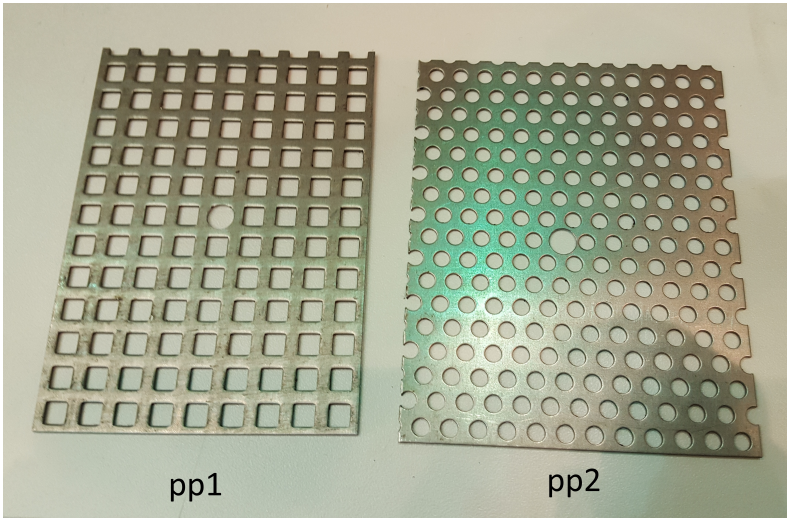

Figure 4.14: Perforated plate 1 and 2, inserted in the nozzle inlet to provoke more turbulent flow. The square holes are 5 mm by 5 mm, in a 8 mm grid, i.e. 39% of the grid is open, and 61% are blocked. The round holes are 4 mm in diameter, and arranged in a hexagonal grid with a spacing of 6.5 mm. This leads to 31% open area, and 69% blocked.

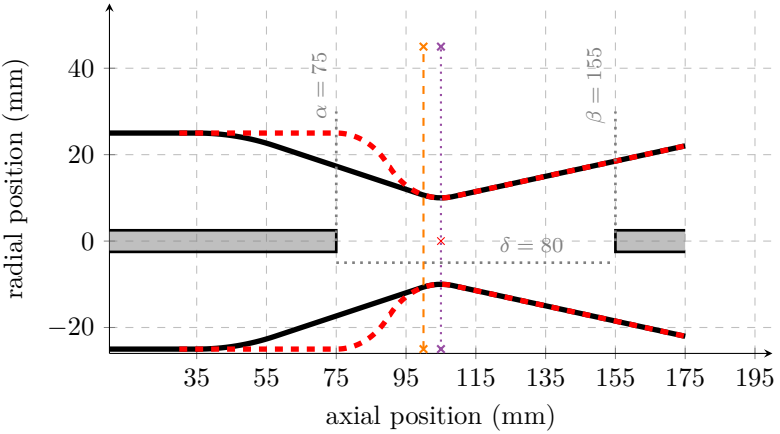

Figure 4.15: Nozzle setup, gas flow direction is from left to right. α indicates upstream contact position, β the downstream contact position. The throat position is at 105 mm (red cross). The black solid line indicates the nozzle contour which was used for the majority of experiments. Converging and diverging parts are both conical, with half angle of 15° and 10° respectively. The red dashed line indicates the contour of a nozzle variant with a shorter converging segment with up to 45° half angle, leading to higher acceleration in that segment. The purple line indicates the throat position, and the orange line is the position where the arc radius is evaluated, as shown in figure 5.15.

4.2.2. Measurement Equipment

This section contains content from [BF16]

To measure the $\mathrm{d}u/\mathrm{d}i$ of the arc precisely, measurement equipment with high accuracy and temporal resolution is needed. The voltage is measured using two RC dividers (*PPE4KV* by LeCroy, 1:100 divider with 400 MHz nominal bandwidth) connected to both contact pins of the interrupter. Although the upstream electrode is connected to the same ground potential as the reference of the oscilloscopes, hard switching of power semiconductors in the current source introduce fast transients which are seen as common mode voltages due to the stray inductance of the connecting cables. These are eliminated in post-processing by subtraction of the two voltage signals. The probes have to be attached to the circuit as close as possible to the arcing pins, to minimize inductive voltage drop, especially during the current transient with high gradients, which are used to determine the dynamic arc behaviour. The distance between the probes is below half a meter of cabling, which gives acceptable error due to stray inductance.

The current is measured by a custom built current sensor similar to the one described in [HKRS10], which was calibrated by comparing it to shunt resistor measurements. It has enough bandwidth to record the current waveforms shown in 4.5, including the sharp changes in $\mathrm{d}i/\mathrm{d}t$ at the start, the peak and the end of the triangular transients. Voltage and current signals are recorded with a 12 bit oscilloscope at a sampling rate of $100\,\mathrm{MS\,s^{-1}}$. This rate is faster than changes in arc voltage would require, but is needed for reliable common mode voltage rejection. Additionally, bandwidth can be traded for increased vertical resolution in post-processing by low pass filtering the signal, which was done using a fifth order Butterworth filter with cutoff frequency of 10 MHz. One waveform is shown in figure 4.16 as an example.

Besides voltage and pressure, also pressure is measured during experiments at three locations by different sensors made by *Kistler*. The first one is type *K-Line RAG A50*, mounted to one of the bottles. It can be also used to verify the filling pressure before experiments. The second sensor, type *4073A20* is installed in the mixing volume, between the radial inlets of two bottles. A third sensor, type *4005B*

A20 can be installed in the nozzle, provided there are threaded holes. Figure 4.9 shows these at several positions along the right nozzle wall, but for the vast majority of measurements it was installed at the nozzle throat. An interesting observation was the fact that this sensor is sensitive to light emitted by the arc. It therefore has to be shielded, a lose piece of aluminum foil in the hole in front of the sensor proved to block the light very effectively, while not introducing any error to the pressure measurement.

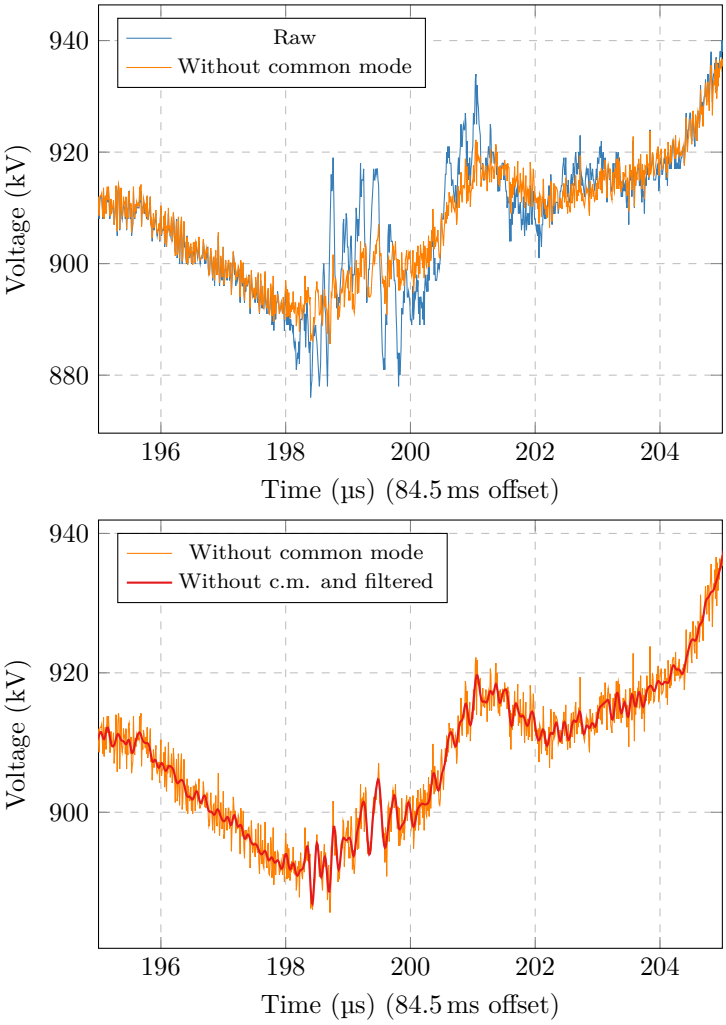

Figure 4.16: Arc voltage as function of time, showing the signal postprocessing. First, the common mode is eliminated by subtracting the voltage measured at the downstream contact from the upstream contact signal, as shown in the top plot. Common mode noise usually is introduced by switching of the IGBTs of the source, which happens at 198 µs in that case. The data is zoomed in around the 84 ms mark in figure 4.17), and shows the last turn-on which starts the main current period. Afterwards, a 5th order butterworth filter is applied, with 10 MHz cutoff frequency. This sufficiently damps the quantization noise of the DSO, but does not sacrifice too much bandwidth, which is needed for the determination of τ, as explained in section 4.3.3.

4.3. Arc Characterization

Blown arcs are difficult to characterize, since they are a complex phenomenon involving many different physical processes. To describe the properties of one setup and compare it to others, some metrics are needed. For the application in passive oscillation switchgear, one can categorize different changes in arc behaviour according to their consequences for that specific application. The most important property is the static voltage current characteristic, i.e. how the voltage drop of the arc changes with changing current, assuming perfectly steady conditions. This is covered in section 4.3.1.

The static $u(i)$ curve is not perfectly static. There are always random fluctuations of arc voltage, which are not coupled to changes the controllable boundary conditions like current or gas flow rate. One prime example is moving arc roots downstream on the contact surface, which changes the length of the arc column. Those fluctuations are covered in section 4.3.2.

As a third category, the arc time constant defines the dynamic changes of the arc. If there was an instantaneous change in current amplitude (or other boundary conditions, like flow conditions), the arc will not be instantly in the steady state corresponding to those, but will need some relaxation time τ to adapt. Since the current through the nominal path oscillates of passive oscillation switches with rather high frequency, the arc has to react to fast changing currents. Depending on the oscillation frequency, the arc may or may not react fast enough to be in quasi-static regime. Section 4.3.3 describes how this dynamic behaviour is characterized.

One important factor for arc characterization is how many experiments are performed. Having many identical experiments is desired in order to be able to have enough results to do a statistical analysis. However, conducting many experiments takes time and also wears the nozzle. To ensure identical conditions, the nozzle has to be replaced before its shape is changed too much due to erosion. Both of these issues call for methods to extract as much data as possible from each experiment. The current waveform shown in figure 4.5 combined with the methods described in the following sections allow the determination of the static and dynamic arc behaviour as function of current in one single experiment, which is more convenient

than tests with an actual passive oscillation switch with interrupter and parallel LC path.

4.3.1. Static Conditions

This section contains content from [BF16].
As described in section 1.3, the nominal current path needs to have negative differential resistance, and section 1.4 already mentioned that this is the case for arcs in gas blast interrupters. For deeper analysis, the voltage current characteristic of the model interrupter needs to be measured. To determine the static $u(i)$ curve of a given setup, the current waveform described in section 4.1.5 is used, although the current spikes can be omitted, as shown in figure 4.17. The static arc voltage is obtained by ramping the current slow enough ($0.3\,\mathrm{kA\,ms^{-1}}$ is typical) that the arc has sufficient time to equilibrate, and excluding the time of the superimposed current spikes, if there are any. During the slow ramp, the dynamic reaction of the arc is negligible, and the arc voltage at any given time is assumed to be the static value for the current flowing at that moment. The black dots in figure 4.18 show a typical example, obtained during one experiment. A general trend is visible, but the arc voltage can vary strongly at certain times, which makes it difficult to attribute one voltage value to a given current value. To compare different setups, a fluctuation-free $u(i)$ is needed, especially if the derivative $\mathrm{d}u/\mathrm{d}i$ is calculated.
A metric was introduced that is capable of describing the interesting features of those curves. The voltage and current data is split up into bins (usually a width of 150 A was chosen) and for each bin the median of the voltage is determined. In order to gain more statistical significance, several experiments with identical conditions are combined, meaning that all data points of all experiments which lie in the respective current bin are evaluated together. By combining at least two experiments, with each crossing all bins twice (once on the rising slope, once falling), four independent periods of time which combine the data of at least 1 ms end up in each bin. The differential resistance is then obtained by piecewise calculating the slope between the median values. An example is shown in figure 4.19. The values obtained with this method are intrinsically robust to outliers and

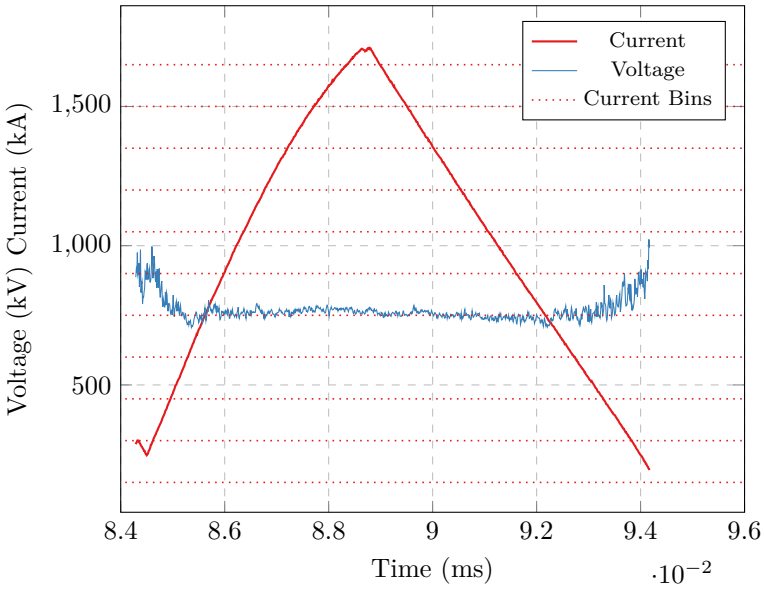

Figure 4.17: Arc voltage and current as function of time, for one experiment. Arc length $\delta = 80\,\text{mm}$, upstream contact position $\alpha = 75\,\text{mm}$, downstream position $\beta = 155\,\text{mm}$.

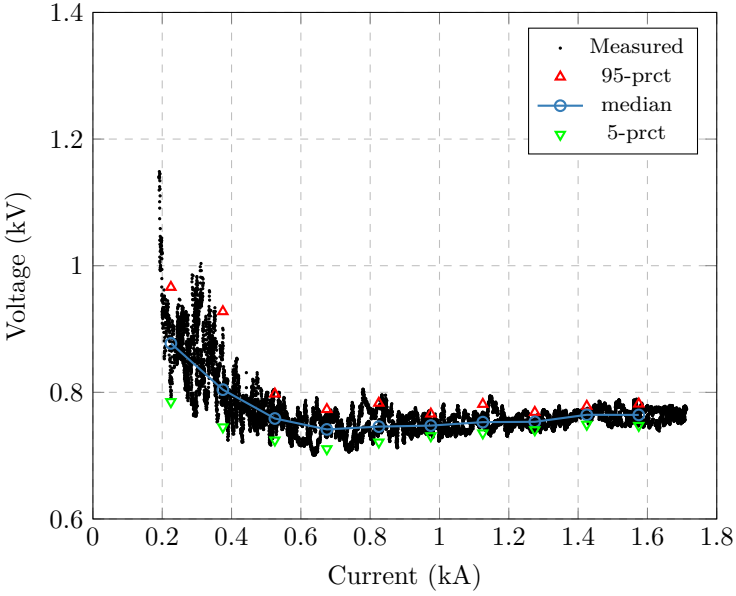

Figure 4.18: Arc voltage as function of current. This plot is obtained by putting each sample point of the data shown in figure 4.17 to the respective position. Since data is sampled at $100\,\mathrm{MS\,s^{-1}}$, roughly one million data points result from the 10 ms long main current period. Only every 1000th is shown here, in black. These datapoints are then sorted into current bins of 150 A width, and the median, as well as the 5- and 95-percentile are calculated for each bin, as indicated. For the data shown in the results sections, the data points of at least two experiments were combined, to ensure each bin contains data from at least 1 ms of measurement.

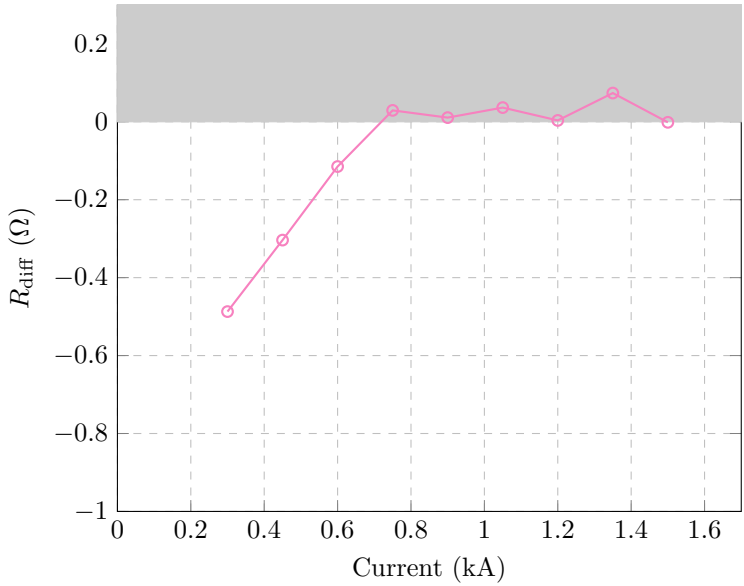

Figure 4.19: Differential arc resistance, determined by calculating the slope between the median data points of figure 4.18. Since the parasitic resistance of the LC-arc loop needs to be added in real applications, values higher than about $-0.1\,\Omega$ are probably not negative enough for reliable amplification.

show the general trend, but cannot describe the voltage fluctuations. These are covered in the next section.

4.3.2. Fluctuations

As mentioned in the previous section, the arc voltage fluctuates even if the external conditions are not changing. This is a potential problem in passive oscillation switches, if the random changes in voltage are higher than the changes due to change in current, and therefore there is no negative $\mathrm{d}u/\mathrm{d}i$ anymore. Most of these voltage fluctuations can be attributed to deviations from the idealized picture of a cylindrical arc, that it is a stable plasma column in the center of the symmetric nozzle, with a clear arc boundary, and arc roots do not move on the electrodes. This is not true, gas flow is turbulent,

which induces random deviations, which lead to instabilities in the arc column. Depending on the flow conditions, these can be quite significant. An extreme case is illustrated in figure 4.20, where the arc does not stay in the nozzle center, leading to an elongation of more than a factor of two. To quantify those fluctuations, additionally to the median voltage, the 5-percentile and the 95-percentile of the arc voltage are also calculated for each current bin. These are shown as red upwards and green downwards triangles in figure 4.18. The percentiles are chosen arbitrarily (10 and 90 could have been used as well), to give a metric for the lower and upper limit of the arc voltage as a function of current. This way, not only a typical voltage current curve is obtained, but also the unpredictable deviations from that voltage curve. An example with extreme fluctuations is shown in figure 4.21. There are very frequent voltage excursions away from the median voltage. Most of these excursions are towards higher values, leading to asymmetrical distance of the percentile from the median value. This is a clear indicator that the fluctuations are not gaussian distributed, and mean plus standard deviation would not be a suitable way to derive an $u(i)$ curve. Specifying the median and other percentiles instead of the mean and standard deviation is a simple yet powerful tool, which was mainly motivated by the lecture and paper of Hanspeter Schmid [SH14]. The three percentiles (5-50-95) allow easy comparison of different setups, with regard to $u(i)$ and the probability of unpredictable deviations from that static curve.

4.3.3. Dynamic Conditions - Determining Arc Time Constant

Parts of this section contain content from [BSF19].
In section 4.3.1, it is assumed that the arc is in a steady state and the energy balance is in equilibrium. The heating power due to the ohmic losses $P_{\text{ohmic}} = u \cdot i$ equals the sum of all cooling terms P_{cool}, which includes radiation losses, convection losses and thermal conduction losses, as described in section 1.4. The arc in this steady state has a certain conductance g_0, which is $g_0 = i_0/u_0$. In most arc models, conductance is assumed to be a function of arc geometry and temperature inside the arc column, and therefore a state variable.

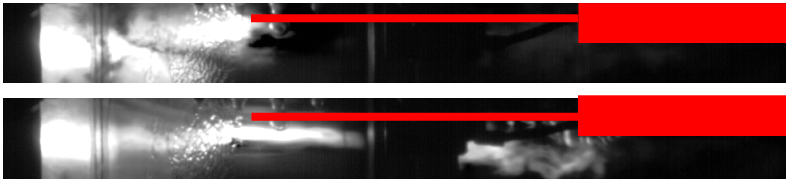

Figure 4.20: High speed images showing arc root movement at downstream contact (indicated in red). Exposure time is 2 us for each frame, time between the two shown frames is 1000 us. The arc root is moved downstream along the contact for more than 80 mm and attached to the thicker part that holds the thin pin, i.e. the arc length more than doubled. The dark band in the middle of the frame is the nozzle holder and nozzle exit, i.e. in the left half, the arc is viewed through the PMMA nozzle, the right half is a direct view.

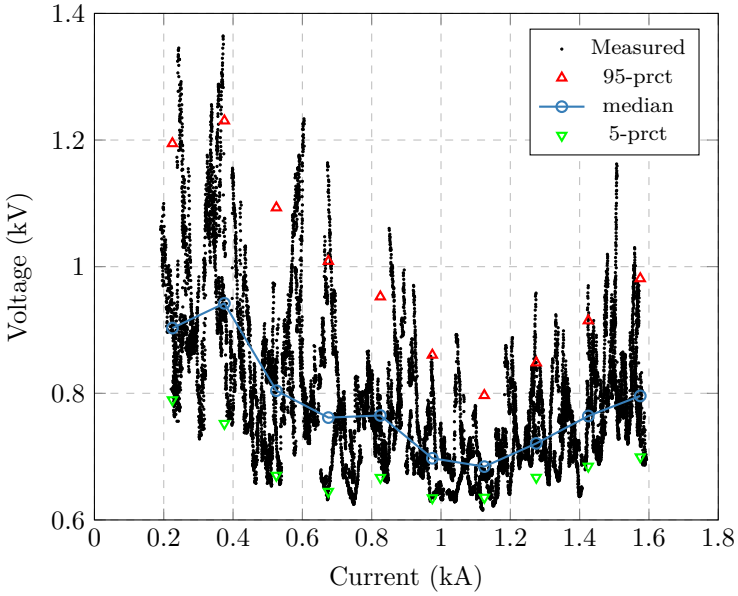

Figure 4.21: Arc voltage as function of current. Arc length $\delta = 80\,\text{mm}$, upstream contact position $\alpha = 15\,\text{mm}$, downstream position $\beta = 95\,\text{mm}$. Similar to figure 4.18, the measured data of one experiment is shown, with only every 1000th data point plotted, to avoid printing one million points.

The response of an arc to dynamic changes in current is generally described by black box models, namely the ones of Mayr and Cassie [May43, Cas39], as summarized in chapter 1. These models assume that the loss terms are a function of g, and cannot change instantaneously. Some time is needed to change to the new equilibrium state, which can be described by a time constant. In case of a current increase form i_0 to i_1, it must be a change that leads to a greater conductance g_1, and in turn to a lower arc voltage u_1. This change requires a certain change of the arc enthalpy, to either increase the arc radius, or the temperature and therefore its conductivity. The required energy has to be supplied by the difference of P_{cool} and $u \cdot i$. The Mayr model is usually used to describe arcs during a few microseconds before and after current zero in AC circuit breakers. It assumes P_{cool} is constant and there is one time constant τ which describes the relaxation process. Cassie, Habedank, Shavemaker and many others [Cas39, Hab93, SvdS00] generalized this, by making P_{cool} and possibly τ a function of g, to describe the high current phase as well. The most general form is therefore

$$\frac{1}{g}\frac{dg}{dt} = \frac{1}{\tau(g)}\left(\frac{ui}{P_{\text{cool}}(g)} - 1\right). \tag{4.2}$$

The physical interpretation of this model is that the arc consists of one energy reservoir (the enthalpy of the heated plasma column) and that the conductance is the fundamental variable to describe its state. For simplicity, the most general form of the transient arc model equation (4.2) will be called *Mayr Equation* throughout the manuscript, although *Cassie Equation* would be equally right or wrong, because the two only differ in how P_{cool} depends on g (see [Kap11, Nak91, KFG$^+$16]).
The literature mentioned above provides different modified models, which assume certain analytic functions for $P_{\text{cool}}(g)$ and $\tau(g)$. Cassie for example assumes a constant voltage during high currents, and Shavemaker combines Mayr and Cassie. Schwarz [Sch73] introduced some additional variables to parameterize $P_{\text{cool}}(g)$ and $\tau(g)$, and more recently also other modifications were published. Khakpour gives a nice overview on quite a few of them [KFG$^+$16]. In the present work, those more specific models were not studied, but the generalized form was used. The only constraint this general form has

is that both $P_{\mathrm{cool}}(g)$ and $\tau(g)$ only depend on g and not on u or i, without specifying a priori what that dependence should be. Other external factors, like contact separation distance and blowing gas flow obviously also impact the arc. The Mayr equation (4.2) assumes those external conditions to remain constant.

This arc model leads to the following behaviour: All changes of external conditions — namely how much current flows through the arc — that take much longer than $5\,\tau$ can be considered quasi-static. The difference between P_{cool} and $u \cdot i$ will always be virtually zero, and the system will be in equilibrium any time.

On the other hand, current variations that happen on a time scale much shorter than τ do not allow the arc to react. The conductance will not change, and the arc will behave like a resistor [May43].

To determine the characteristic time constant τ of a given setup, several possibilities exist [Rij75, Ams77, Rup79, DRWZ83], which were evaluated in previous work [WLF13, Wal13]. As shown in figure 4.22, using a current waveform with a perfect current step with completely constant current before and after, and infinitely high gradient during the step would be the easiest way to determine τ. It would only require fitting an exponential function to the voltage (or conductance) waveform. The top graph in figure 4.22 shows a current step in red, and the voltage response of the arc in blue. The blue dashed line indicates the instantaneous arc voltage, which would occur for $\tau = 0$. The middle graph shows the arc conductance $g = i/u$, and the instantaneous value. The bottom graph shows the ohmic heating power $P_{\mathrm{heat}} = u \cdot i$ in red, and the cooling power $P_{\mathrm{cool}}(g)$ in blue. The latter cannot be measured directly, but is calculated from the static arc characteristic, where $P_{\mathrm{heat}} = P_{\mathrm{cool}}$ can be assumed. Calculating τ from measurements with a staircase shaped current waveform with steep slopes (rise time much faster than τ) and long enough ($>3\tau$) flats afterwards would be trivial. However, it is experimentally impossible to create current steps of $\Delta i \approx 100\,\mathrm{A}$ at current amplitudes between a few 100 A and a few kA with rise times below 1 µs. This would be required to determine τ of axially blown arcs, which typically is in the order of single microseconds. Using the Flexible Pulsed Direct Current Source (as described in [RBF16] and section 4.1), it is nevertheless possible to determine τ reliably, using current transients of triangular wave-

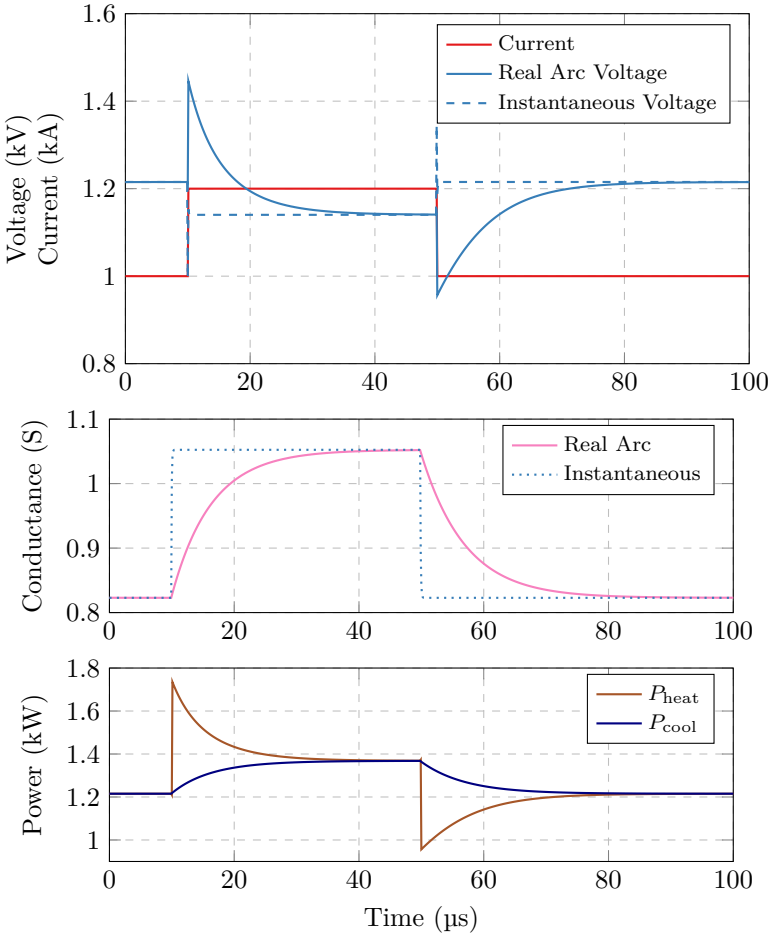

Figure 4.22: Idealized response of an arc with $\tau = 10\,\mu s$ to current steps. Upper graph shows current and voltage, center shows the conductance. The dotted line is the steady state value corresponding to the current flowing at that time, the solid line is calculated by numerically solving the differential equation 4.2. The lower graph shows the cooling term P_{cool} and $P_{\text{heat}} = u \cdot i$. After $\sim 5\,\tau$, both are equal and the arc is in steady state.

shape.

Fitting Algorithm

Determination of τ means finding a solution for which equation (4.2) accurately reproduces the measured results. This requires experimental data of dynamic arc behavior, i.e. current and voltage wave-forms of an arc that is perturbated from a steady state. A quasi-static DC current (gradient lower than $1\,\mathrm{A\,\mu s^{-1}}$) is superimposed with transient current impulses of triangular wave-shape, as shown in figure 4.25. If the rise time and fall time of the current are in the order of magnitude of τ, it is possible to determine τ, by a method proposed in [Wal13].
First of all, a value of τ is guessed. Then, the conductance and voltage response of an arc with the guessed value of τ is calculated. In a third step, the calculated conductance waveform is compared to the measured values i/u, by calculating the root mean square difference. This process is repeated for different values of τ, until a minimum difference is found.
In the present work, an algorithm to solve the Mayr equation was implemented, tested and used to perform the fit. A key requirement to the algorithm is to avoid the need to calculate derivatives of measured signals. Differentiating measured current and voltage signals accurately and with sufficient bandwidth is impossible, due to the inherent decrease of signal to noise ratio of derivatives without using strong low pass filters. The optimized fitting algorithm instead uses the forward Euler method to solve equation (4.2), which makes the following assumptions:

- The arc is in steady state before the current transient, therefore all variables at $t = 0$ are known $g_0 = i_0/u_0$, $P_{cool,0}(g_0) = u_0 i_0$
- During the current transient, τ is a constant value, i.e. changes in g are small enough so $\tau(g)$ can be considered constant.
- During the current transient, $P_{\mathrm{cool}}(g)$ can be linearized, with one point being $P_{\mathrm{cool},0}(g_0)$, and a second point $P_{\mathrm{cool},1}(g_1)$.
- All changes in conductance and voltage during the current impulse are considered to be exclusively due to the Mayr equation

(4.2), i.e. there are no random fluctuations during the transient period due to other reasons like arc root movement etc that would also alter $P_{\mathrm{cool}}(g)$.

With these assumptions, initial conditions and a guessed value for τ and $P_{\mathrm{cool},1}(g_1)$, equation (4.2) can be used to solve for the conductance waveform $g(t)$, if the current waveform $i(t)$ is given. This is done by iteratively calculating $\dot{g}(t)$, $g(t)$ and $u(t)$ for one point in time, using the values from the previous time step. To minimize the error of that method, time steps much smaller than τ have to be used. Since the sampling rate of current and voltage has to be high ($>50\,\mathrm{MS\,s^{-1}}$) to reject common mode noise of the source (see section 4.1), this is not a problem.
The result of one idealized current waveform is shown in figure 4.23. The response of the arc with $\tau = 10\,\mu\mathrm{s}$ depends on the slope and duration of the current spikes. Although the whole process is governed by the rather simple equation (4.2), several different features can be seen. The first spike has a rise time of 4τ, which means the conductance lags behind the instantaneous value, but has a similar shape (see middle plot). This means the voltage (top plot) still follows the static curve, although with a certain shift. For rising current the voltage is higher, for negative $\mathrm{d}i/\mathrm{d}t$ the voltage is below the steady state curve. This shift is a function of $\mathrm{d}i/\mathrm{d}t$ and τ and increases as both increase. Jumps in $\mathrm{d}i/\mathrm{d}t$ as at the start, peak and end of the spike change this shift, and result in similar relaxation as a current step. This effect is seen best on the voltage curve in the top plot of figure 4.23: at $t = 20\,\mu\mathrm{s}$ the spike starts. Initially, the voltage rises, until around $t = 30\,\mu\mathrm{s}$ the "steady lag" is established [1]. From there on, the transient voltage curve follows the steady curve (with the mentioned shift), i.e. $\mathrm{d}u/\mathrm{d}i < 0$ as shown in figure 3.5. It is important to note that sudden jumps in $\mathrm{d}i/\mathrm{d}t$ always lead to resistive behaviour, i.e. $\mathrm{d}u/\mathrm{d}i > 0$ for a certain period, and are therefore detrimental to the goal of passive oscillation. Steep $\mathrm{d}i/\mathrm{d}t$ corresponds to a higher lag, which becomes also unfavourable as soon as the lag becomes significant with respect to the oscillation frequency. This is explained in chapter 3, especially in figures 3.6

[1] Thank you Tim for the great picture of the (slim or fat) cat following the laser pointer with steady speed and distance.

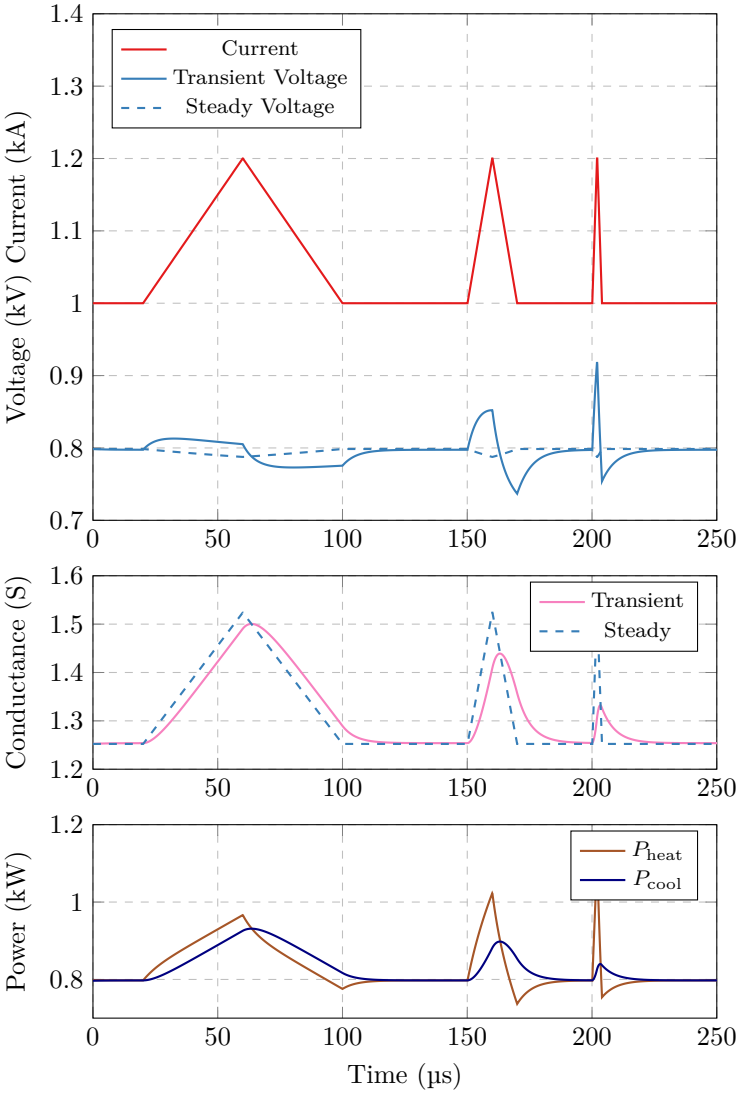

Figure 4.23: Idealized response to triangular current transients. An arc with $\tau = 10\,\mu s$ is assumed. Triangular current transients with rise time $4\,\tau, 1\,\tau$ and $1/4\,\tau$ follow. Solid lines indicate the calulated transient arc response, dashed lines indicate the steady state values, i.e. the ones which would be measured for $\tau = 0$.

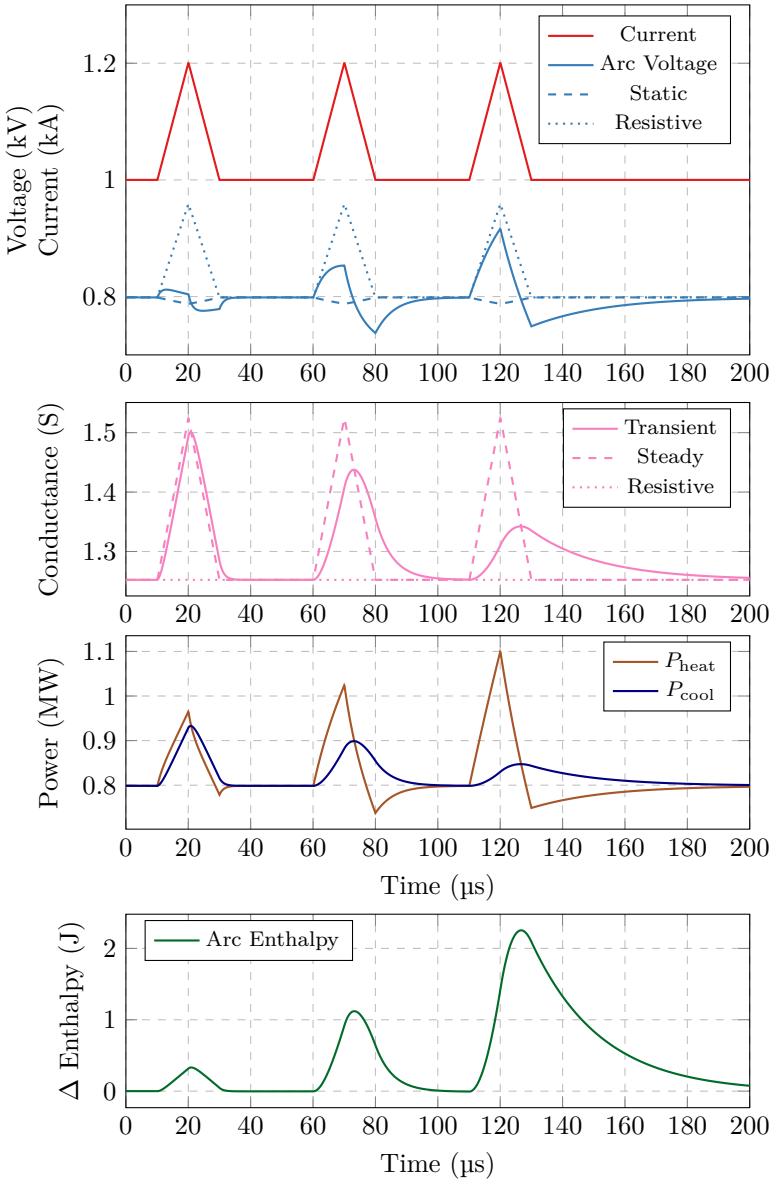

Figure 4.24: Idealized arc response for different values of τ. The arc response to a current spike of 10 µs is simulated. During the first spike, $\tau = 2.5$ µs, during the second $\tau = 10$ µs, and during the last one $\tau = 40$ µs. The ratio of spike rise time to τ is therefore identical to the three spikes in figure 4.23.

and 3.7. However, for the task of determining the arc time constant τ, jumps in current or steep $\mathrm{d}i/\mathrm{d}t$ that lead to voltage transients which then relax towards the steady state are actually needed.

The second spike has a rise time of τ. Here, the lag of the conductance is so significant that the shape of the waveform starts to differ from the hypothetical steady state curve. This also leads to bigger changes of the arc voltage. The last spike has a rise time of $1/4\tau$, meaning the current rises and falls so fast that the conductance can hardly follow. Peak conductance is reached almost at the end of the spike, and afterwards exponential decay follows. For better illustration, figure 4.24 shows three identical current spikes, but each spike is simulated with a different value for τ, to match the rise time/τ-ratios of the spikes in figure 4.23. To aid interpretation, dashed lines show the voltage and conductance values one would obtain for an arc that is always in steady state, i.e. for $\tau = 0$. Dotted lines represent the resistive case, in which the arc conductance does not change at all, i.e. for $\tau = \infty$. In this picture it becomes clear why a rise time around τ as the middle spike is a good current waveform. For this spike, the conductance changes significantly, but at the same time it is also significantly delayed compared to the steady curve. The voltage curve is in between the two extremes during the rising edge, and shows significant undershoot on the falling edge. The left spike with rise time 4τ is too slow for the arc to be transient. Its conductance follows almost exactly the steady state curve, which leads to a small deviation of the voltage from the static $u(i)$ value. This makes it hard to determine a numeric value for τ, especially if the deviation of the voltage curve becomes small enough to be in the order of the inductive voltage drop between the two voltage probes. The rightmost spike is too fast for the arc to properly react at all. Its conductance does not change as much, and the voltage follows the resistive curve.

For the vast majority of all experiments, τ was determined to be in the range from 1 µs to 20 µs, and therefore a triangular current pulse with approximately 10 µs rise and fall time, and an amplitude between 100 A and 300 A was chosen. This requires current gradients in the range from $10\,\mathrm{A\,\mu s^{-1}}$ to $100\,\mathrm{A\,\mu s^{-1}}$, which is possible with the FPDCS [RBF16]. In principle it would be possible to extend the time used for the fit beyond the end of the fast current spike, where

the conductance decays exponentially, making the very fast spike also a valuable waveform. However, higher $\mathrm{d}i/\mathrm{d}t$ generally increases problems with the voltage measurement as well as the current source. First of all, with higher current gradients the inductive voltage drop rises and at some point it would be necessary to account for it before the conductance can be fitted. This can be seen already in the example measurement shown in figure 4.25. The measured conductance (i/u, pink in the second graph) drops at the moment the current starts to rise and stays below the fit, until it increases sharply peak current. Secondly, snappy diode recovery becomes an issue, which leads to current oscillations at the end of the spike. These can also be seen in figure 4.25, starting at 82.01 ms. For this example, the fit was run until the end, but for the actual measurements the fit was stopped at the first current minimum. Third, the IGBTs have a minimum turn-on time, as well as a turn-off delay time above 2 µs, which also prevents rise times much shorter than 10 µs.
To obtain a value of τ for one particular current spike, the conditional optimizing function *fmincon* is used to find the value pair τ and $P_{\mathrm{cool},1}(g_1)$ which minimizes the root-mean-square error between the calculated conductance and the measured signal $g_{\mathrm{meas}} = i/u$. Given that the voltage and current signal are recorded with decent accuracy and a sample rate of at least 2 orders of magnitude faster than $1/\tau$ is used, fitting is possible for arbitrary current waveforms. Figure 4.25 shows this at the example of one measured current spike. The forward algorithm starts solving the Mayr equation at $t = 82.997\,\mathrm{s}$, i.e. a few microseconds before the current starts to rise. At this time, the arc is assumed to be in steady state, i.e. $P_{\mathrm{cool},0}(g_0) = u \cdot i$. From there on, only the current signal is used as input for the calculation of $g(t)$. The red dashed lines in the conductance and voltage plots are the results for the value of τ which minimizes the root mean square difference between the measured and calculated conductance curves, $\tau = 8.2\,\mu\mathrm{s}$ in that case. Additionally, two dotted lines show the curves that result for higher ($\tau = 5.2\,\mu\mathrm{s}$) or lower ($\tau = 11.2\,\mu\mathrm{s}$) values than the optimal fit.

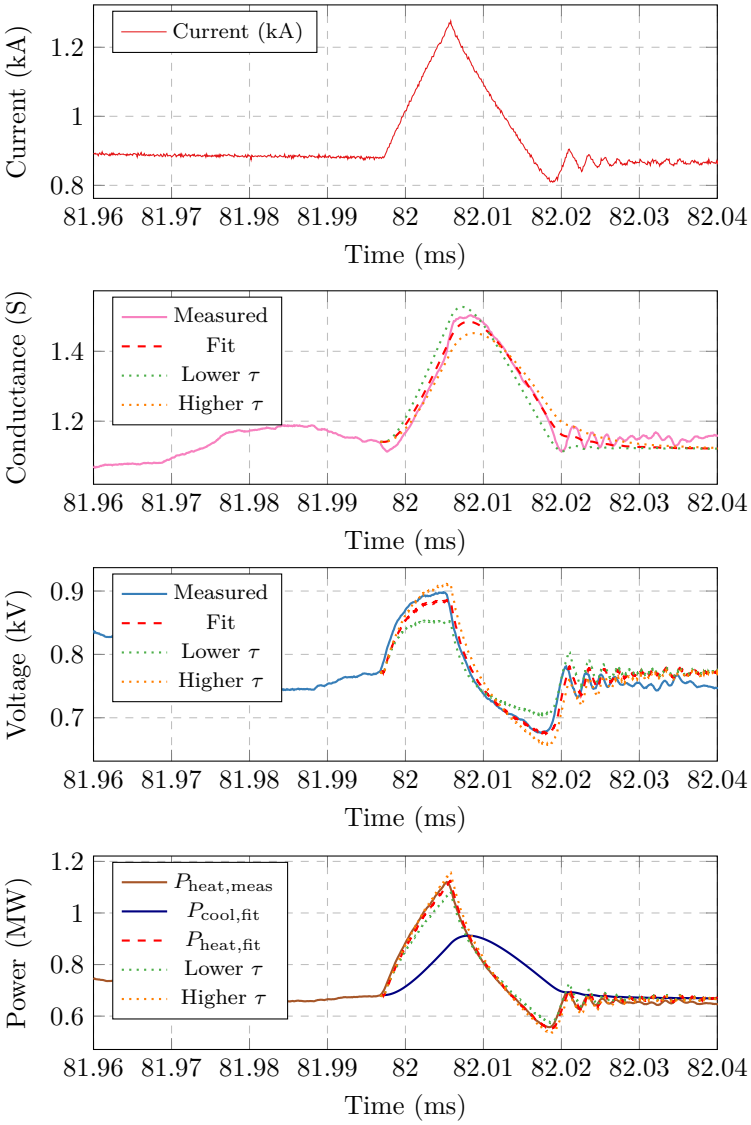

Figure 4.25: Example of the Euler-based fitting algorithm. The current spike from figure 4.5 was taken as input. The measured values for arc voltage, conductance and ohmic heating power are shown, as well as the corresponding values of the fit. The result in this case is $\tau = 8.2\,\mu s$. Additionally, the dotted lines indicate the curves which result for $\tau = 5.2\,\mu s$ (green) and $\tau = 11.2\,\mu s$ (orange)

4.4. Determining Axial Voltage Distribution

This section is largely based on [BF18].

The surroundings in which the arc burns inside a gas blast interrupter vary greatly with axial position. In the presented setup, the pressure and gas density drop by a factor of two from inlet to nozzle throat, while the velocity increases from below Mach 0.2 to Mach 1. In the diverging section, pressure drops even more rapidly, from 4 bar abs. to below 1 bar abs. at the exit. These changes likely have a strong influence on the arc voltage in the different axial segments. In order to understand which axial segment of the arc in a converging-diverging nozzle contributes how much to its $u(i)$ curve, it is necessary to determine the voltage drop of individual arc segments. The model interrupter has adjustable electrodes, which enables measurements with varying arc lengths and at different positions inside the nozzle. Unfortunately, it proved to be difficult to measure configurations where the downstream electrode is upstream of the throat (i.e. $\beta < \gamma$ in the nomenclature introduced in figure 4.9). The arc root does not stay on the tip of the contact, but moves downstream along the electrode, elongating the arc by several centimetres, an example is shown in figure 4.20.

This made it impossible to determine the arc voltage as a function of axial position by direct measurement. An example measurement illustrating this is shown in figure 5.2. Here, two setups with the same upstream contact position $\alpha = 75$, but different downstream positions $\beta = 95$ and $\beta = 135$ are compared. Those setups have 20 mm and 60 mm arc length, but show almost identical arc voltages (solid and dashed lines). To overcome this problem, the positions of upstream and downstream contacts were varied independently in steps of 20 mm, while always keeping $\beta > \gamma$. In this section, a differential method is explained, that still allows the determination of the voltage drop of the upstream arc segments.

In a first step, the static voltage current curve is determined, as described in section 4.3.1, for several different contact positions. Two examples are shown in figures 4.28a and 4.28b. The configurations that were measured have varying contact positions in 20 mm steps (see figure 4.27), it is possible to determine the contribution to the arc voltage by the individual 20 mm long axial segments. This is done

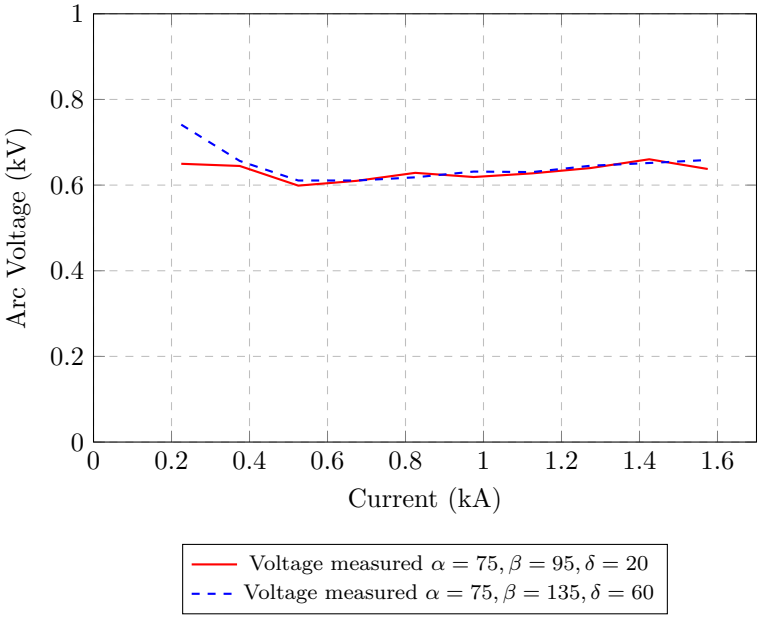

Figure 4.26: The lines indicate the measured arc voltage of two configurations with identical upstream contact position ($\alpha = 75$), and varying downstream position ($\beta = 95$ and 135 respectively). The results are almost identical, despite the difference in contact gap. This is believed to be caused by arc root movement along the downstream contact pin, as illustrated in figure 4.20. The differential method gives more plausible results, as shown in figure 5.2.

by subtraction of the results for configurations without the segment in question from the results that had an arc in that segment. To determine the median voltage drop from position 75 mm to position 95 mm, the median voltages of the tests with $\alpha = 95,\ \beta = 155$ are subtracted from the median voltages of the tests with $\alpha = 75,\ \beta = 155$, current bin by current bin (see section 4.3.1). The result is considered to be the voltage drop of that segment. This method assumes that the different arc segments are independent from each other, and that the difference in arc voltage between configuration $\alpha = 95,\ \beta = 155$ and $\alpha = 75,\ \beta = 155$ is only originating from the voltage drop in the segment 75 mm to 95 mm. The validity of this

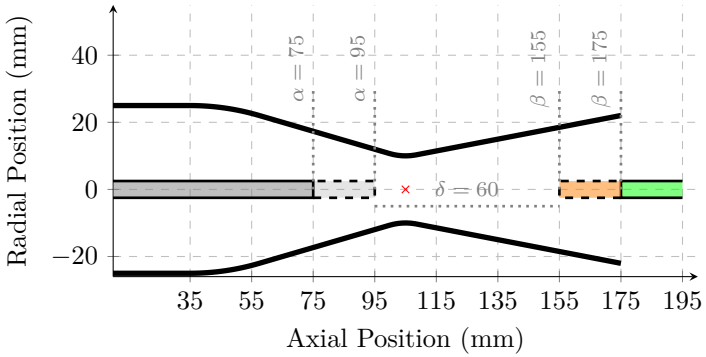

Figure 4.27: Nozzle setup, gas flow is from left to right. α indicates upstream contact position, β the downstream contact position. Both are varied, all combinations are shown later on in figure 5.1. The throat position γ is always fixed, at 105 mm (red cross). The gap between electrodes is denoted by δ. All distances are always denoted in mm, and are measured from the nozzle inlet being the origin, except for δ, which is $\beta - \alpha$. The vertical lines indicate the positions for the examples in figures 4.28a and 4.28b, as well as the verification case in section 5.1.1.

assumption is discussed in section 5.1.1.

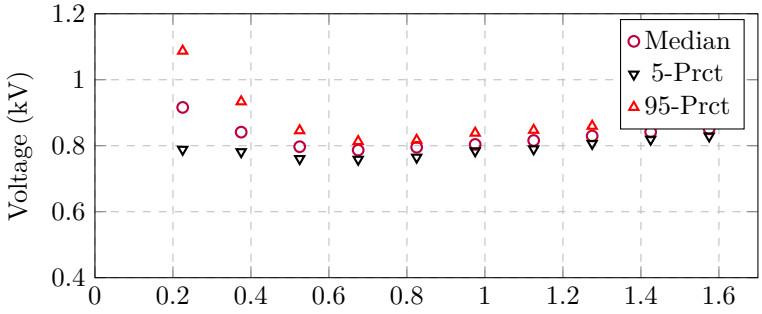

(a) Arc voltage as function of current, for tests with $\alpha = 75, \beta = 155$.

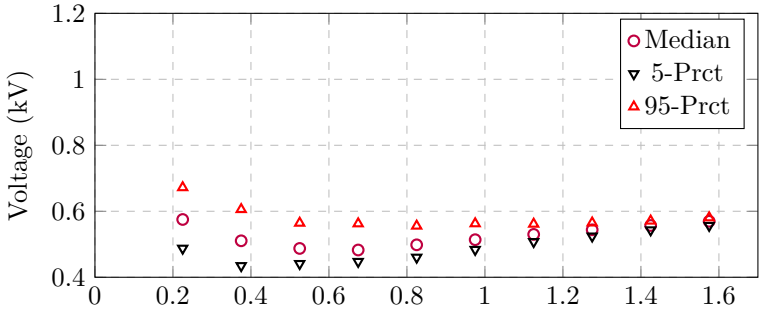

(b) Arc voltage as function of current, for tests with $\alpha = 95, \beta = 155$.

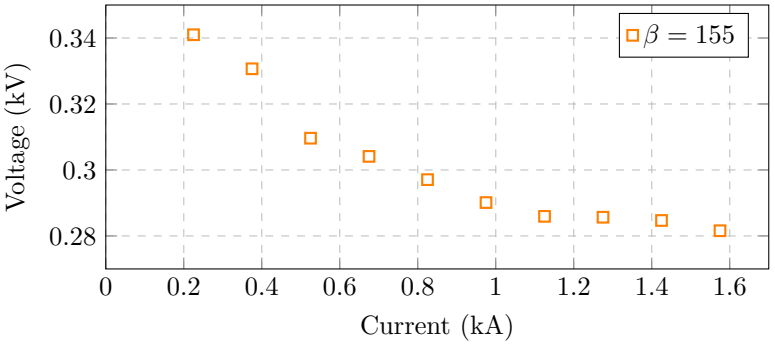

(c) Voltage drop of segment 75 mm to 95 mm

Figure 4.28: The voltage drop for the segment from 75 mm to 95 mm is determined by substracting the median voltage of 4.28b from the median voltage of 4.28a, current bin by current bin.

4.5. Ablation Measurements

This section contains content from [BFF17].

Ablation of nozzle wall material was determined using three different methods, making use of the dividable nozzles described in section 4.2.1. First, the weight of the two halves was measured with a scale (Mettler PN1210), with which the mass could be determined with $\pm 10\,\mathrm{mg}$ accuracy, giving $\pm 20\,\mathrm{mg}$ certainty for the complete nozzle.

Secondly, the two halves were scanned with a commercial flatbed scanner *Canon CanoScan LiDE 220*. Assuming cylindrical symmetry, the change of the contour can be used to calculate the ablated mass, using the density of PMMA ($1.188\,\mathrm{mg\,mm^{-3}}$). Additionally, this method shows the axial location of the ablation. The scanner had a resolution of 4800 dpi, which gives a theoretical resolution of 5 µm per pixel. The gray scale images were aligned, cropped and converted to a binary image first, and the contour of the wall was extracted afterwards using MATLAB. Figure 4.10 shows one example image before processing and the result.

As a third method, the inner contour of the nozzle was determined by a coordinate measurement machine (CMM) *Mitutoyo KN815*, which is usually used to compare workpieces to the specifications. This machine determined the nozzle radius every 5 mm along the axial direction, by measuring 8 points along the circumference. Since the machine was not available at the laboratory, it was only feasible to measure each nozzle before use, and two of the three after the complete series of experiments. The accuracy of these measurements was given by the *roundness* of the circles determined by the 8 measured points, i.e. the difference between the biggest inscribed circle and the smallest circumscribed circle. This roundness value was about 20–40 µm before and 30–100 µm after all the experiments.

To create the test currents, the FPDCS current source as described in [RBF16] and section 4.1 is used. As shown in figure 4.29, each experiment consists of two phases: During the pre-current phase, only a small current is flowing while the downstream contact moves from the closed position to the open position. This way, an arc is established. Towards the end of this phase, the current is slightly increased and the valves of the blowing system are opened. As soon

as the gas flow has reached a steady state and the contact has stopped its movement at the final position, the main current phase is started. During this time, the current is increased and held at its set value for 10 ms. All results that are shown in section 5.2 are calculated only from the values of the main current phase.
After each measurement, the nozzle halves were weighed and the contour was scanned with the flatbed scanner to determine the ablation. Two measurements per current setting were done to ensure repeatability, while keeping the total number of experiments - and therefore cumulative ablation - for each nozzle low. Thus the geometry of the nozzle is as similar as possible for all tests. For the same reason, the measurements were done in ascending order, starting at 300 A up to 1400 A. The measurements with 100 A and 200 A, however, were done afterwards, when it became clear that they are desired to complete the data set. Since the ablation values of 300 A were already at the edge of the measurement range, the 100 A and 200 A tests were done with an adapted current shape. The inductance of the current source was increased, to reduce ripple and prevent the current to go to zero. Additionally the duration of the main current phase was increased from 10 ms to 40 ms, to increase the amount of ablation towards measurable values. During the complete measurement series, the throat diameter increased by a maximum of 10%, which did not change the arc voltage measurably. This was confirmed by repeating the first test ($I = 300\,\mathrm{A}$) at the very end.

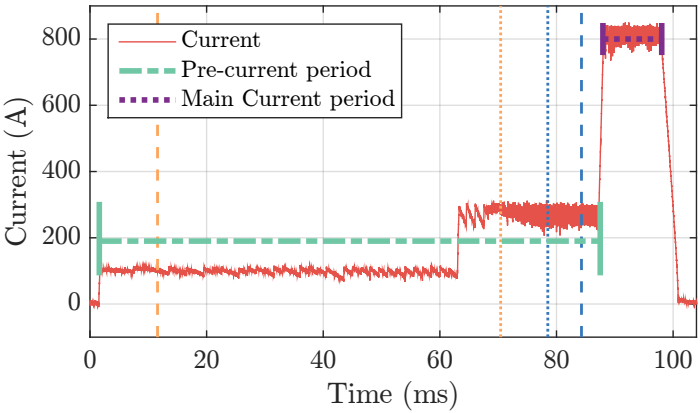

Figure 4.29: Example current waveform. Start and end of contact movement are indicated with vertical dashed lines, start and stabilization of blowing gas flow with vertical dotted lines. The 85 ms of pre-current were identical for all experiments, followed by 10 ms of main current, 800 A in this case.

4.6. 1D Modelling of Arc Cooling

This section contains content from [BF18]

To get a rough estimation on the cooling mechanisms of the arc column and to investigate the influence of nozzle contour and blow gas pressure, a simplified 1D model is used. It was inspired strongly by the work of Lowke, Ludwig and Tuma [LL75, TL75]. Their model assumes an arc in steady state conditions, with cylindrical symmetry, and two radial zones only. In the center there is hot arc plasma, with uniform properties in radial direction. Around that, there is cold gas, also with uniform properties in radial direction. The cold gas flow is not influenced by the arc, so there is no clogging of the throat and no heating of the cold gas. With these assumptions, analytical formulas for compressible flow can be used to determine all fluid- and thermodynamic variables of the cold gas zone as function of axial position. The key assumption of Lowke's model is the absence of a radial pressure gradient. If this holds, the cold flow determines the axial Mach number distribution of the hot plasma zone as well. With Mach number and pressure fixed by the cold flow at every nozzle

position, it is possible to solve for arc temperature and radius. The problem is divided into short axial segments (0.1 mm long) and the energy balance is solved at each axial position along the arc axis. The required steps are explained briefly in the following.

First, the model uses the isentropic flow relations to determine the properties of the cold flow along the nozzle. The details can be found for example in [KC10], or any other textbook on fluid dynamics that covers sub- trans- and supersonic flow of compressible fluids. For the present work the detailed calculations are not needed. It is enough to know that analytical solutions exist, allowing the calculation of any relevant parameter of a fluid that flows through a nozzle, if certain assumptions and boundary conditions are met. If the flow is steady (i.e. velocity distribution does not change with time), frictionless and adiabatic (i.e. the gas is neither heated nor cooled), and the fluid is an ideal gas, the flow only depends on four parameters: nozzle shape, inlet pressure and exit pressure, as well as the adiabatic index of the gas. The latter is also known as the heat capacity ratio, $\gamma = \frac{c_p}{c_v}$, which is dimensionless and equal to 1.4 for air. The inlet temperature is not relevant, as long as the gas fulfills the ideal gas law throughout the complete nozzle. But in order to calculate the temperature distribution, the value at one position is needed, which usually is at the nozzle inlet. Using the so-called *isentropic flow relations*, pressure, temperature, Mach number and density at arbitrary positions in a converging-diverging nozzle can be calculated, only by knowing the stationary (i.e. inlet) values, and the ratio of local nozzle cross section and throat area.

If the cold gas flow is known, the plasma is modelled in a second step. This requires more detailed material data, which for air is given by D'Angola [DCGC07, DCGC11]. This data set is valid up to 60 000 K and 100 bar, and includes all values needed: specific enthalpy h (equation 55 with coefficients from table 22), electrical conductivity σ (equation 58 with coefficients from table 25) and density of air ρ (equations (53) and (54) with coefficients from table 21) as function of pressure and temperature, from which also the speed of sound can be derived. For each arc segment, there are assumed to be three terms, ohmic heating (equation 4.3), radiation cooling (equation 4.4) and convective cooling (equation 4.5) including the axial energy flow

by mass transport (equation 4.6).

$$P_{\text{ohmic}} = i^2 \cdot \frac{l}{\sigma A} \tag{4.3}$$

$$P_{\text{rad}} = \epsilon_{\text{net}} \cdot lA \tag{4.4}$$

$$P_{\text{conv}} = \dot{H}_{\text{out}} - \dot{H}_{\text{in}} \tag{4.5}$$

$$\dot{H}_{\text{out}} = h(p,T) \cdot \dot{m}(p,T,A) = hMc\rho A \tag{4.6}$$

Throughout this manuscript, A denotes the cross sectional area of an axial arc segment of length l, where l is short enough for all variables to be homogeneous in axial direction. For the results shown below, $l = 0.1\,\text{mm}$ was used. The specific enthalpy h, the density ρ, the electric conductivity σ and the speed of sound c are all material parameters which depend only on local temperature T and pressure p. The plasma mass flow out of the segment is $\dot{m}$, and M denotes the local Mach number of the flow, whereas c is the local speed of sound. The convective cooling power of one segment is therefore equal to the enthalpy flow out (downstream) minus the enthalpy flow into the segment (from upstream). This can be either due to a temperature increase in that segment, or an increased mass flow due to radial inflow of cold gas. Both of these effects are combined in equations 4.5 and 4.6.

The radiation losses are modelled to be proportional to the plasma volume, and temperature dependence was implemented using net emission coefficients ϵ_{net} as published by Aubrecht and Bartlova [AB09]. Specifically, the data for 1 mm arc diameter was used. Pressure dependency was accounted for by scaling ϵ_{net} linearly with local density.

As already mentioned, p and M are given by the analytical cold flow calculations, the current i is fixed as well as the enthalpy flow $\dot{H}_{in}$ into the segment from the segment upstream (i.e. $\dot{H}_{\text{in}} = \dot{H}_{\text{out}}$ of the

upstream segment). For a given segment, the only free variables are plasma temperature T and cross sectional area A (i.e. arc radius). If one assumes that there are no other cooling terms except convection and radiation, those two have to be equal to the ohmic heating in steady state:

$$P_{\text{ohmic}} = P_{\text{rad}} + P_{\text{conv}}. \tag{4.7}$$

This energy balance equation reduces the free parameters to one. For each plasma temperature, there is only one possible arc area that fulfills equations (4.3) to (4.7), and vice versa. To get a unique solution for T and A, the combination is chosen which minimises the voltage drop over that segment. This follows the principle of least action and is similar to the arguments in [Chr06]. Temperature is one of the free variables, and therefore density ρ as well as specific enthalpy h in equation (4.6) have to be always recalculated for each change of T while searching the solution.
Since the enthalpy outflow of one segment is the inflow of the next, the global solution can be found by iterating the individual segments from upstream to downstream, while $\dot{H}_{\text{in}}$ of one segment is equal to $\dot{H}_{\text{out}}$ of the segment directly upstream. Figures 4.30, 4.31, 4.32, and 4.33 show results for one set of initial conditions, namely a current of 1000 A, and 7 bar abs. inlet pressure.
Figure 4.30 shows the ohmic heating power, and how it is split between convection and radiation cooling. The radiation term dominates the upstream part of the nozzle, only in the segment right around the throat the convection term gets slightly larger than the radiation term. This is in disagreement with the results from [PBC14], but agrees with the results from [HKRS74] who show a radially resolved energy balance at an axial position close to the throat. Figures 4.31 and 4.32 show the plasma radius and temperature respectively, as calculated by the model. There is little variation in the converging segment, only around the throat there are significant changes. Downstream of the throat position (at 118 mm in the shown example), the convection term in this implementation becomes negative. The temperature jumps to the upper bound of 60 000 K (or 35 000 K in this case, which was set as a upper boundary condition for the simulations shown), and the plasma radius suddenly decreases. This effectively means that the solution found

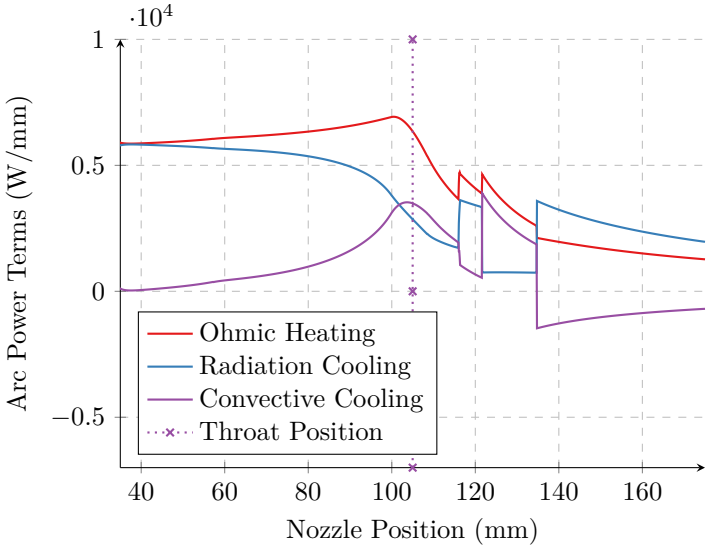

Figure 4.30: Heating and cooling terms according to the 1D model, for 1000 A and 7 bar abs. inlet pressure and the conical nozzle contour (black solid line in 4.15). It is clear that for most of the converging part the radiation losses dominate, only a few mm around the throat (which is at 105 mm) - where acceleration is highest - the convection term briefly contributes a significant fraction to the cooling. In the diverging part, the convection term becomes negative and the model can no longer be applied.

by the algorithm reduces the plasma mass flow for all downstream positions after the jump, and heats the remaining plasma by ejecting the surplus mass back into cold gas at ambient temperature (less mass flow out than in, at the same enthalpy). This clearly violates the second law of thermodynamics, and all data after the first jump is invalid. Therefore the downstream segment was not used in the evaluation. The reason for this behaviour of the model lies in the fact that no additional equation or boundary condition prevents the term P_{conv} in equation (4.5) to be negative, which is not a valid physical processes. For all input conditions that were simulated, this only happened in the diverging segment of the nozzle. Most probably this is due to differences of subsonic and supersonic flow. As long as the term is positive, the results are consistent i.e. at least up to

the throat. This flaw of the model could in principle be corrected by preventing "convective heating" with suitable constraints. But since the results presented in section 5.1 (and [BF18]) showed that the converging segments are the ones which contribute most to the overall arc voltage [BF18], the downstream segments are not of high interest, and this was omitted.
Figure 5.16 shows the electric field as function of axial position, which is in line with the results of [BVF19] presented in section 5.1. The highest field is around the throat, with a gradual increase towards that position in the upstream part. In agreement with [TL75, LL75], this model results in a current-independent arc voltage characteristic. The authors of those papers discuss that the negative differential arc resistance, which is experimentally observed for low currents, results from the effect of turbulence that becomes important when the arc radius reaches the size of the turbulent shear layer at the arc boundary. The effect of turbulence is not modelled here, but by comparing the modelled arc radius with the measured differential arc resistance, the current level at which this effect should become important can still be estimated, as shown in section 5.3.1. A comparison of simulation results with experiments is also found there.

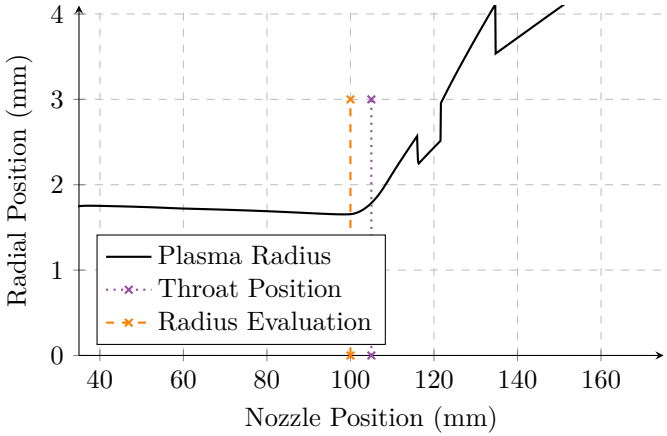

Figure 4.31: Plasma radius for 1000 A and 7 bar abs., as determined by the 1D model. The throat position is indicated by the dotted line, the position for the radius evaluation as dashed line. The jump towards smaller arc radii at 117 mm marks the end of valid data.

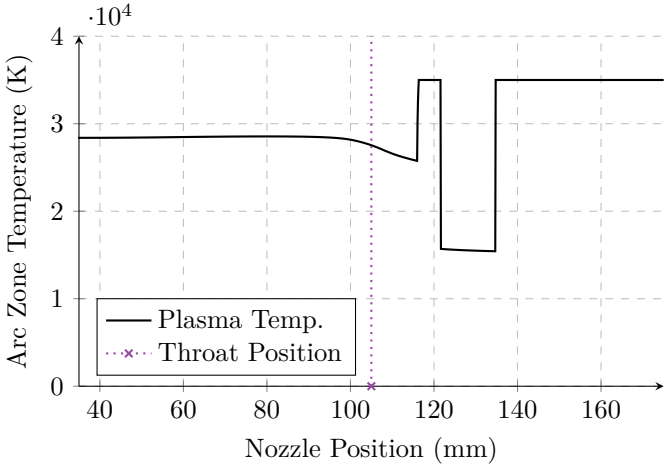

Figure 4.32: Arc zone temperature, as calculated by the 1D model. It can be seen how the temperature drops in the converging section, until the model fails shortly downstream of the throat and runs into the upper boundary at 35 000 K.

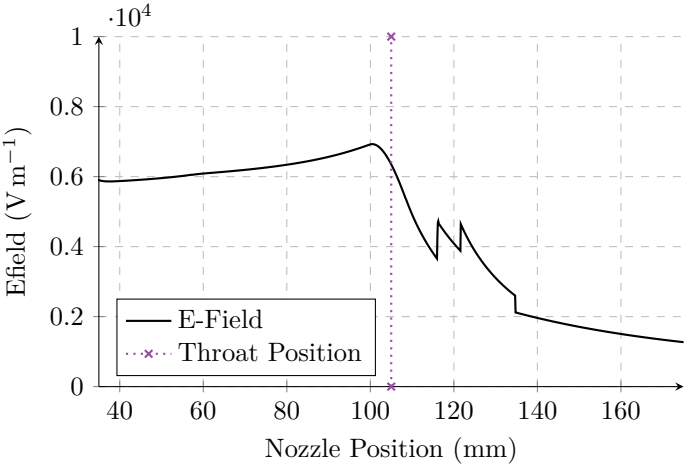

Figure 4.33: Electric field as calculated by the 1D model, for 7 bar abs. inlet pressures and a current of 1000 A. However, just as found by Lowke [LL75], the resulting voltage is independent of current, so this curve results for any input current.

5. Results

With the methods described in chapter 4, it is possible to characterize the behaviour of a given interrupter. Experiments under various conditions were performed, to find the external parameters (nozzle geometry, blow pressure, contact position inside the nozzle etc) which influence the $u(i)$ behaviour favourably. Determining how $\mathrm{d}u/\mathrm{d}i$ can be changed towards more negative values for high current values is of special interest. Empirical studies with varied external parameters are accompanied by theoretical studies of the interaction of axial gas flow with the plasma column inside the interrupter in an attempt to find the fundamental underlying physical processes that determine $u(i)$.
To keep the results close to their discussion for easier reading, each section first describes the results of one parameter variation, followed directly by their discussion.

5.1. Axial Distribution of E-field

This section is largely based on [BF18]
The gas in typical gas blast interrupter nozzles is accelerated from almost stationary to supersonic speeds. This implies gas properties like pressure or density vary greatly (more than one order of magnitude) in axial direction, which in turn have influence on the cooling of the plasma. It is very likely that different axial segments have a different voltage current curve $u(i)$, with different differential resistance. It is non-trivial to measure the axial E-field distribution of an arc, as shown for example by [Hof12]. A method based on variable contact positions was developed during the present work, which is described in section 4.4. The result of this method are presented here.
Fifteen different contact configurations were measured, as shown in figure 5.1. The positions refer to the coordinate system introduced

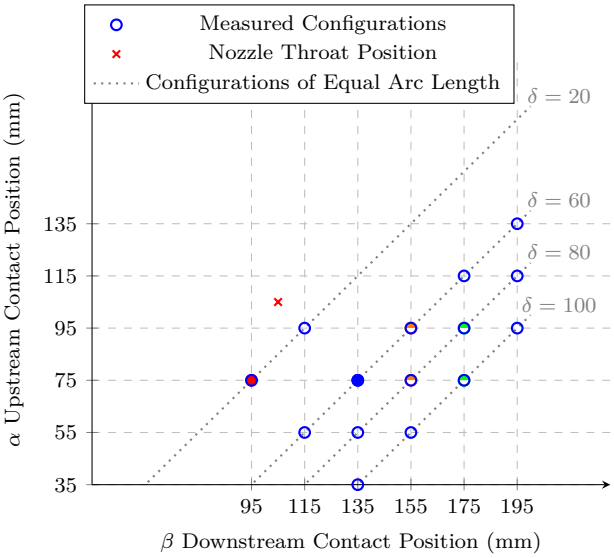

Figure 5.1: All combinations of upstream (α) and downstream contact positions (β). The dotted lines indicate configurations with equal arc length δ. The red and blue filled circles indicate the measurements shown in figure 5.2. The orange and green half filled circles indicate the two possible configuration which were used for the calculation of the segment from 75 mm to 95 mm, as indicated in figure 4.27. Results for this particular segment are shown in figures 5.2 and 5.3c.

in figures 4.9 and 4.27. With this measured set of configurations, it is possible to determine the voltage drop in the segments 35-55, 55-75, 75-95, 95-115, 115-135 by keeping β fix and subtract results of different α. The sections 115-135, 135-155, 155-175, 175-195 can be extracted by keeping α fix and varying β. In total, this gives the arc voltage as function of axial position, between 35 mm and 195 mm (as shown in figure 5.3).

For most of the segments, there are two sets of configurations that can be subtracted as described bin section 4.4. For example the voltage of the segment from 75 mm to 95 mm can be calculated by either using the configurations with $\beta = 155$ or the ones with $\beta = 175$. The results of both possibilities are shown in figure 5.3c. If the assumption of independent arc segments were true, the resulting $u(i)$

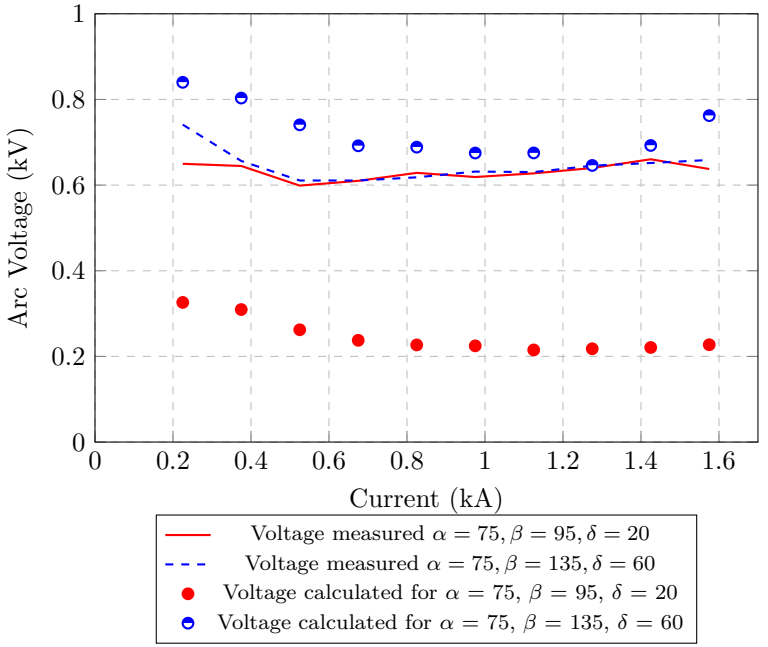

Figure 5.2: The lines indicate the measured arc voltage of two configurations with identical upstream contact position ($\alpha = 75$), and varying downstream position ($\beta = 95$ and 135 respectively). The results are almost identical, despite the difference in contact gap. The filled and half-filled circles indicate the calculated arc voltage for the same configurations, calculated with the method described in section 4.4.

curves of one segment (i.e. 75 mm to 95 mm) should be identical, independent of whether $\beta = 135$ or $\beta = 155$ were used. Whenever more than one possibility to calculate one segment was given, the average of the two was calculated (blue circles in figure 5.3).

The figures 5.3a to 5.3h show the $u(i)$ characteristics of all eight segments. The boxes and diamonds indicate the calculated median voltages for the two possibilities, the filled circles the average of the two. The method is not exact enough to derive precise numerical values, but there are several qualitative trends that can be identified: First, the axial electric field is generally highest at the throat and

in the converging section upstream of it. The segments closest to the inlet, where the gas flow is still slow, and also the segments far downstream of the throat contribute relatively little to the overall arc voltage. Secondly, the negative trend in $u(i)$ is most prominent in the converging segment directly upstream of the throat. As shown in figure 5.3c, $\mathrm{d}u/\mathrm{d}i$ is negative up to about 1000 A. On the other hand, the diverging segment downstream of the throat (figure 5.3f) has an unfavourable positive $\mathrm{d}u/\mathrm{d}i$.
Additionally, the raw measurements (see figures 4.18 and 4.21 for two examples) show that fluctuation of the arc voltage is low for cases where the arc was only downstream of the throat ($\alpha > 105\,\mathrm{mm}$), whereas the measurements with mostly upstream segments show greater spread between median, 5- and 95-percentile respectively. In general, the two identical tests that were combined to obtain the data for one specific contact configuration were very similar. This is as expected, due to experience from earlier tests that checked for repeatability. However, for strongly fluctuating cases, uncertainty is higher than for configurations with stable arcs.

5.1.1. Discussion

Independence of segments

The method described in section 4.4 assumes that the axial arc segments are independent from each other, and if one arc segment is replaced by the electrode, the remaining arc voltage decreases by exactly the contribution of this segment. For the downstream end of the arc, this is a reasonable assumption, since in the diverging part of the nozzle the flow is supersonic. There is no physical mechanism how a downstream segment could influence the arc upstream, at least as long as ablation does not change the mass flow and if there is no significant clogging of the nozzle by the arc cross section. This can be safely assumed, ablation mass flow was determined to be zero below 500 A and still way below the mass flow rate of the gas up to the maximum current 1600 A in [BFF17] and section 5.2. Furthermore, the pressure signals are in agreement with this assumption as well. Significant changes in the available fluid dynamic cross section, either due to wall material contributing additional mass flow, or the arc diameter decreasing the available cross section, would change the flow.

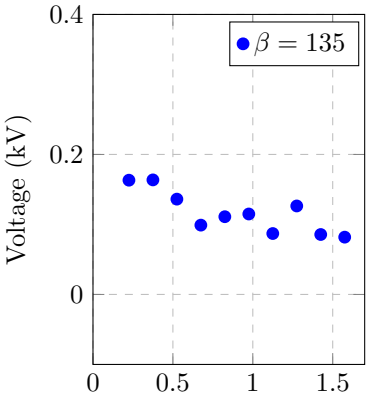

(a) Voltage drop of segment 35 mm to 55 mm

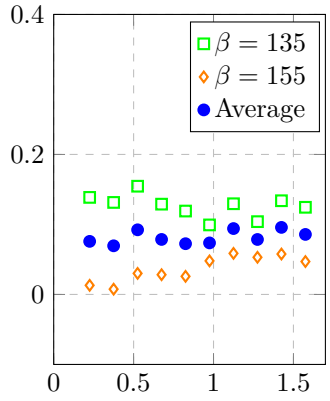

(b) Voltage drop of segment 55 mm to 75 mm

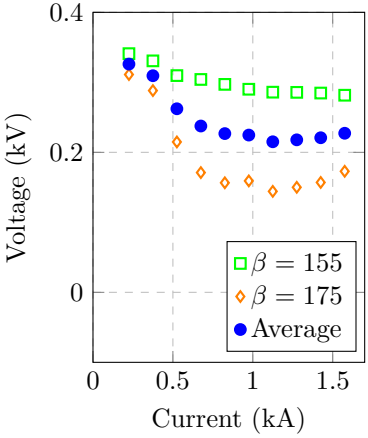

(c) Voltage drop of segment 75 mm to 95 mm

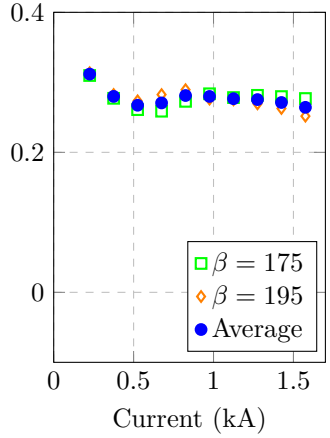

(d) Voltage drop of segment 95 mm to 115 mm

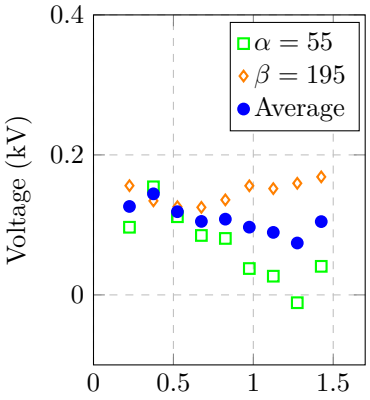

(e) Voltage drop of segment 115 mm to 135 mm

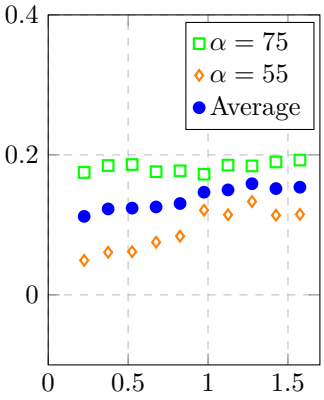

(f) Voltage drop of segment 135 mm to 155 mm

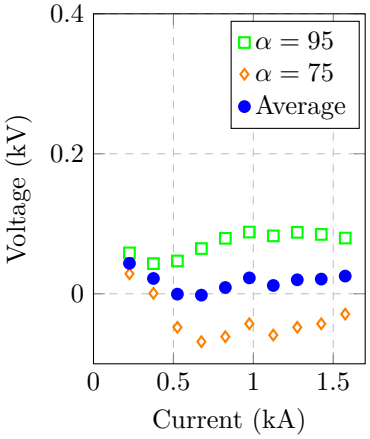

(g) Voltage drop of segment 155 mm to 175 mm

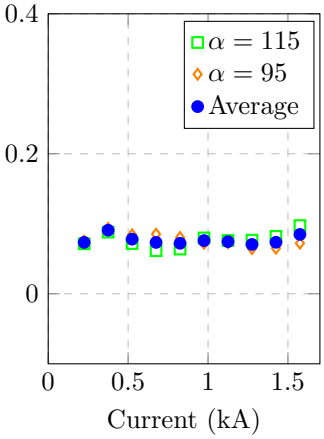

(h) Voltage drop of segment 175 mm to 195 mm

Figure 5.3: Voltage drop of all eight axial segments. Blowing gas was air at 8 bar abs.

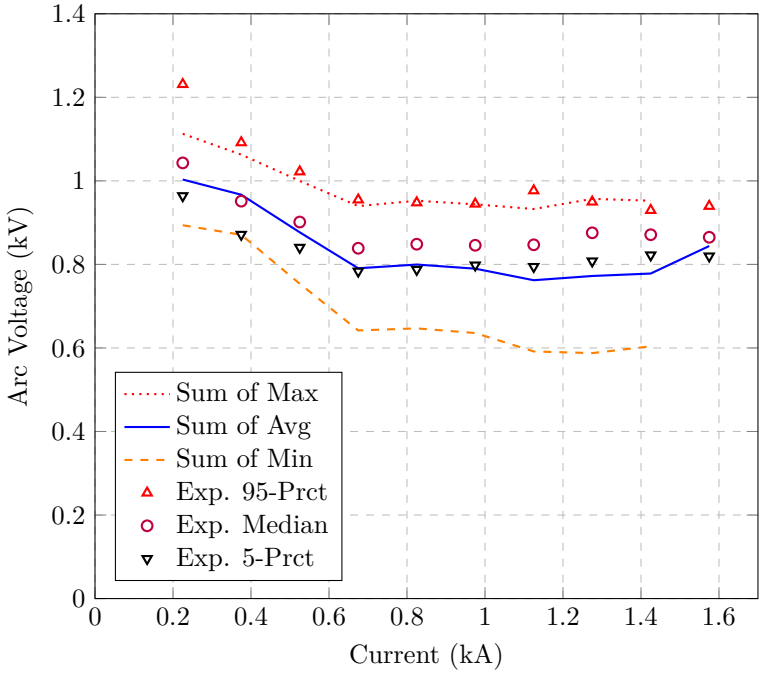

Figure 5.4: Comparison of a direct measurement ($\alpha = 35, \beta = 135$) with the voltage reconstructed by adding up the voltages of the segments, that correspond to the measured geometry. The measured values are indicated by the markers as in figure 4.21, the lines show the sum of the averaged median (solid blue), as well as the sum of the higher (dotted red) and lower (dashed orange) of the two possibilities.

The pressure signal at the nozzle inlet (measured a few centimeters upstream of position zero in figure 4.27) would change if experiments with and without current are compared. This is not the case. For the upstream segments, it is not as easy to motivate the assumption. In contrast, high-speed footage even shows that perturbations to the arc (like excursions away from the center line) are carried downstream with the gas flow. But the upstream segments are exactly the ones which are inaccessible to direct measurements. In order to justify the assumption empirically, the calculated voltages of the segments

are summed up again, and compared with the direct measurements of an arc with the same length. Figure 5.4 shows one example, for the longest and most upstream arc. The median voltages of the five segments from 35 mm to 135 mm were calculated, using all ten relevant different measured configurations, from $\alpha = 35$ $\beta = 135$ up to $\alpha = 135, \beta = 195$. The calculated voltage drops of the five segments were then summed up, and plotted as blue line. The purple circles indicate the median of the direct measurement. The data agrees very well, indicating the assumption is reasonable for the upstream end as well. Furthermore, to give an indication of the robustness of the method, instead of using the average from each segment (blue circles in figure 5.3), the higher and lower values were summed up respectively. This is shown as red, dotted line and orange dashed in figure 5.4. The spread between those gives a good indication of the uncertainty of the method. For all eight segments, the reconstructed median lies within 20% of the directly measured values.

However, the segment 115 mm to 135 mm which was evaluated twice from both sides shows some inconsistency. Once the arc was only upstream of the segment, and once only downstream. In that case, there was considerable difference in the results, as shown in figure 5.3e. This shows the limit of the method, because in case the rest of the arc is upstream of the segment, it shows desired properties due to its negative $\mathrm{d}u/\mathrm{d}i$ (boxes), whereas in case the arc is only downstream, it is not beneficial due to positive $\mathrm{d}u/\mathrm{d}i$ (diamonds).

Additional, the negative values in figures 5.3e and 5.3g also show the limits of the method. The most likely explanation for those unphysical values is non-independence of the segments. Although the opening angle of 10° theoretically should prevent flow separation and the pressure ratio $p_{\mathrm{inlet}}/p_{\mathrm{exit}}$ is large enough to exclude normal shocks inside the nozzle, shocks might still be present towards the end of the diverging part of the nozzle. Additionally, the stationary contact creates a bow shock right upstream of itself, which obviously changes the flow conditions a few mm upstream and moves with the contact as its position is varied.

Consequences for Passive Oscillation

The results show that the most favourable segments are the ones right upstream of the throat, where the overall arc voltage is high, and $\mathrm{d}u/\mathrm{d}i$ is negative for currents up to 1000 A. This is the converging part of the nozzle, where the gas is accelerated from Mach 0.2 to Mach 1.

With the present nozzle and pin contacts, the configuration with most favourable differential resistance would be $\alpha = 75\,\mathrm{mm}$, $\beta = 135\,\mathrm{mm}$. Segments downstream of 135 mm have positive $\mathrm{d}u/\mathrm{d}i$, so including them would counteract the beneficial characteristic of the other segments. This neglects all other aspects, especially the design choices related to the breaking performance at current zero. A distance of 60 mm might be too short to prevent reignition, and a compromise needs to be found. Also, commercial interrupters have pin contacts which are significantly bigger than the 5 mm used here, mostly to withstand erosion at high peak currents. Increasing the downstream pin diameter might change that optimum position, due to changes to the supersonic gas flow and bow shock locations. If the pin diameter is not negligible compared to the nozzle cross section, the downstream position can have a significant influence on the flow. The most extreme case is a pin that creates a second, even smaller bottleneck after the nozzle throat, which would change the flow conditions completely. Introducing a hollow upstream contact for double flow arrangement might also alter the results obtained here. Other effects, like wall ablation or contact electrode erosion might also change the behavior, especially if they introduce significant amounts of gas or metal vapor into the arcing plasma.

Including the segments upstream of 75 mm would only add a constant voltage independent of current, but no negative differential resistance. Adding a constant offset voltage theoretically should not change the passive oscillation behaviour at all. But the fluctuations around the median also increase, and more fluctuations are probably bad for reliable performance. However, without simulations or experiments that include an LC-path in parallel to a gas CB, it is hard to judge how much influence the fluctuations have on breaking performance.

For application in real-sized devices, $\mathrm{d}u/\mathrm{d}i$ is required to be negative at realistic load currents, which are about 5 times higher than

the currents available with the flexible pulsed current source. As discussed in [BFF17], the onset of ablation correlates with $\mathrm{d}u/\mathrm{d}i$ becoming zero or positive. In the following it is thus investigated if ablation is the physical reason for the change in $\mathrm{d}u/\mathrm{d}i$ or if this onset happens coincidentally at the same current amplitude.

5.2. Nozzle Wall Ablation

This section is largely based on [BFF17], and the relevant part of [BVF19].

For the measurements presented in [BFF17], three identical PMMA nozzles were produced, as described in section 4.2.1. Each was used for a series of experiments at one pressure. In the following, these series are shown as 4.5 bar abs., 8.4 bar abs. and 12.7 bar abs., which refers to the inlet pressure of the nozzle. Additionally, one nozzle from the ablation resistant material was used as well.

Figure 5.5 shows that the $\mathrm{d}u/\mathrm{d}i$ behavior is more favorable for higher blow pressures. For 4.5 bar, the voltage curve is decreasing up to about 400 A, and is slightly rising until it becomes flat above. For 8.4 bar the rising part is less pronounced and for 12.7 bar the rising part is not observed anymore. The curve gradually transitions into a flat regime around 800 A to 1000 A. Additionally, the overall arc voltage and arc power is higher for higher blow pressures, as shown in figure 5.6.

Table 5.1 shows the mass that was ablated during the entire measurement series, for all three pressures. The CMM measurements agree very well with the weight measurement whereas the flatbed scanner

	Scale	**Scan**	**CMM**
4.5 bar	5.43 g	5.56 g	n/a
8.4 bar	4.05 g	4.41 g	4.14 g
12.7 bar	3.38 g	3.72 g	3.35 g

Table 5.1.: Sum of the ablated mass of all (16) experiments for each nozzle, determined by weighing, the scans and the CMM. Scale inaccuracy is at least ±20 mg.

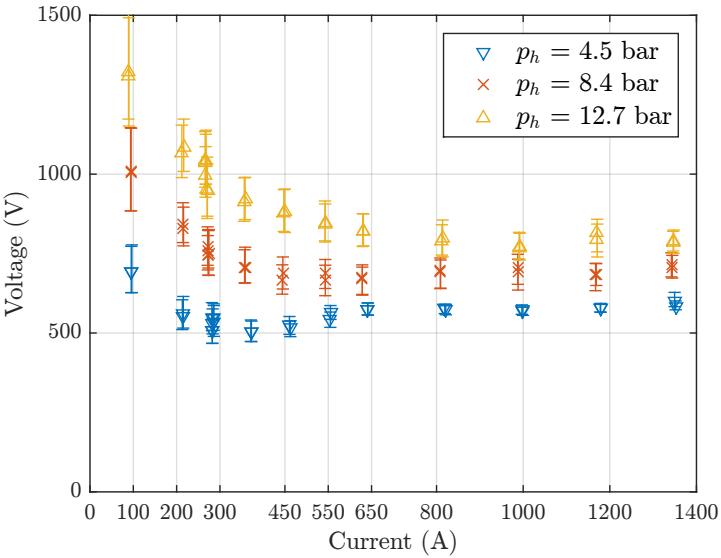

Figure 5.5: Arc voltage as function of current. The markers show the median, the errorbars indicate the standard deviation.

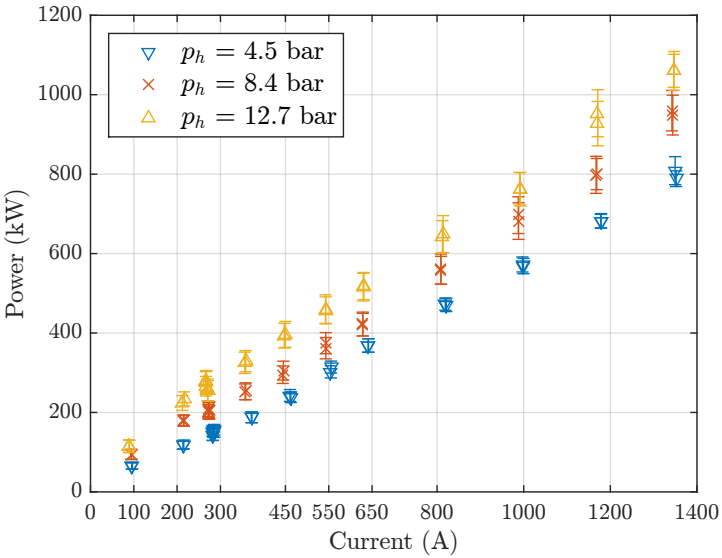

Figure 5.6: Arc power ($p = u \cdot i$) during the main current phase as function of current. Errorbars indicate the standard deviation.

results overestimate the mass loss by about 10%. Figure 5.7 shows the nozzle geometry change of the 12.4 bar series, as determined by the 29 measured circles of the CMM, and the scan.

The results of the scans and the CMM (see figure 5.7) both show the ablation as a function of axial position. Ablation starts at the position of the upstream contact (40 mm), increases towards the throat position (70 mm) and sharply decreases afterwards. In the diverging part of the nozzle, from 80 mm up to the downstream contact at 120 mm the amount of ablation is much smaller than in the upstream section. Furthermore, upstream of the throat (< 70 mm), the scan overestimates the ablation, whereas downstream it shows less in comparison with the CMM. This means the overestimation in the upstream section has to be higher than 10%. The data for the individual currents was only recorded with the scale and the scan, after two experiments for each current value. The evaluation of the results with the method described in section 4.5 indicates that the scanning method has an uncertainty around ± 100 mg. Since the scale had an accuracy of ± 20 mg, the values from weight measurements were used to plot the ablation as function of current in figure 5.8. This clearly shows that the mass loss due to ablation is increasing with current after a certain threshold around 350 A, and higher blow pressure reduced the amount of ablation for all currents.

A more general picture is obtained if the ablated mass is normalized to the total energy the arc dissipated during the high current phase, as shown in figure 5.9. This especially allows a comparison of tests with low current but long duration with tests of high current and short time. Experiments with 300 A for 40 ms are included, which had a similar specific ablation. Figure 5.9 shows even more clearly, that for the lower blow pressures the ablation increases sharply above a threshold current. Qualitatively this is similar to the results of Seeger [STCA06]. Comparing the results quantitatively is not possible though, due to the different materials and gases.

The results above showed correlation between onset of measureable ablation and $\mathrm{d}u/\mathrm{d}i$ becoming zero or positive. To confirm causality, a material with as little ablation as possible was chosen. The company *Brandenburger Isoliertechnik* offers ablation resistant composite material (trade name *S5000*), which was tested. Changing the nozzle material from PMMA to that material did not change

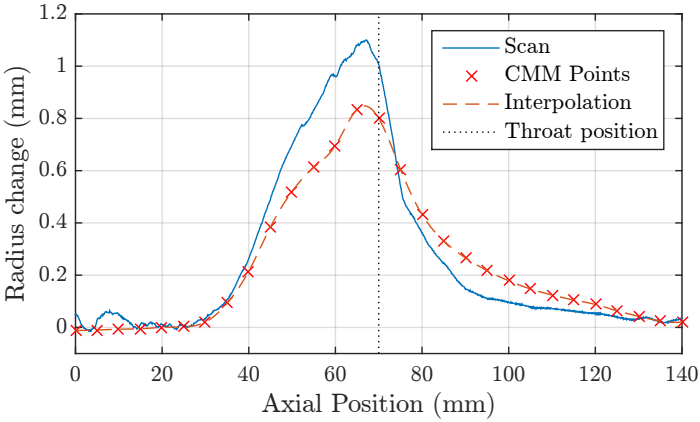

Figure 5.7: Total change of geometry (see figure 4.10) due to ablation. Determined by the flatbed scans and the coordinate measurement machine, after the entire measurement series for the 12.4 bar nozzle.

the $u(i)$ curves significantly. Figure 5.10 shows virtually identical behavior, compared to PMMA for three different inlet pressures and air as blowing gas. Additional ablation measurements using weighing and scanning the nozzle contour showed that *S5000* did loose weight similarly to PMMA, although the nozzle contour did not change as much. Table 5.2 shows the comparision of the PMMA nozzle with the S5000 nozzle.

Measurement	PMMA	S5000
Weighing	0.32 g	0.09 g
Scanning	0.47 g	-0.23 g

Table 5.2.: Difference in ablation between PMMA and S5000 after 3 shots each at an upstream pressure of 7 to 7.5 bar abs. with blowing gas contact opening.

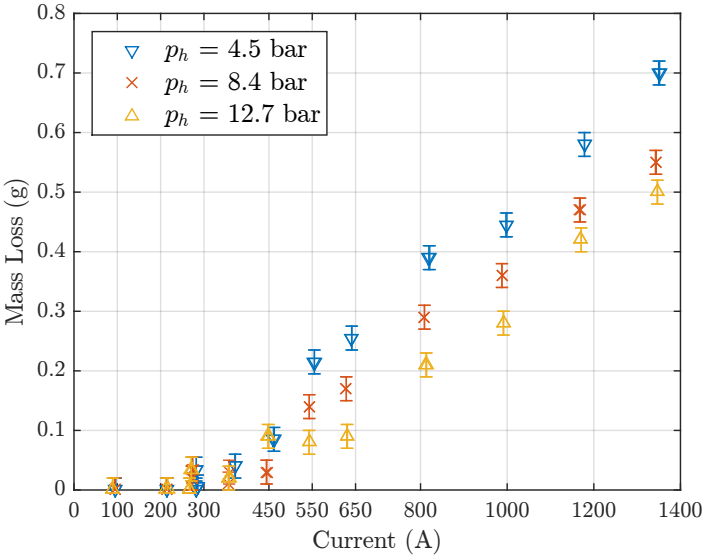

Figure 5.8: Ablated mass as a function of current. Initially all experiments with currents from 300 A to 1400 A used 10 ms of main current. Additional experiments with 300 A and below were performed, using longer periods of main current, but ablation was still too low to be measured accurately. Errorbars indicate scale uncertainty of ±20 mg.

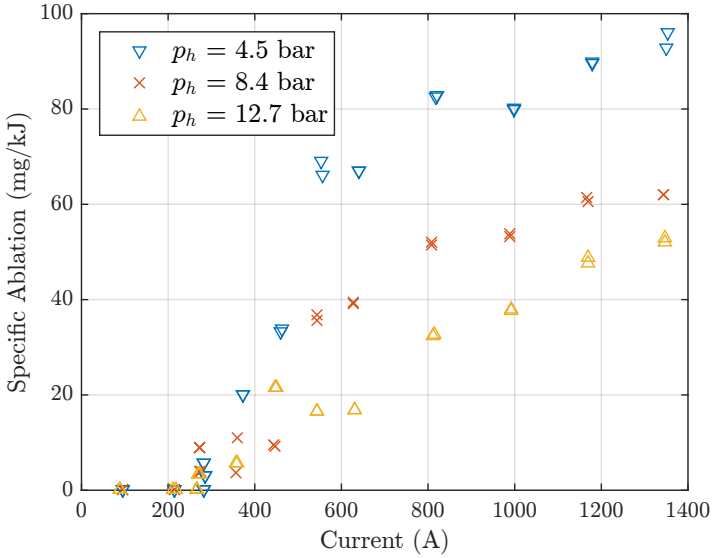

Figure 5.9: Ablated mass normalized to the energy dissipated by the arc during the main current phase, as function of current. Below 350 A, the ablation rate is about as low as the measuring inaccuracy, above that it rises with current.

5.2.1. Discussion

The scanning technique produced valuable ablation mass results, even though the theoretical accuracy was not achieved. It was not possible to detect the edge of the contour on the scans with single-pixel resolution, since the edge is visible as a brightness gradient of roughly 20 px, or 100 µm. To improve the edge detection accuracy, painting the surface with different marker pens was considered, but all inks that were tried did not increase the detection accuracy much. Other materials or changes to the background or lighting might be able to improve this technique. Additional to the edge detection uncertainty, the contour determined by the scan significantly overestimated the change of the radius around the throat compared with the CMM, as shown in figure 5.7. This is attributed to the fact that the gap where the two nozzle halves are joined is not perfectly gas-tight. The tests with 800 A and above showed erosion on the mating surface, up to the sealing cord groove, which was likely caused by hot gas entering the gap. This erosion most probably eroded the contour edge as well, which means the assumption of cylindrical symmetry does not hold perfectly.

As shown in figure 5.7, ablation is generally higher upstream. One possible reason for this bias could be higher arc power in the upstream segments compared to the downstream segments. This is in line with the results shown in section 5.1, which showed considerably higher voltage drop in the upstream segments. Alternatively, the percentage of the dissipated arc energy that contributes to ablation compared with other cooling mechanisms is higher upstream. Higher blow pressures leads to higher arc power and lower ablation rate at the same time. This means, with increasing blow pressure the overall share of the ablation as cooling mechanism is reduced. However the present data does not allow for a quantification or explanation of this effect, since too many factors are still unknown. One of them is the combustion of PMMA with the oxygen of blowing air. According to [RQ96], combustion of 1 g of PMMA yields a similar energy than what is required to vaporize it. This means, it is not possible to determine the energy balance of the ablation properly as long as air is used.

The additional measurements with *S5000* and PMMA nozzles which

were performed after the publication of [BFF17] clearly show that ablation rates up to 1600 A are not high enough to influence the gas flow or the arc voltage significantly. This can also be justified by pressure measurements (not shown), that indicate that the upstream pressure does not change much with changing current. If the mass flow of ablated wall material would be significant compared to the mass flow of the blowing gas, this would lead to drastically rising pressures upstream as well as at the nozzle throat, where sensors are installed. This is not the case. Visual inspection of the *S5000* nozzles indicated charring of the material. Mass loss is most probably due to evaporation of volatile parts of the material, while simultaneously the charred material kept its shape. In general, it proved more difficult to determine ablation rates for *S5000* than for PMMA. The weight of *S5000* nozzles did change overnight, probably due to moisture ingress and drying processes, and the ablated surface was cracked and eroded by pieces breaking off, rather than homogeneous ablation. See figure 5.11 for an illustration of this effect. This made the determination of ablation rates by measuring changes in geometry more challenging than it already is for PMMA.
Although the results are not as obvious as expected, it can still be concluded that ablation is not the main driver for the differential resistance to become positive. Mainly because the onset current above which measurable ablation occurs is independent of pressure (see figures 5.8 and 5.9), whereas the transition point where $u(i)$ changes from falling to flat/rising is clearly pressure dependent, as shown later on in section 5.3.

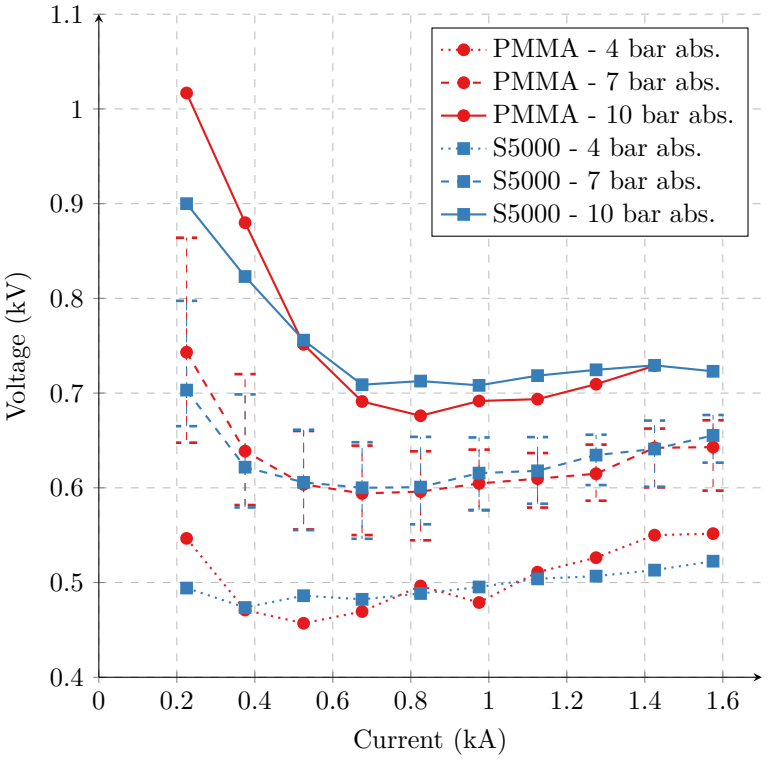

Figure 5.10: Measured arc voltage as function of current for experiments with different nozzle materials and different inlet pressures. Each point indicates the median voltage, calculated from at least 1 ms worth of data, as decribed in [BF16]. For the 7 bar abs. data sets, errorbars were included which show the 5- and 95-percentile of the arc voltage, giving an indication of the maximum fluctuation amplitude. Blowing gas was air.

Figure 5.11: Ablation resistant nozzles after experiments. in contrast to homogeneous ablation in PMMA, the surface of *S5000* material chars and cracks, until pieces break of.

5.3. Influence of Upstream Pressure

This section is largely based on [BVF19].
Previous work showed that the upstream pressure of the blowing gas has a considerable influence on the $u(i)$ behavior [Wal13]. This was confirmed by the experiments, as shown already in figure 5.5 and also figure 5.10. Higher inlet pressures move the $u(i)$ curve up, i.e. increase the overall arc voltage. Additionally, the transition point where $\mathrm{d}u/\mathrm{d}i$ becomes zero or even positive is shifted towards higher currents, as shown in figure 5.13. For air at 4 bar, $\mathrm{d}u/\mathrm{d}i$ is positive above about 450 A, whereas at 10 bar, the voltage decreases with rising current up to 800 A, and starts increasing again above 1000 A. Additionally it shows differential resistance values between $-1\,\Omega$ and $0.2\,\Omega$, with higher pressure yielding more negative values for each current value.

5.3.1. Discussion & Comparison with 1D Model

For the passive oscillation to work, the sum of differential resistance of the arc plus the parasitic resistance of the LC-branch needs to be negative, in order to amplify the oscillating current. Figures 5.12 and 5.13 clearly show increasing the inlet pressure is favourable for passive oscillation switchgear. What matters for this topology of DC switch is the absolute value of $\mathrm{d}u/\mathrm{d}i$ (more negative values are favourable), as well as the maximum current, where $\mathrm{d}u/\mathrm{d}i$ is still negative. Both improve with increasing pressure. Exact numbers for real devices are not known to the author, but parasitic resistance below 100 mΩ seems realistic.
To interpret the experimental results the 1D model was used. Figures 5.14, 5.15, 5.16 show the simulation results for the same pressures as the experiments shown in figure 5.12. The arc radius as function of axial position and for three different pressures is shown in figure 5.15. It shows a reasonable order of magnitude of a few mm. Highspeed footage of the experiments is also available and shows comparable diameters of the light emitting zone. However, no quantitative information can be extracted from the videos without a more sophisticated optical setup. Currently, distortions by the lens effect of the PMMA nozzle and unclear definition of the arc boundary

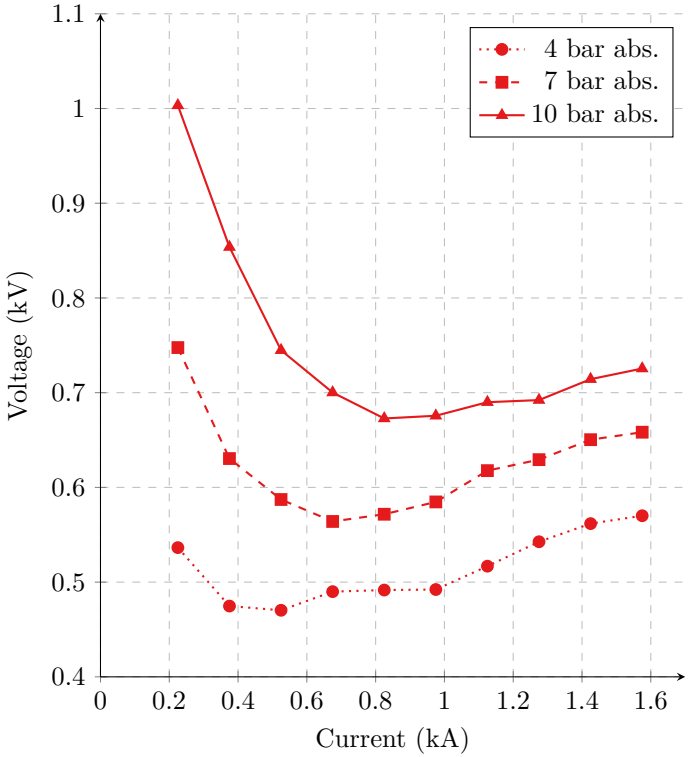

Figure 5.12: Arc voltage as function of current for experiments with different pressures in air

introduce too many uncertain factors. With narrow bandpass filters it would be possible to determine radial temperature profiles like done by [PSC+17] for example. Similar measurements could be used as validation for the model. A simulated arc voltage can be obtained by integration the E-field (figure 5.16). Since the model breaks down in the downstream section, this was done only up to position 100 mm, which is just upstream the throat and shown in figure 5.17b. These values are around 400 A to 600 A, which agrees well with the experimental arc voltage up to the throat position as shown in [BVF19], which were in the same range for the flat part of

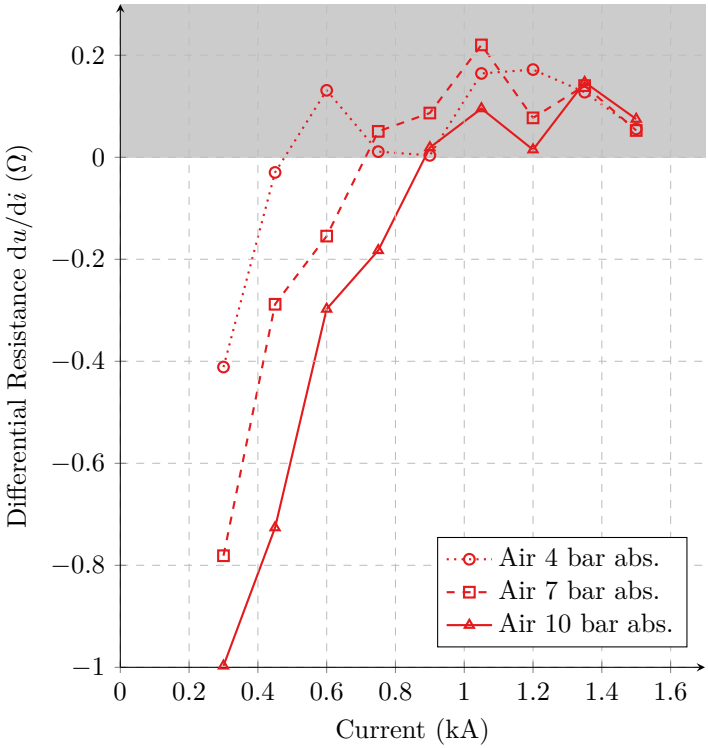

Figure 5.13: Differential Resistance du/di, for different pressures, as function of current. The unfavorable region where du/di is positive is shaded in grey.

the $u(i)$ curve. From the simulation it can be seen that the arc radius squared scales with current, $r^2 \propto i$, which is in agreement with Tuma and Lowke [TL75, LL75]. This is also intuitively clear, the conductive area proportionally increases with current. In addition, it can be derived from the model that at fixed current the arc radius cubed is inverse proportional to the pressure, i.e $r^3 \propto 1/p$, which is different from [TL75, LL75], who found an even stronger dependence to the power of four. Lastly, the electric field scales with the square root of pressure, as shown in figure 5.17b and which is again in agreement with Tuma and Lowke, as well as with the measurements.

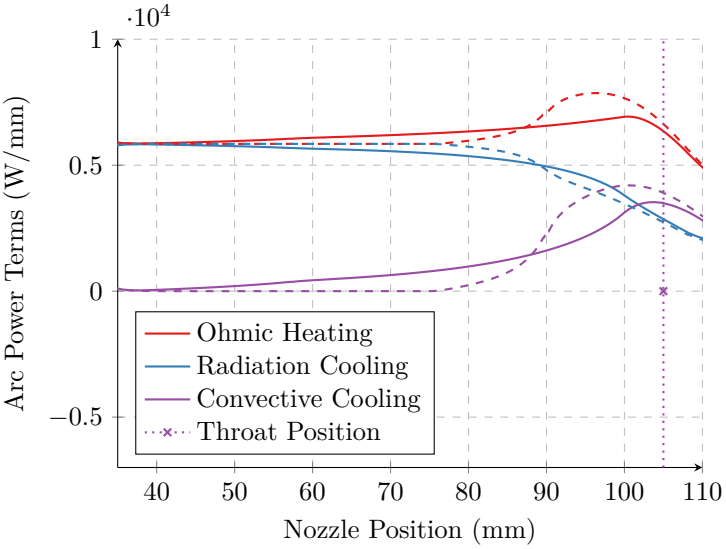

Figure 5.14: Heating and cooling terms according to the 1D model, for 1000 A and 7 bar inlet pressure. Solid lines show the results of the conical nozzle contour (black solid line in figure 4.15), dashed lines were obtained for the shorter acceleration profile (red dashed line in figure 4.15). It is clear that for most of the converging part the radiation losses dominate, only a few mm in front of the throat (105 mm) - where acceleration is highest - the convection term briefly contributes a significant fraction to the cooling. In the diverging part, the convection term becomes negative and the model can no longer be applied.

As mentioned in section 4.6, the simulations results always show the arc voltage to be independent of current, as turbulent mixing

is neglected. As soon as thermal conductance, including turbulence has an effect on central arc temperature, a negative differential arc resistance is expected [LL75]. Figure 5.18 shows the measured values of the differential resistance on the y-axis, plotted against the simulated arc radius for the respective current and pressure values on the x-axis. It is clearly visible that there is a critical arc radius around 1.4 mm, where $\mathrm{d}u/\mathrm{d}i$ goes to zero. The calculated arc radius, at which the transition from negative to non-negative differential arc resistance is observed is found to be independent of pressure. For a given current, the arc radius changes with pressure, which means the critical radius is reached at different current values for different pressures. In fact, for each pressure p there is a current i_{crit} which results in an arc radius of r_{crit}. These current values scale with

$$i_{\mathrm{crit}} \propto p^{\frac{2}{3}}, \tag{5.1}$$

as illustrated in figure 5.17c.
The existence of a critical radius can best be explained by the shear layer that separates the hot arc core from the cold gas flow around it. The author takes this value as an empirical measure for the thickness of the turbulent mixing layer. The model neglects this, but in reality this is definitively present. Lowke already describes this in [TL75], claiming that below 500 A their model did not give the same results as the experiments of Hermann [HKN+74]. For the nozzle shown in figure 4.15, the critical radius below which the arc core is getting too small to dominate the effects of the shear layer is 1.4 mm. The nozzle profile with shorter converging section (red lines in figures) shows a smaller radius in the axial segment with highest acceleration (90 mm to 105 mm in figure 5.15), but slightly bigger values in the straight segments upstream. The voltage drop is highest in the segments with smallest radius. It might therefore be favourable to use a nozzle profile with a short converging section to get more negative $\mathrm{d}u/\mathrm{d}i$. Due to the resulting smaller arc radius, turbulence still influences the central arc temperature more, for otherwise equal conditions. This effect is illustrated in figure 5.17c. If the radius is evaluated not at 100 mm but at the position of its minimum (around 95 mm for the red lines shown in figure 5.15), the critical current is further increased. More detailed simulations and experiments are needed to quantitatively state the improvement due to the nozzle with shorter

acceleration segment.

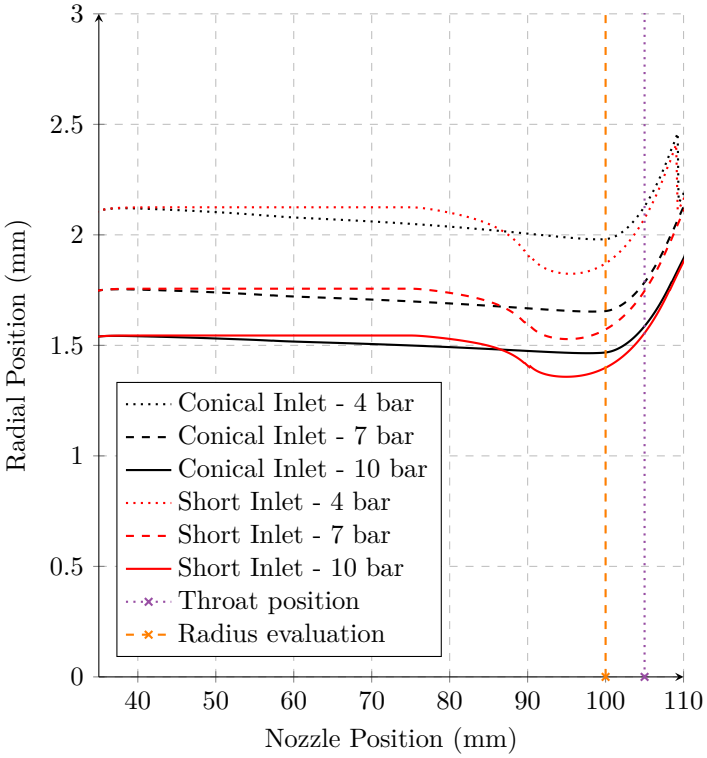

Figure 5.15: Plasma radius for 1000 A and three pressures, as determined by the 1D model. The throat position is indicated by the red dotted line, and the position used for the radius evaluation is indicated in orange. Red lines correspond to the red contour in figure 4.15, black lines to the standard nozzle contour.

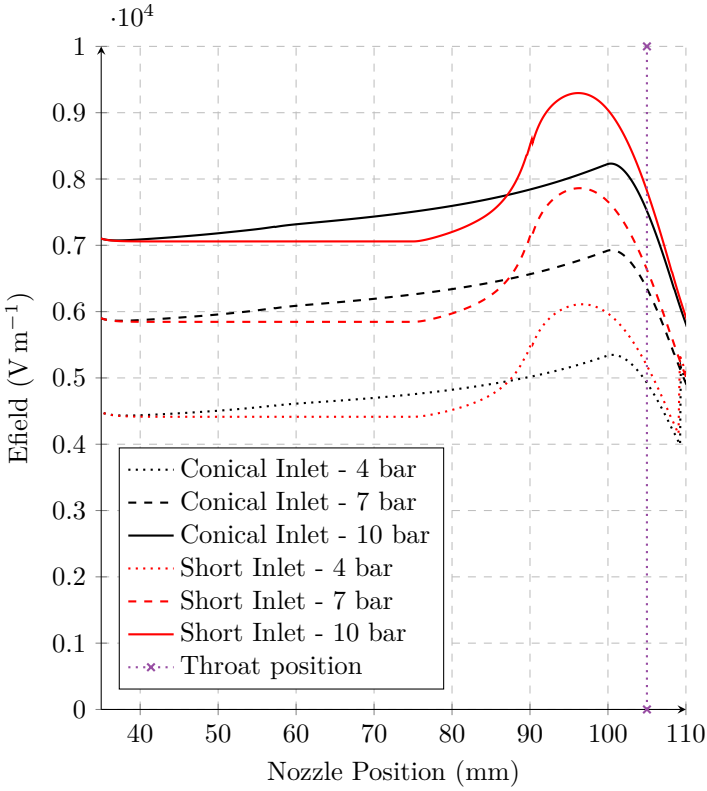

Figure 5.16: Electric field as calculated by the 1D model, for three inlet pressures and a current of 1000 A. However, as explained in section 4.6, the resulting voltage is independent of current, so these curves result for any input current.

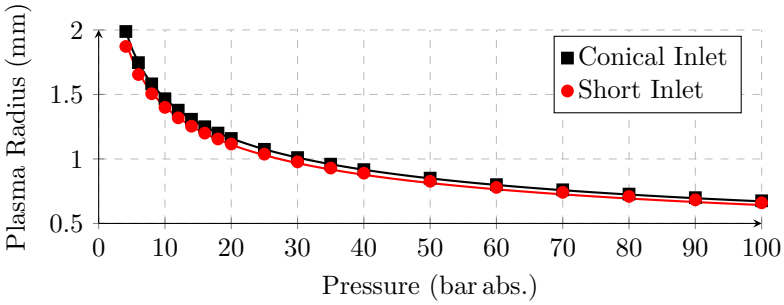

(a) Arc radius at 100 mm as function of pressure. Marks are simulation results, the solid lines show $r \propto 1/p^{-3}$ fits.

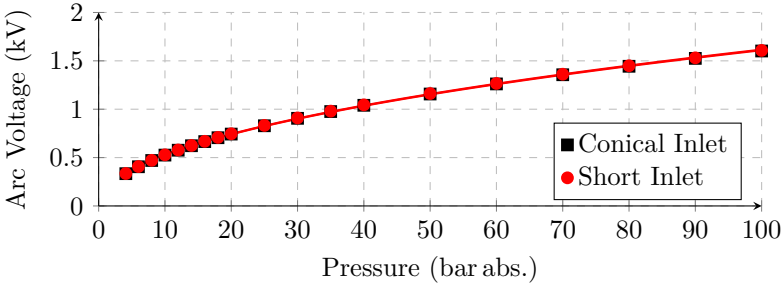

(b) Arc voltage as function of pressure, with the current fixed at 1000 A. Obtained by integrating the E-field from 35 mm to 100 mm. Marks show simulation results, solid lines $u \propto p^{0.5}$ fits of these results.

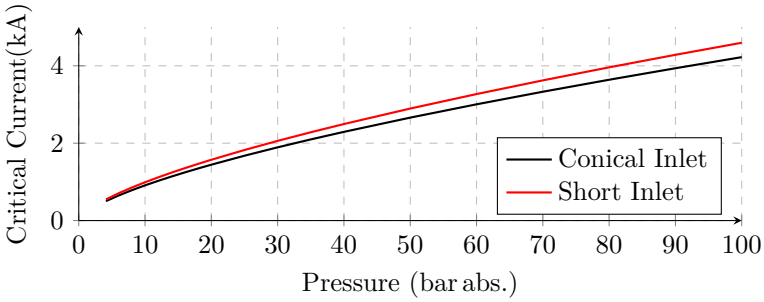

(c) Critical Current, i.e. the current leading to an arc radius of 1.4 mm, as function of pressure. Lines are obtained from $i_{\text{crit}} \propto p^{2/3}$.

Figure 5.17: 1D-model results, for varying pressure and the two nozzles shown in figure 4.15.

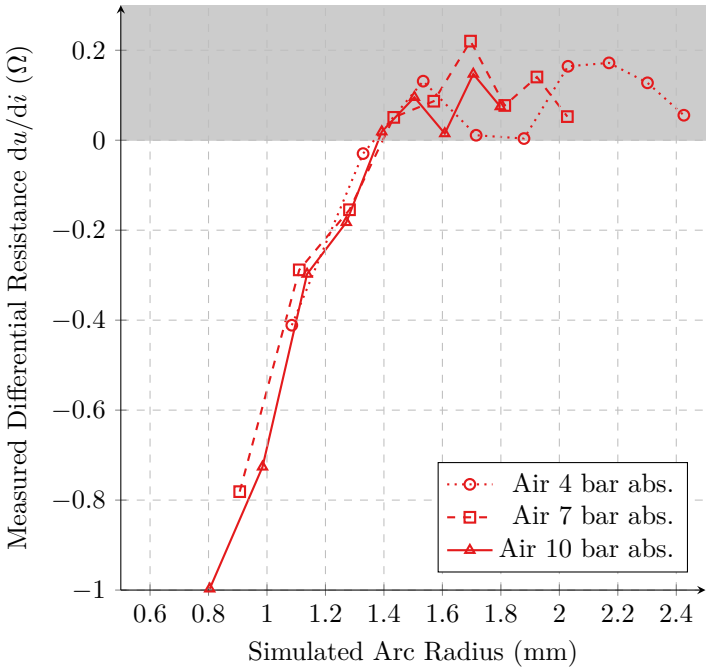

Figure 5.18: For each of the current and pressure combinations measured and plotted in Figures 5.10 and 5.13, the arc radius 5 mm upstream of the throat was calculated using the 1D model. That radius is used on the x-axis, instead of the current as in figure 5.13. The measured du/di values for all pressures line up very well, with negative values corresponding to radii below 1.4 mm, and unfavourable positive values above that critical radius. This indicates that the geometry of the arc column close to the throat is important for the $u(i)$ behavior

5.4. Inlet Conditions

This section is largely based on [BVF19].
In section 5.3, turbulent mixing at arc boundary was assumed to be the major factor leading to negative $\mathrm{d}u/\mathrm{d}i$. This would mean the gas flow conditions play an important role. In an attempt to directly influence the turbulent shear layer (thickness), different parts were inserted in the cylindrical inlet section upstream of the nozzle, as described in section 4.2.1.
Figure 5.19 shows the resulting $u(i)$ curves. Almost all configurations show similar arc voltage. Only flow straightener number 1 showed slightly lower voltage, but with similar shape of the voltage curve.

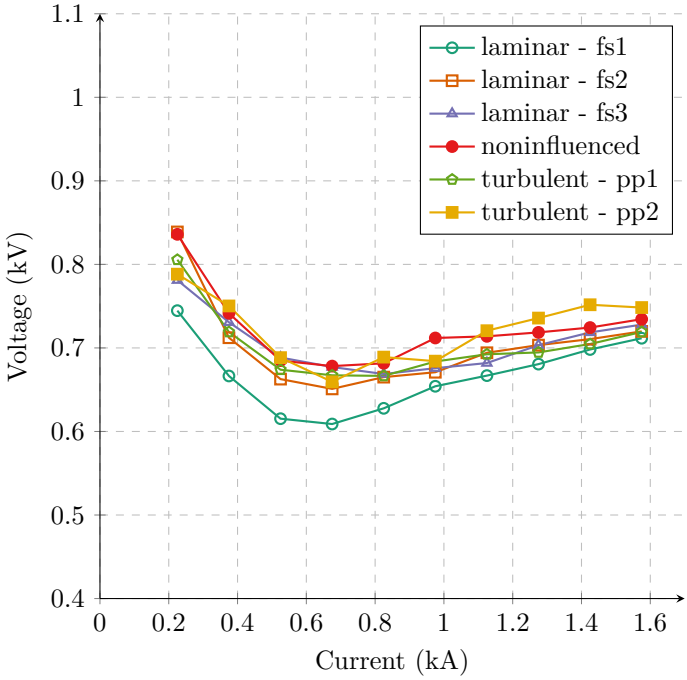

Figure 5.19: Arc voltage as function of current for experiments with different inserts in the gas flow. Inlet pressure 8 bar upstream the nozzle.

5.4.1. Discussion

Although turbulent cooling of the plasma column is considered the main factor for a negative differential arc resistance, no change was observed due to the different inserts in the inlet segment. The inserts probably did not change the conditions at the shear layer between cold gas and hot plasma. The slightly lower voltage of fs1 most likely results from a pressure drop due to friction the long and narrow tubes.

5.5. Blowing gas

This section is largely based on [BVF19].
The experimental results in combination with the numerical model for air, as shown above, indicate that the ratio of arc radius and turbulent shear layer determine at which current levels the differential arc resistance is negative. Thus, it is justified to assume that different blowing gases with different material parameters could also lead to different current levels at which the differential arc resistance changes from being negative to non-negative. This was analyzed experimentally, with three other gases. Nitrogen, carbon dioxide and helium where chosen as their main thermodynamic properties are quite different (see table 5.3 for values at standard conditions). As the setup is not sealed and the exhaust will be released to the environment, the use of other gases is restricted, particularly SF_6 could not be used due to its global warming potential and toxic dissociation products.
Figures 5.20,5.22 and 5.24 show the influence of the blowing gas on the arc voltage. First, it can be noted that helium clearly gives the lowest arc voltage, and the least favourable $\mathrm{d}u/\mathrm{d}i$. For 7 bar, $\mathrm{d}u/\mathrm{d}i$ is positive starting from 500 A, and for 10 bar it is zero form there on. Figures 5.21,5.23 and 5.25 show the differential resistance $\mathrm{d}u/\mathrm{d}i$ for the three pressures as well.

5.5.1. Discussion

The results of the other gases are closer to each other, but differ still. Most surprising was the fact that nitrogen and air are so far

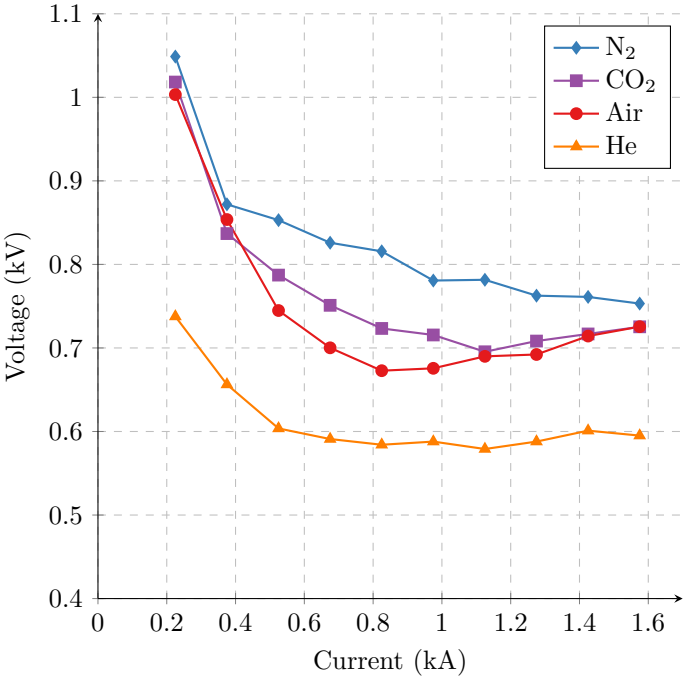

Figure 5.20: Arc voltage as function of current for experiments with different gases at inlet pressure of 10 bar.

apart. Depending on which exact value is still considered negative enough for the application, nitrogen might be the most favorable of the four gases, since its $\mathrm{d}u/\mathrm{d}i$ negative up to 1600 A (as can bee seen in figure 5.20), albeit the derivative is too close to zero to yield a reliable numeric result. CO_2 is in between air and nitrogen, with lower overall voltage than N_2, and $\mathrm{d}u/\mathrm{d}i$ negative up to 1000 A, whereas air has positive $\mathrm{d}u/\mathrm{d}i$ starting at 800 A.

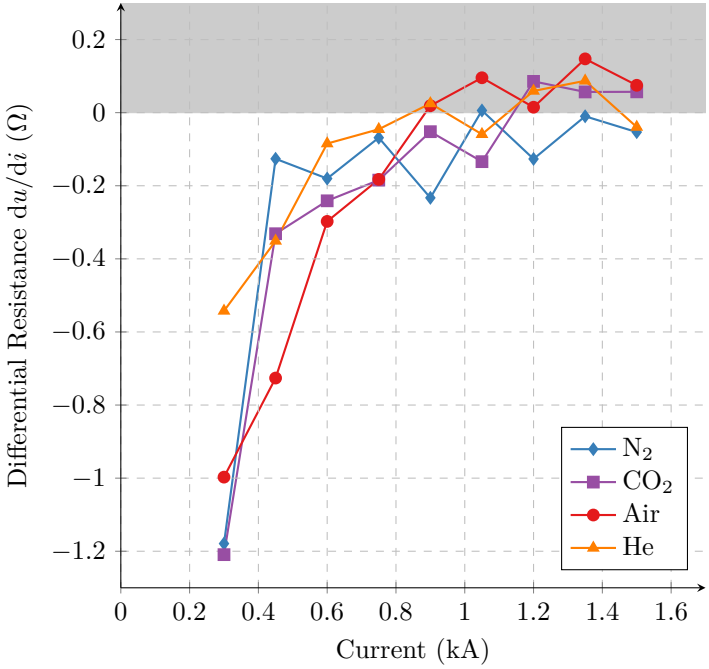

Figure 5.21: Differential resistance du/di as function of current for the different gases. Inlet pressure is 10 bar in all cases. As in figures 5.13 and 5.18, the unfavorable area of positive du/di is shaded grey.

Gas	Speed of Sound v_s [m/s]	Density ρ [kg/m^3]	Thermal Conductivity k [mW/m K]	Specific Heat C [kJ/kgK]
Air	343	1.21	25.9	1.01
CO_2	267	1.84	14.6	0.84
He	1008	0.17	142	5.19
N_2	349	1.17	24	1.04

Table 5.3.: Properties of the different gases at standard conditions. Air, carbon dioxide, helium and nitrogen were used in the experiments. Values taken from [Eng]

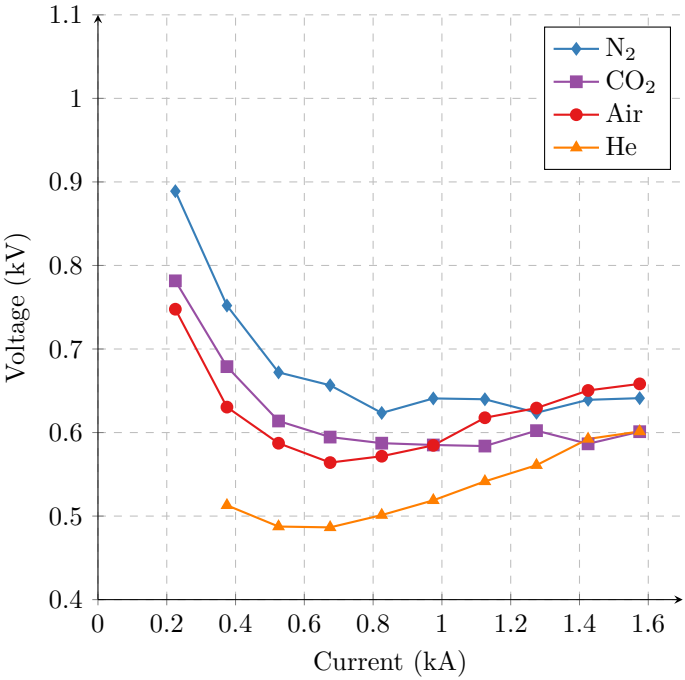

Figure 5.22: Arc voltage as function of current for experiments with different gases at inlet pressure of 7 bar.

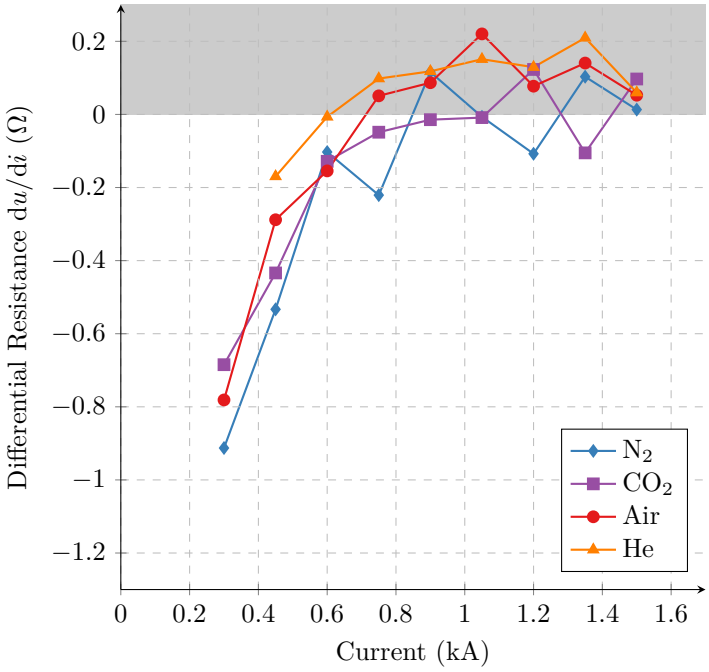

Figure 5.23: Differential resistance du/di as function of current for the different gases. Inlet pressure is 7 bar in all cases. As in figures 5.13 and 5.18, the unfavorable area of positive du/di is shaded grey.

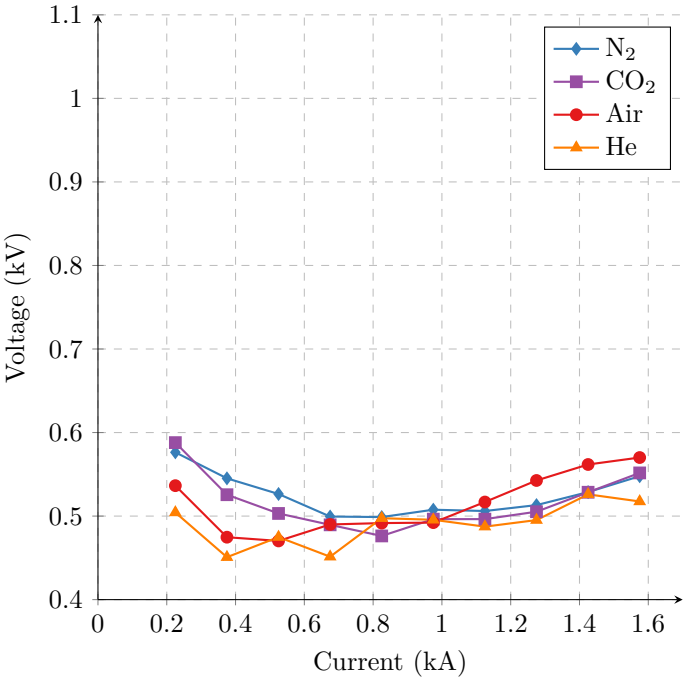

Figure 5.24: Arc voltage as function of current for experiments with different gases at inlet pressure of 4 bar.

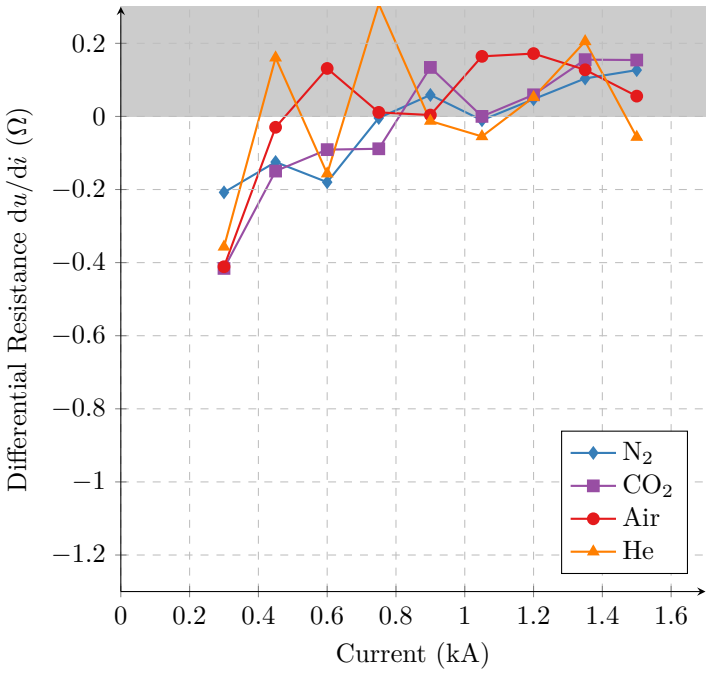

Figure 5.25: Differential resistance du/di as function of current for the different gases. Inlet pressure is 4 bar in all cases. As in figures 5.13 and 5.18, the unfavorable area of positive du/di is shaded grey.

6. Summary & Outlook

In the present work, the fundamental mechanism that leads to current amplification in passive oscillation switches was studied in detail. The importance of the voltage current curve on the time to current zero is derived theoretically, as well as the impact of the arc time constant on the maximum possible oscillation frequency, which have to be accounted for while dimensioning the size of inductor and capacitor in the current commutation path.

Furthermore, methods to characterize the arc of one specific interrupter are presented, using special waveforms created by the Flexible Pulsed Direct Current Source available at ETH. These methods allow the determination of the static $u(i)$ curve as well as dynamic time constant τ with minimal experimental effort.

Using these methods, some qualitative trends were found which should enable optimization of the interrupter, by systematic parameter variations. However, this was done using an academic setup: the current levels were about one order of magnitude too low compared with the real application, and air was used as a blowing gas, rather than SF_6.

Additionally, this work gives some insights in the mechanisms that lead to the negative differential resistance in axially blown arcs. The combination of experiments and an 1D arc model showed the arc radius correlates well with the differential resistance. Below a certain critical radius (1.4 mm in the specific setup used in this work), the differential resistance is clearly negative, above, either zero or even positive. This is in agreement with literature [LL75, TL75], assuming the critical arc radius is roughly identical to the thickness of the arc boundary. For radii below this value, turbulent cooling is influencing the core temperature of the arc. The arc radius is increasing with current, and decreasing with pressure, therefore the critical radius is reached at higher currents, if the upstream pressure is increased.

Nozzle wall ablation is found to start at similar current levels where

the differential resistance becomes zero. However, ablation onset does not scale with pressure, and therefore it can be concluded that moderate ablation (i.e. as long as ablation gas does not dominate the gas flow) is not responsible for the voltage to become independent of current.

The next logical steps in experimental research on passive oscillation would be repeating the academic investigations at realistic currents. For breaking 5 kA to 8 kA, it is necessary to characterize the static and dynamic arc behaviour during peak currents of 10 kA to 16 kA.

Furthermore, comparison with more realistic breaker geometry would be beneficial to confirm the findings. The setup used during this work definitively has advantages due to the fact that the nozzle is easily accessible, but also shortcomings. The open setup prevents any analysis of the influence of the exit pressure for example, which is around six times higher in commercial interrupters. A higher back-pressure requires also higher inlet pressure to keep the ratio $p_{\mathrm{inlet}}/p_{\mathrm{exhaust}}$ well above 3, which is needed to ensure sonic conditions. An encapsulated interrupter with appropriate gas handling equipment would also enable the use of other gases, namely SF_6 or the alternative electronegative gases which are currently discussed.

Experiments which include the LC-branch would also be helpful. First of all, those could validate the simulation results from chapter 3. Secondly, they might give an answer to the question if random fluctuations are beneficial, unfavourable or do not play a role at all. This again requires an upgraded current source, which can deliver the full current for several ms, and is able to deal with a load that provides a high counter voltage. Last but not least, experiments with real oscillations are also needed to evaluate the stress on the interrupter at current zero. In this work, it was always assumed that the interrupter is able to clear as soon as CZ is reached, but this might not be the case, especially if the interrupter design is optimized for negative differential resistance instead of maximum breaking performance. The values of L and C determine the two main variables for succesful interruption: $\mathrm{d}i/\mathrm{d}t$ before, and $\mathrm{d}u/\mathrm{d}t$ right after CZ, and the optimum values for amplification might not be ideal for clearing at CZ. This could be overcome by using more gas interrupters in series than usual, with good amplification but poor interruption performance, or even a series connection different interrupters. For

example gas blast interrupters optimized for amplification could be combined with vacuum interrupters which interrupt at current zero despite very high $\mathrm{d}i/\mathrm{d}t$ and $\mathrm{d}u/\mathrm{d}t$.

Another factor is the time needed to mechanically open the interrupter. Contact separation and pressure built-up due to compression takes roughly 30 ms in most commercial puffer breakers, which is longer than the commutation time. This means, the fault neutralization time is dominated by time the interrupter needs to open. Efforts are made to reduce this time down to one cycle in AC, i.e. around 10 ms, to reduce erosion and enable controlled point-on-wave switching, for example [Tho04, BMS+74]. However, in AC there is no incentive to reduce the opening time to values much below one half cycle, due to the fact that the minimal arcing time is at least that long until natural current zero is reached. For DC breakers fault neutralization times below 5 ms are needed [CTB683]. The author is not aware of any attempts to combine gas blast interrupters with high speed drives take less than 10 ms from trip order to fully open position. This would certainly be interesting, since faster opening times could have very significant influence on the arc voltage, as well as on the interruption performance at current zero. Possible consequences of ultra fast opening include less metal vapour in the plasma due to less contact heating, or transient phenomena in the gas flow pattern. Pressure waves only travel at the speed of sound, which becomes relevant on the single ms timescale, which means flow cannot be treated as quasi-static anymore, but travelling pressure waves in the puffer-nozzle-system need to be considered.

Adding more diagnostics like optical methods which give quantitative results is also a promising option. During this work, a highspeed camera was used which could record the whole nozzle at 100'000 frames per second with reasonable resolution, or up to 2'000'000 fps if only a thin stripe is captured. An attempt to use it to determine the arc radius was made, but proved unreliable due to the fact that the dynamic range of the arc light is much higher than the camera sensitivity. With the help of narrow bandpass filters, it should be possible to obtain radial temperature profiles [PSC+17, SPC+15, FMU+14, CSG+17]. Optical measurements could validate the model results, or detect shortcomings which then can lead to model improvements. The metal content of the plasma was neglected

for example, which could be investigated by filtering copper emission lines.
Regarding simulation work, there are also many possibilities to improve the arc model. The 1D two-zone model is definitively only a first step towards a satisfying arc model, and does not allow numerical interpretation. Namely, it could not reproduce the $u(i)$ behaviour of the arc in the region of interest where R_{diff} is negative. Adding a third zone for the shear layer might be a solution for this issue. Alternatively, there is quite interesting work done to use CFD for arc research, for example [FMN17]. To confirm the hypothesis of the critical radius, a more microscopic view into the plasma might be helpful. This includes modelling the radiation transport from the arc core to the shear layer and beyond, as well as studying the interaction of electrons, ions and neutral atoms in the plasma column.
Another interesting research topic are the concepts where the oscillation is actively amplified instead of purely passively by the arc. This can be done by power electronic devices with voltage ratings well below the system voltage, placed either in the nominal path or in the commutation path. Per Skarby of ABB proposed to use an IGBT with a parallel MOSA to create a high voltage drop (while IGBT is off) or low voltage drop (while IGBT is on) in the main current path. This effectively creates the negative differential resistance by an active component, and described in [Ska11]. A similar concept was presented by [ABN+18], under the name *SciBreak*. There, a vacuum interrupter is used in the nominal path, and a power electronic coverter in series with the usual L and C is used as commutation path. This is more complicated than the simple IGBT-MOSA concept of Skarby, but has the advantage of zero semiconductors in the nominal path, which eliminates the need for cooling and reduces on-state losses.

Bibliography

[AB09] V. Aubrecht and M. Bartlova. Net Emission Coefficients of Radiation in Air and SF6 Thermal Plasmas. *Plasma Chemistry and Plasma Processing*, 29(2):131–147, apr 2009. doi: 10.1007/s11090-008-9163-x.

[ABB13] ABB. Live Tank Circuit Breakers Application Guide, 2013. URL `https://library.e.abb.com/public/26886facea44b7b1c1257cec0046a07c/1HSM954323-02enLiveTankCircuitBreaker-ApplicationGuideEd1.2.pdf`.

[ABN+18] L. Angquist, A. Baudoin, S. Norrga, S. Nee, and T. Modeer. Low-cost ultra-fast DC circuit-breaker: Power electronics integrated with mechanical switchgear. In *2018 IEEE International Conference on Industrial Technology (ICIT)*, volume 116, pages 1708–1713. IEEE, feb 2018. doi: 10.1109/ICIT.2018.8352439.

[Ams77] R. Amsinck. Verfahren zur Ermittlung des Ausschaltverhalten bestimmender Lichtbogenkenngrössen. *ETZ-A*, 98:566, 1977.

[ATW17] T. An, G. Tang, and W. Wang. Research and application on multi-terminal and DC grids based on VSC-HVDC technology in China. *High Voltage*, 2(1):1–10, mar 2017. doi: 10.1049/hve.2017.0010.

[BF16] L. S. J. Bort and C. M. Franck. Effects of nozzle and contact geometry on arc voltage in gas circuit-breakers. In *2016 IEEE International Conference on High Voltage Engineering and Application (ICHVE)*, pages 1–4. IEEE, sep 2016. doi: 10.1109/ICHVE.2016.7800700.

[BF18] L. S. J. Bort and C. M. Franck. Determination of Axial Electric Field Distribution in Blown Arcs With Differential Method. *IEEE Transactions on Plasma Science*, PP:1–7, 2018. doi: 10.1109/TPS.2018.2880950.

[BFF17] L. S. J. Bort, V. Freiermuth, and C. M. Franck. Influence of Ablation on Differential Arc Resistance. *Plasma Physics and Technology*, 4(3):1–4, 2017. doi: 10.14311/ppt.2017.2.145.

[BKS72] W. Bötticher, U. Kogelschatz, and E. Schade. Untersuchung quasistationärer Lichtbögen hoher Leistung bei starker axialer Gasströmung / High Power Quasistationary Arcs in Strong Axial Gasflow. *Zeitschrift für Naturforschung A*, 27(10):1433–1439, jan 1972. doi: 10.1515/zna-1972-1009.

[BMR+85] B. Bachmann, G. Mauthe, E. Ruoss, H. Lips, J. Porter, and J. Vithayathil. Development of a 500kV Airblast HVDC Circuit Breaker. *IEEE Transactions on Power Apparatus and Systems*, PAS-104(9):2460–2466, sep 1985. doi: 10.1109/TPAS.1985.318991.

[BMS+74] R. Berglund, W. Mittelstadt, M. Shelton, P. Barkan, C. Dewey, and K. Skreiner. One-Cycle Fault Interruption at 500 kV: System Benefits and Breaker Design. *IEEE Transactions on Power Apparatus and Systems*, PAS-93(5):1240–1251, sep 1974. doi: 10.1109/TPAS.1974.293847.

[Bon15] M. Bonkarev. *Concept Analysis for High-Voltage Direct-Current Circuit Breakers for Application in a Network of HVDC Transmission*. PhD thesis, Brandenburgische Technische Universität Cottbus - Senftenberg, 2015. URL `https://opus4.kobv.de/opus4-btu/files/3545/Bonkarev{_}Maxim.pdf`.

[BSF19] L. Bort, T. Schultz, and C. Franck. Determining the Time Constant of Arcs at Arbitrary Current Levels. *Plasma Physics and Technology*, 2019, in press.

[Buc14] M. K. Bucher. *Transient Fault Currents in HVDC VSC Networks During Pole-to-Ground Faults*. Phd thesis, ETH Zürich, 2014. doi: 10.3929/ethz-a-010376446.

[BVF19] L. S. J. Bort, M. Vonesch, and C. M. Franck. Controlling the differential resistance of axial blown arcs. *Journal of Physics D: Applied Physics*, in press, jul 2019. doi: 10.1088/1361-6463/ab34e0.

[Cas39] A. Cassie. Arc Rupture and Circuit Severity: a New Theory. In *Conférence Internationale des Grands Réseaux Életriques à Haute Tension*, volume 102, pages 1–16, 1939.

[CBHJ12] M. Callavik, A. Blomberg, J. Häfner, and B. Jacobson. The Hybrid HVDC Breaker. *ABB Grid Systems Technical Paper*, 361:143—-152, 2012. URL `https://new.abb.com/docs/default-source/default-document-library/hybrid-hvdc-breaker--an-innovation-breakthrough-for-reliable-hvdc-gridsnov2012finmc20121210{_}clean.pdf`.

[Chr06] T. Christen. Application of the maximum entropy production principle to electrical systems. *Journal of Physics D: Applied Physics*, 39(20):4497–4503, oct 2006. doi: 10.1088/0022-3727/39/20/030.

[CSG+17] J. Carstensen, P. Stoller, B. Galletti, C. B. Doiron, and A. Sokolov. Measuring Density Profiles of Electrons and Heavy Particles in a Stable Axially Blown Arc. *Physical Review Applied*, 8(2):024002, aug 2017. doi: 10.1103/PhysRevApplied.8.024002.

[CTB683] Cigré JWG A3/B4.34. *Cigre Technical Brochure - Technical Requirements and Specifications of State-of-the-Art HVDC Switching Equipment*. Number 683. CIGRE, 2017.

[CTB739] Cigré JWG B4/B5.59. *Cigre Technical Brochure - Protection and local control of HVDC-grids*. Number 739. 2018.

[DCGC07] A. D'Angola, G. Colonna, C. Gorse, and M. Capitelli. Thermodynamic and transport properties in equilibrium air plasmas in a wide pressure and temperature range. *The European Physical Journal D*, 46(1):129–150, nov 2007. doi: 10.1140/epjd/e2007-00305-4.

[DCGC11] A. D'Angola, G. Colonna, C. Gorse, and M. Capitelli. Thermodynamic properties of high temperature air in local thermodynamic equilibrium: II accurate analytical expression for electron molar fractions. *The European Physical Journal D*, 65(3):453–457, nov 2011. doi: 10.1140/epjd/e2011-20424-5.

[DJSH14] R. Derakhshanfar, T. U. Jonsson, U. Steiger, and M. Habert. B4-304 CIGRE 2014 Hybrid HVDC breaker A solution for future HVDC system Sweden. *Cigre Session Papers & Proceedings*, pages B4–304, 2014.

[DRWZ83] H. Drebenstedt, W. Rother, C. Weber, and P. Zahlmann. Ein verbessertes Verfahren zur Bestimmung der charakteristischen Funktionen des Zweipolmodells für Schaltlichtbögen. *Internat. Wiss. Kolloquium, TH Ilmenau*, 28, 1983.

[Egl16] L. Egli. *Testing of Supersonic Nozzles for High Current DC Circuit Breakers*. Semester thesis, ETH Zürich, 2016.

[Eng] Engineering ToolBox. `https://www.engineeringtoolbox.com`. [Online; accessed March 16, 2018].

[Fai12] P. Fairley. `https://spectrum.ieee.org/tech-history/dawn-of-electronics/san-franciscos-secret-dc-grid`, 2012.

[FCM16] L. T. Falkingham, K. W. Cheng, and W. J. Molan. The design of a 245kV vacuum circuit breaker. In *2016 27th International Symposium on Discharges and Electrical Insulation in Vacuum (ISDEIV)*, volume 2, pages 1–4. IEEE, sep 2016. doi: 10.1109/DEIV.2016.7763961.

[FMN17] R. Fuchs, M. Murmann, and H. Nordborg. Towards an Efficient Arc Simulation Framework. *Plasma Physics and Technology Journal*, 4(1):79–82, 2017. doi: 10.14311/ppt.2017.1.79.

[FMU+14] S. Franke, R. Methling, D. Uhrlandt, R. Bianchetti, R. Gati, and M. Schwinne. Temperature determination in copper-dominated free-burning arcs. *Journal of Physics D: Applied Physics*, 47(1):015202, jan 2014. doi: 10.1088/0022-3727/47/1/015202.

[Fre15] V. Freiermuth. *High Bandwidth Voltage-Divider for HVDC-CB Experiment*. Semester thesis, ETH Zürich, 2015.

[Fre17] V. Freiermuth. *Finding the Limits of Theoretical Arc Models*. Master thesis, ETH Zürich, 2017.

[Goe17] J. Goedejohann. *Development of Highspeed Imaging Evaluation Methods for Arcs*. Semester thesis, ETH Zürich, 2017.

[Hab93] U. Habedank. Application of a new arc model for the evaluation of short-circuit breaking tests. *IEEE Transactions on Power Delivery*, 8(4):1921–1925, 1993. doi: 10.1109/61.248303.

[HHT+18] T. Heinz, D. Helbig, J. Teichmann, S. Wethekam, U. Prucker, M. Konermann, D. M. Engel, and C. Wolf. 145 kV Vacuum Circuit Breaker and Clean Air Instrument Transformer Performance , Installation- and Operational Experience. In *VDE High Voltage Technology 2018; ETG-Symposium*, pages 183–188, Berlin, 2018. VDE. URL `https://ieeexplore.ieee.org/document/8576739`.

[HKN+74] W. Hermann, U. Kogelschatz, L. Niemeyer, K. Ragaller, and E. Schade. Experimental and theoretical study of a stationary high-current arc in a supersonic nozzle flow. *Journal of Physics D: Applied Physics*, 7(12):1703–1722, aug 1974. doi: 10.1088/0022-3727/7/12/317.

[HKN+76] W. Hermann, U. Kogelschatz, L. Niemeyer, K. Ragaller, and E. Schade. Investigation on the physical phenomena around current zero in HV gas blast breakers. *IEEE Transactions on Power Apparatus and Systems*, 95(4):1165–1176, jul 1976. doi: 10.1109/TPAS.1976.32210.

[HKRS74] W. Hermann, U. Kogelschatz, K. Ragaller, and E. Schade. Investigation of a cylindrical, axially blown, high-pressure arc. *Journal of Physics D: Applied Physics*, 7(4):607–619, mar 1974. doi: 10.1088/0022-3727/7/4/315.

[HKRS10] B. Hudoffsky, N. Karrer, and J. Roth-Stielow. Realization of a (400 A / DC-10 MHz) clamping HOKA current probe. In *PCIM Europe 2010: International Exhibition & Conference for Power Electronics Intelligent Motion Power Quality*, pages 556–561, Nürnberg, 2010. VDE Verlag.

[Hof12] M. Hoffacker. *Verfahren zur ortsaufgelösten Messung der Widerstandsverteilung eines axial beblasenen Schaltlichtbogens*. Phd thesis, RWTH Aachen, 2012. doi: ISBN: 3861306824.

[HS70] W. Hermann and E. Schade. Transportfunktionen von Stickstoff bis 26000 K. *Zeitschrift für Physik A Hadrons and nuclei*, 233(4):333–350, aug 1970. doi: 10.1007/BF01397793.

[HS72] W. Hermann and E. Schade. Radiative energy balance in cylindrical nitrogen arcs. *Journal of Quantitative Spectroscopy and Radiative Transfer*, 12(9):1257–1282, sep 1972. doi: 10.1016/0022-4073(72)90183-5.

[HSKY06] M. Homma, M. Sakaki, E. Kaneko, and S. Yanabu. History of vacuum circuit breakers and recent developments in Japan. *IEEE Transactions on Dielectrics and Electrical Insulation*, 13(1):85–92, feb 2006. doi: 10.1109/TDEI.2006.1593405.

[Hum16] J. Humml. *Simulation of Heated Supersonic Gas Flow in a Circuit Breaker Nozzle*. Bachelor thesis, ETH Zürich, 2016.

[Kap11] M. Kapetanović. *High voltage circuit breakers*. ETF - Faculty of Eletrotechnical Engineering, Sarajevo, Sarajevo, 2011. ISBN: 978-9958-629-39-6.

[KC10] P. K. Kundu and I. M. Cohen. *Fluid Mechanics*. Academic Press, 4 edition, 2010. ISBN: 9780123814005.

[KFG+16] A. Khakpour, S. Franke, S. Gortschakow, D. Uhrlandt, R. Methling, and K.-D. Weltmann. An Improved Arc Model Based on the Arc Diameter. *IEEE Transactions on Power Delivery*, 31(3):1335–1341, jun 2016. doi: 10.1109/TPWRD.2015.2473677.

[KS72] U. Kogelschatz and W. R. Schneider. Quantitative Schlieren Techniques Applied to High Current Arc Investigations. *Applied Optics*, 11(8):1822, aug 1972. doi: 10.1364/AO.11.001822.

[Liu16] M. Liu. *Parameter Study of HVDC Circuit Breaker Arcs*. Semester thesis, ETH Zürich, 2016.

[LL75] J. J. Lowke and H. C. Ludwig. A simple model for highcurrent arcs stabilized by forced convection. *Journal of Applied Physics*, 46(8):3352–3360, aug 1975. doi: 10.1063/1.322239.

[LSY+85] A. Lee, P. G. Slade, K. H. Yoon, J. Porter, and J. Vithayathil. The Development of a HVDC SF6 Breaker. *IEEE Transactions on Power Apparatus and Systems*, PAS-104(10):2721–2729, oct 1985. doi: 10.1109/TPAS.1985.319113.

[May43] O. Mayr. Beiträge zur Theorie des statischen und des dynamischen Lichtbogens. *Archiv für Elektrotechnik*, 37(12):588–608, dec 1943. doi: 10.1007/BF02084317.

[Nak91] K. Nakanishi. *Switching Phenomena in High-Voltage Circuit Breakers*. Marcel Dekker Inc., New York, NY, 1 edition, 1991. ISBN: 0-8247-8543-6.

[Nel08] J. H. Nelson. History of Circuit Breaker Standards, 2008. URL `http://www.ewh.ieee.org/soc/pes/switchgear/presentations/tp{_}files/2008-GM{_}Tutorial{_}1{_}Nelson.pdf`.

[Nie79] L. Niemeyer. Physical Processes Determining the Interruption Limits of Gas Blast Switchgear. In *International Conference on Developments in Design and Performance of EHV Switching Equipment*, London, UK, 1979. IEE, London, UK.

[NNH+01] H. Nakao, Y. Nakagoshi, M. Hatano, T. Koshizuka, S. Nishiwaki, A. Kobayashi, T. Murao, and S. Yanabu. DC current interruption in HVDC SF6 gas MRTB by means of self-excited oscillation superimposition. *IEEE Transactions on Power Delivery*, 16(4):687–693, 2001. doi: 10.1109/61.956757.

[NR73] L. Niemeyer and K. Ragaller. Development of Turbulence by the Interaction of Gas Flow with Plasmas. *Zeitschrift für Naturforschung A*, 28(8):1281–1289, jan 1973. doi: 10.1515/zna-1973-0807.

[NR17] K. Niayesh and M. Runde. *Power Switching Components*. Power Systems. Springer International Publishing, Cham, 2017. doi: 10.1007/978-3-319-51460-4. ISBN: 978-3-319-51459-8.

[PBC14] E. Panousis, M. Bujotzek, and T. Christen. Arc Cooling Mechanisms in a Model Circuit Breaker. *IEEE Transactions on Power Delivery*, 29(4):1806–1813, aug 2014. doi: 10.1109/TPWRD.2014.2312134.

[PSC+17] E. Panousis, P. C. Stoller, J. Carstensen, V. Teppati, R. Methling, S. Franke, and S. Gorchakov. Active and passive optical diagnostics in a model HV circuit breaker. In *XXXIII ICPIG*, volume 33, page 72, 2017. URL

`http://icpig2017.tecnico.ulisboa.pt/wp-content/uploads/2017/06/ICPIG2017{_}proceedings.pdf`.

[Rag78] K. Ragaller. *Current Interruption in High-Voltage Networks*. Springer US, Boston, MA, 1978. doi: 10.1007/978-1-4757-1685-6. ISBN: 978-1-4757-1687-0.

[RBF16] A. Ritter, L. Bort, and C. Franck. Five years of pulsed current testing for HVDC switchgear. In *2016 IEEE International Conference on High Voltage Engineering and Application (ICHVE)*, pages 1–4. IEEE, sep 2016. doi: 10.1109/ICHVE.2016.7800658.

[RF18] A. Ritter and C. M. Franck. Prediction of Bus-Transfer Switching in Future HVdc Substations. *IEEE Transactions on Power Delivery*, 33(3):1388–1397, jun 2018. doi: 10.1109/TPWRD.2017.2764386.

[Rij75] H. Rijanto. *Ein experimentelles Verfahren zur Bestimmung von Lichtbogenkenngrößen - Stromüberlagerungsverfahren*. Dissertation, Technische Universität Hannover, 1975.

[Rit18] A. Ritter. *Disconnector Switching in HVAC and Future HVDC presented by*. Phd thesis, ETH Zürich, 2018. doi: 10.3929/ethz-b-000272999.

[RQ96] B. T. Rhodes and J. G. Quintiere. Burning rate and flame heat flux for PMMA in a cone calorimeter. *Fire Safety Journal*, 26(3):221–240, apr 1996. doi: 10.1016/S0379-7112(96)00025-2.

[RS01] M. Rahimo and N. Shammas. Freewheeling diode reverse-recovery failure modes in IGBT applications. *IEEE Transactions on Industry Applications*, 37(2):661–670, 2001. doi: 10.1109/28.913734.

[RSF18] A. Ritter, U. Straumann, and C. M. Franck. Improving GIS Disconnectors for Future HVDC Applications. *IEEE Transactions on Power Delivery*, 8977(c):1–1, 2018. doi: 10.1109/TPWRD.2018.2844374.

[Rup79] R. Ruppe. Experimentelle und theoretische untersuchungen am axial beströmten wechselstromlichtbogen vor dem stromnulldurchgang. *Dissertation, TH Illmenau*, 1979.

[Sch73] J. Schwarz. *Berechnung von Schaltvorgängen mit einer zweifach modifizierten Mayr-Gleichung.* Dissertation, Technische Hochschule Darmstadt, 1973.

[SH14] H. Schmid and A. Huber. Measuring a Small Number of Samples, and the 3σ Fallacy: Shedding Light on Confidence and Error Intervals. *IEEE Solid-State Circuits Magazine*, 6(2):52–58, jan 2014. doi: 10.1109/MSSC.2014.2313714.

[SHBF19] T. Schultz, B. Hammerich, L. Bort, and C. Franck. Improving interruption performance of mechanical circuit breakers by controlling pre-current-zero wave shape. *High Voltage*, pages 1–9, apr 2019. doi: 10.1049/hve.2018.5103.

[SHK+98] T. Shioiri, M. Honma, E. Kaneko, M. Miyagawa, and I. Ohshima. Insulator characteristics of vacuum interrupter for a new 72/84 kV C-GIS. In *Proceedings ISDEIV. 18th International Symposium on Discharges and Electrical Insulation in Vacuum (Cat. No.98CH36073)*, volume 2, pages 744–747. IEEE, 1998. doi: 10.1109/DEIV.1998.738869.

[Sim15] B. Simonet. *Design and Testing of Supersonic Nozzles for High Current DC Circuit Breakers.* Master thesis, ETH Zürich, 2015.

[SK00] R. Smeets and V. Kertesz. Evaluation of high-voltage circuit breaker performance with a new validated arc model. *IEE Proceedings - Generation, Transmission and Distribution*, 147(2):121, mar 2000. doi: 10.1049/ip-gtd:20000238.

[Ska11] P. Skarby. HIGHVOLTAGE DC BREAKER APPARATUS, 2011. URL `https://patents.google.com/patent/US8995097B2/en`.

[SLF16] T. Schultz, V. Lenz, and C. M. Franck. Circuit Breakers for Fault Current Interruption in HVDC Grids. In *VDE-Fachtagung Hochspannungstechnik*, number November, 2016. doi: 10.3929/ethz-a-010795297.

[SPC+15] P. C. Stoller, E. Panousis, J. Carstensen, C. B. Doiron, and R. Färber. Speckle measurements of density and temperature profiles in a model gas circuit breaker. *Journal of Physics D: Applied Physics*, 48(1):015501, jan 2015. doi: 10.1088/0022-3727/48/1/015501.

[STCA06] M. Seeger, J. Tepper, T. Christen, and J. Abrahamson. Experimental study on PTFE ablation in high voltage circuit-breakers. *Journal of Physics D: Applied Physics*, 39(23):5016–5024, dec 2006. doi: 10.1088/0022-3727/39/23/018.

[Str15] J. Strumbelj. *Simulation and Upgrade of HVDC Bus-Transfer Setup*. Master thesis, ETH Zürich, 2015.

[SvdS00] P. Schavemaker and L. van der Sluis. An improved Mayr-type arc model based on current-zero measurements. *IEEE Transactions on Power Delivery*, 15(2):580–584, apr 2000. doi: 10.1109/61.852988.

[SYBS15] R. Smeets, A. Yanushkevich, N. Belda, and R. Scharrenberg. Design of test-circuits for HVDC circuit breakers. In *2015 3rd International Conference on Electric Power Equipment Switching Technology (ICEPE-ST)*, pages 229–234. IEEE, oct 2015. doi: 10.1109/ICEPE-ST.2015.7368338.

[TCF17] J. Thomas, G. P. Chaffey, and C. M. Franck. Small-Scale HVDC Circuit Breaker. *IEEE Transactions on Components, Packaging and Manufacturing Technology*, 7(7):1058–1068, jul 2017. doi: 10.1109/TCPMT.2017.2694058.

[Tho04] R. Thomas. *Controlled Switching of High Voltage SF6 Circuit Breakers for Fault Interruption*. PhD thesis, Chalmers University of Technology, 2004.

[Tho14] J. Thomas. *Small scale testing of hvdc circuit breakers*. Master thesis, ETH Zürich, 2014.

[TL75] D. T. Tuma and J. J. Lowke. Prediction of properties of arcs stabilized by forced convection. *Journal of Applied Physics*, 46(8):3361–3367, 1975. doi: 10.1063/1.322240.

[TWZ+16] G. F. Tang, X. G. Wei, W. D. Zhou, S. Zhang, C. Gao, Z. Y. He, and J. C. Zheng. Research and Development of a Full-bridge Cascaded Hybrid HVDC Breaker for VSC-HVDC Applications. *Cigre Session 2016*, pages 0–9, 2016. URL `https://e-cigre.org/publication/A3-117{_}2016`.

[VCP+85] J. Vithayathil, A. Courts, W. Peterson, N. Hingorani, S. Nilsson, and J. Porter. HVDC Circuit Breaker Development and Field Tests. *IEEE Transactions on Power Apparatus and Systems*, PAS-104(10):2692–2705, oct 1985. doi: 10.1109/TPAS.1985.319110.

[Von18] M. Vonesch. *Gas Circuit Breaker Arc Voltage Under Different Flow Conditions*. Master thesis, ETH Zürich, 2018.

[Wal13] M. M. Walter. *Switching Arcs in Passive Resonance HVDC Circuit Breakers*. PhD thesis, ETH Zürich, 2013. doi: 10.3929/ethz-a-010112102.

[WF14] M. M. Walter and C. M. Franck. Optimal Test Current Shape for Accurate Arc Characteristic Determination. *IEEE Transactions on Power Delivery*, 29(4):1798–1805, aug 2014. doi: 10.1109/TPWRD.2013.2297400.

[WLF13] M. M. Walter, C. Leu, and C. M. Franck. Optimizing the Arc Characteristics for Improved Designs of Passive Resonant Hvdc-Circuit Breakers. pages 317–322, 2013. doi: 10.3929/ethz-b-000078010.

[WLL+18] W. Wen, B. Li, B. Li, J. He, Y. Wang, Y. Huang, T. Cheng, and L. Weidong. No-Load Dielectric Recovery of the Ultra-Fast Vacuum Switch in Hybrid DC Circuit Breaker. *IEEE Transactions on Power Delivery*, 8977(c):1–1, 2018. doi: 10.1109/TPWRD.2018.2881764.

[WWR+14] Y. Wu, Y. Wu, M. Rong, F. Yang, C. Niu, M. Li, and Y. Hu. Research on a novel two-stage direct current hybrid circuit breaker. *The Review of scientific instruments*, 85(8):084707, 2014. doi: 10.1063/1.4893481.

[WYC+18] T. Wei, Z. Yu, Z. Chen, X. Zhang, W. Wen, Y. Huang, and R. Zeng. Design and test of the bidirectional solid-state switch for an 160kV/9kA hybrid DC circuit breaker. *Conference Proceedings - IEEE Applied Power Electronics Conference and Exposition - APEC*, 2018-March:141–148, 2018. doi: 10.1109/APEC.2018.8341000.

[YZH06] S. Yanabu, E. Zaima, and T. Hasegawa. Historical Review of High Voltage Switchgear Developments in the 20th Century for Power Transmission and Distribution System in Japan. *IEEE Transactions on Power Delivery*, 21(2):659–664, apr 2006. doi: 10.1109/TPWRD.2005.861228.

[ZYC+18] X. Zhang, Z. Yu, Z. Chen, Y. Huang, B. Zhao, and R. Zeng. Modular Design Methodology of DC Breaker Based on Discrete Metal Oxide Varistors with Series Power Electronic Devices for HVDC Application. *IEEE Transactions on Industrial Electronics*, PP(c):1–1, 2018. doi: 10.1109/TIE.2018.2886787.

A. Appendix

During the course of this thesis, much more data was generated than can be presented in this thesis.
Namely, pressure at three locations (bottle, mixing volume and nozzle throat), contact travel and highspeed video was captured during almost all experiments.
Additionally, the model described in section 3.3 was used to simulate time to current zero for a wide range of parameters L and C, using a rather academic arc as input. Those simulations could be easily repeated with $u(i)$ curves and τ of real interrupters.
In case you are interested to obtain more detailed data, please write me an email: i-have-read-your-thesis (at) lbmail.eu